A Study of Direct Measuring Skin Friction Gages for High Enthalpy Flow Applications

by

Ryan James Meritt

Master's Thesis Submitted to the Faculty of the
Virginia Polytechnic Institute and State University
In partial fulfillment of the requirements for the degree of

Master of Science
In
Aerospace Engineering

Dr. J. A. Schetz, Chairman

Dr. W. J. Devenport

Dr. W. H. Mason

April 30, 2010
Blacksburg, VA

Keywords: skin friction, wall shear, high-enthalpy, complex turbulent flow, aerodynamics

A Study of Direct Measuring Skin Friction Gages for High Enthalpy Flow Applications

Ryan J. Meritt
Dr. J. A. Schetz, Chairman
Aerospace Engineering

Abstract

This study concerns the design, analysis, and initial testing of a novel skin friction gage for applications in three-dimensional, high-speed, high-enthalpy flows. Design conditions required favorable gage performance in the Arc-Heated Facilities at Arnold Engineering Development Center. Flow conditions are expected to be at Mach 3.4, with convective heat properties of $h = 1{,}500\ W/m^2 \cdot K$ ($264\ Btu/hr \cdot ft^2 \cdot °R$) and $T_{aw} = 3{,}900\ K$ ($7{,}000\ °R$). The wall shear stress is expected to be as high as $\tau_w = 2{,}750\ Pa$ ($0.40\ psi$) with a correlating coefficient of skin friction value around $C_f = 0.0035$. Through finite element model and analytical analyses, a generic gage design is predicted to remain fully functional and within reasonable factors of safety for short duration tests. The deflection of the sensing head does not exceed $0.025\ mm$ ($0.0001\ in$). Surfaces exposed to the flow reach a maximum temperatures of $960\ K$ ($1{,}720\ °R$) and the region near the sensitive electronic components experience a negligible rise in temperature after a one second test run.

The gage is a direct-measuring, non-nulling design in a cantilever beam arrangement. The sensing head is flush with the surrounding surface of the wall and is separated by a small gap, approximately $0.127\ mm$ ($0.005\ in$). A dual-axis, semi-conductor strain gage unit measures the strain in the beam resulting from the shear stress experienced by the head due to the flow.

The gage design incorporates a unique bellows system as a shroud to contain the oil filling and protect the strain gages. Oil filling provides dynamic and thermal damping while eliminating uniform pressure loading. An active water-cooling system is routed externally around the housing in order to control the temperature of the gage system and electronic components. Each gage is wired in a full-bridge Wheatstone configuration and is calibrated for temperature compensation to minimize temperature effects.

Design verification was conducted in the Virginia Tech Hypersonic Tunnel. The gage was tested in well-documented Mach 3.0, cold and hot flow environments. The tunnel provided stagnation temperatures and pressures of up to $T_0 = 655\ K$ (1,180 $°R$) and $P_0 = 1{,}020\ kPa$ (148 psi) respectively. The local wall temperatures ranged from $T_w = 292$ to 320 K (525 to 576 $°R$). The skin friction coefficient measurements were between 0.00118 and 0.00134 with an uncertainty of less than 5%. Results were shown to be repeatable and in good concurrence with analytical predictions.

The design concept of the gage proved to be very sound in heated, supersonic flow. When it worked, it did so very effectively. Unfortunately, the implementation of the concept is still not robust enough for routine use. The strain gage units in general were often unstable and proved to be insufficiently reliable. The detailed gage design as built was subject to many potential sources of assembly misalignment and machining tolerances, and was susceptible to pre-loading. Further recommendations are provided for a better implementation of this design concept to make a fully functional gage test ready for Arnold Engineering Development Center.

Acknowledgements

I would like to first express my sincerest gratitude to my Advisor, Dr. Joseph A. Schetz for his guidance, mentorship, and friendship throughout my graduate education. He has enlightened me through his broad knowledge of viscous boundary layers, high-speed aerodynamics, and fluid dynamics. He has shown me different ways to approach a research problem, was always there to meet and talk about my ideas, and asked good questions to help me think through tough problems.

I would like to thank the Department of Aerospace Engineering (AOE) at Virginia Tech, especially those members of my committee for their input and advice, Dr. W. J. Devenport and Dr. W. H. Mason. In particular, I greatly appreciate the expertise, hard work, and patience from Mr. James Lambert, Mr. Scott Patrick, and Mr. Mark Montgomery of the AOE machine and electrical shops.

The funding for this research was provided by Arnold Engineering Development Center ($AEDC$). Thank you to Dr. Joseph Sheeley, Dr. Wayne Hawkins, and the others at $AEDC$ for this great opportunity and challenge.

I would also like to acknowledge Alex Sang and Luna Innovations for their insightful ideas with regard to the bellows and LeePlug design, oil filling procedures, and for the donation of resources.

I am deeply grateful to Col Russell Walden, Lt Col Keith Gay, and Capt Chris Andersen who have taught me a great deal about leadership, perseverance, and dedication throughout my years of cadet training in Air Force R.O.T.C. They made it possible for me to carry on an additional year at Virginia Tech and complete this degree. These gentlemen have been my role models and it has been an honor to have worked with them.

I am blessed to have such wonderful friends: Shadie Tanious, Tyler Aarons, Lindsay King, Craig Metzger, Natalie Madeja, and Joshuah Hess. They have been there every step of the way through my college career, and I am where I am today because of them. The memories I shared with them are everlasting, and they have all positively influenced my life like no others could have.

Lastly, I would especially like to thank my parents: Robin Lott and Kirk Meritt for their unconditional love and support. They gave me life, instilled strong moral values, taught me personal responsibility, encouraged my interests, and showed me the importance of education. Generously, they always gave me their personal time, hard-fought efforts, and true self so that I may grow up to face this challenging world with a positive attitude and a strong will.

Table of Contents

List of Figures

List of Tables

Nomenclature

A	reference area
a	acceleration
a, b	calibration constants
BL	boundary layer
C	lip size
C_D	drag coefficient
C_f	skin friction coefficient
D	diameter
E_i	excitation voltage
E_o	output voltage
F_D	drag force
F_c	boundary-layer transformation factor
G	gap size
g	gravitational acceleration
GF	gage factor (strain gage)
h	heat transfer coefficient
k	spring constant
L, ℓ	length
M	Mach number
M_o	moment
m	mass
Pr	Prandtl number
P	pressure
q	dynamic pressure
$\dot{q}_w$	heat flux
R	resistance
r	radius
St	Stanton number
T	temperature
T^*	reference temperature
t	time
U	velocity
u^*	friction velocity
u^+	velocity divided by friction velocity
v	transverse velocity
x	axial distance downstream
X	Cartesian mean flow direction
y	lateral distance
Y	Cartesian spanwise perpendicular
y^+	transverse coordinate for Law of the Wall
Z	misalignment

Greek

α	material thermal diffusivity
Δ	change
β	temperature functions
δ	boundary layer thickness
ε	strain
μ	dynamic viscosity
ρ	density
τ	shear
θ	gage offset angle
ν	kinematic viscosity
ω	frequency
ζ	damping ratio

Subscripts

aw	adiabatic wall
$comp$	compressible
DSC	strain sensor region
e	edge of the boundary layer
i	initial
inc	incompressible
w	wall surface
x, y, z	Cartesian components
0	total or stagnation quantity
1	in front of shock wave
2	behind shock wave

Superscripts

$+$	laminar sublayer nondimensionalization
$*$	reference value

1. Introduction

Why do we want to develop a skin friction gage for high-enthalpy flows? In order to determine and maximize the efficiency of any fluid machinery device, the knowledge and quantification of the resistance to the fluid motion in the system is essential [1]. Aerospace engineers have long sought to take advantage of this fluid interaction in high-speed, high-temperature environments. There is still much to learn about skin friction from this area of study, and has been a matter of extensive research over the past decades. Such is the purpose and aim of the research presented in this thesis.

1.1. Importance of Measuring Skin Friction

Before any knowledge of fluid measurement systems can be considered, it is important to first fully understand the fundamentals of drag. Any object interacting with a fluid medium will experience a retarding force, deemed the drag, parallel and opposite to its relative direction of motion [2]. The force due to drag, F_D, is defined as,

$$F_D = \frac{1}{2}\,\rho\,U^2\,C_D\,A \qquad \textbf{Equation 1}$$

where ρ is the density of the fluid, U is the velocity, C_D is the drag coefficient, and A is the reference area. The drag force can be broken down into two primary categories: pressure drag and skin friction or surface friction drag [3]. Though the magnitudes of these drag components will change, they are always present on aircraft and are experienced at all speeds regimes from subsonic to hypersonic.

Pressure drag is the force arising from the resolved components of pressure acting normal to the surface. It can be subdivided into several distinct contributions: induced or vortex drag, wave drag, and form or boundary layer pressure drag [4]. Induced drag is drag due to lift.

Because of the pressure differential on the top and bottom surfaces of the wing, air will shed off the wing tips to produce vortices. This circular motion creates a greater angle of attack near the wing tips region thus causing an increase in drag. Wave drag occurs in supersonic flight due to the formation of shock waves. A shock wave creates a sudden change in pressure at the front of the aircraft or wing which produces a large pressure drag across the body. Lastly, form drag is caused by the flow separation induced by the shape, or form, of the platform. Components that are the not perfectly streamlined produce pockets of high and low pressure regions resulting in a pressure drag [5].

The second drag force component is skin friction drag. Skin friction is generated by shear stresses produced through the interaction of fluid particles and the surface of the body. This occurs tangentially on the surface and within the thin viscous region adjacent to the body also known as the boundary layer [6]. The magnitude of the skin friction drag correlates to the properties of both the gaseous flow and solid surface. In regard to the gas, the magnitude depends upon the relationship between the motion of the flow and viscous forces, i.e. Reynolds number. In regard to the solid, drag is related to the roughness or finish of the surface and the size of the wetted area.

Skin friction is often expressed as a coefficient of shear stress as seen in Equation 2,

$$C_f = \frac{\tau_w}{1/2\ \rho_e\ U_e^2} \qquad \textbf{Equation 2}$$

where τ_w is the shear stress at the wall, and the subscript e designates the value on the edge of the boundary layer. Under the assumption of the no-slip condition and continuum flow, the intensity of the shear stress at the surface is given by Equation 3,

$$\tau_w = \mu \left. \frac{\partial U}{\partial n} \right|_w \qquad \textbf{Equation 3}$$

where μ is the dynamic viscosity of the fluid, and $\partial U/\partial n$ is the change in velocity normal to the surface of the body. Equation 3 is valid throughout a laminar boundary layer, and due to the laminar sublayer, a turbulent boundary layer as well [7]. The critical component in Equations 2 and 3 is the wall shear stress, and that will be the focus and desired measurable value throughout this study.

1.2. Motivation

The knowledge of skin friction is vital to understanding the performance of a system. Drag must be overcome by the thrust in order for the body to achieve forward motion. How effectively this is accomplished defines the flight performance and economics of the aircraft. Reducing the drag will require less thrust, ultimately saving weight and minimizing fuel consumption. Cost savings has been, and always will be, a driving force in the aerospace industry.

Skin friction drag can account for more than half the total drag acting upon an aerodynamic system [8]. Since it is caused by the viscous drag in the boundary layer, it will increase with complex turbulent flow. In addition, skin friction follows the drag equation (Equation 1) such that it increases by roughly the square of the fluid velocity. Thus, it becomes evident that skin friction considerations grow increasingly important in regard to high-speed, high-enthalpy flows.

Over the last five to six decades, a great deal of effort has been placed in the study of high-enthalpy flow regimes as experienced by re-entry vehicles, hypersonic aircraft, and ram/scramjet engines. Many projects have attempted to minimize the source of drag in such

applications, but only a few have been met with success. This is due, primarily to, the inability to accurately predict and experimentally determine skin friction in such hostile environments. These applications are subject to extreme pressures, temperatures, velocities, and vibrations which produce very complex turbulent patterns with high and varying heat-fluxes. In these flow regimes, analytical methods begin to break down due to dissociation, ionization, and variable Prandtl number, etc. Modern skin friction measurement methods also suffer due to a variety of induced errors and destructive conditions.

Experimental data is used in the verification of new physical models, validation of result credibility, quantitative evaluation of computational errors, and certification of most computational fluid dynamics (CFD) frameworks. Thus, the next step to understanding skin friction in high-enthalpy flow environments lies in the ability to apply both new and proven methods to experimentally measure its quantitative value.

1.3. Scope of Investigation

There exists an increasing need to expand the measurement capabilities of skin friction gages. The goal of this research is to do just that. In order to meet the research objectives outlined below, novel and proven methods will be applied to develop a new class of skin friction measurement devices.

1.3.1. Objectives

The principal objective of this research is to develop a skin friction gage capable of performing favorably in high-enthalpy flow conditions such as those experienced at the Arnold Engineering Development Center ($AEDC$) Arc-Heated Facilities. This is a formidable challenge to overcome. The gage must first and foremost be robust in design in order to survive harsh testing environments and to increase its effective life.

Second, it must be sensitive enough to measure the small wall shear quantity with reasonable accuracy. Even once this is accomplished, there are still more design challenges to face. The highly sensitive gage must be insensitive to vibration, temperature, and pressure influences as well as electro-magnetic interference. To counteract these undesirable effects, the gage must incorporate some form of shielding, damping, and thermal managements systems.

The gage design concept must also be versatile so that its application may be adaptive and flexible for a wide range of flow conditions. The design must be lightweight to reduce inertial effects and as small as possible to allow easy incorporation and service in a variety of facilities.

There is no required sustainable time duration, so the gage only needs to be exposed to the adverse flow for as long as it takes to obtain data. This can be accomplished accurately in less than one second. Lastly, the system and all its components need to meet the environmental and vibration requirements of the facility.

1.3.2. Generic Skin Friction Gage Concept

Researchers at Virginia Polytechnic Institute and State University (Virginia Tech) have devoted a great deal of study to skin friction gages in a variety of hostile environments. Each project presents innovative ideas and important lessons from its conclusions. Such knowledge serves as a vital starting point to this study.

Chadwick (1992) [9] and DeTurris (1992) [10] used a non-nulling cantilevered configuration in heated supersonic applications within scramjet combustors. Novean (1996) [11], Remington (1999) [12], and Magill (1999) [13] all experimented with non-fluids to minimize vibration effects in complex transonic and supersonic flows. Pulliam (2000) [14] and Orr (2004) [15] examined fiber optic sensors for complex, high-temperature flows. Smith (2001)

[16] developed a cantilever beam gage for the Hyper-X scramjet engine model which was successfully tested at the NASA Langley Arc-Heated Scramjet Test Facility. Rolling (2007) [17] produced a new class of skin friction gages capable of shock impingement compensation. Most recently, Sang (2007) [18] designed a gage that incorporates a bellows system to enhance robustness at extreme temperatures and adverse vibration conditions. A detailed review of the non-nulling, skin friction gages developed at Virginia Tech can be found in the Schetz review article [19].

The most successful of the gage designs used in these projects, is the non-nulling, cantilever beam arrangement. This is also the most practical concept for this study as will be justified later in Chapter 2.1: *Methods of Measuring Skin Friction*. A generic configuration of the cantilever beam concept is shown in Figure 1.

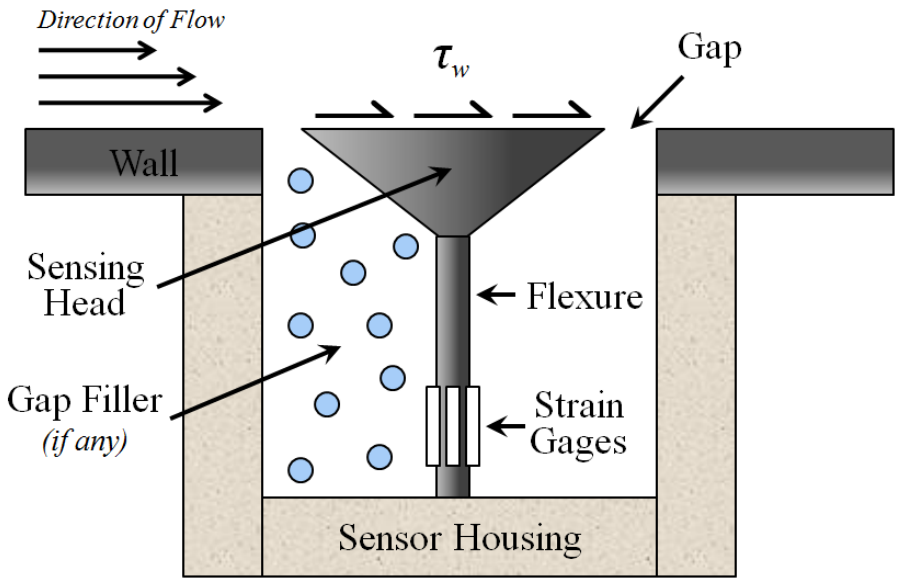

Figure 1: Generic Direct Measurement, Non-nulling, Cantilever Beam Concept

The sensing head is flush with the wall and measures the tangential forces imparted by the flow. It is typically circular in cross-section, and surrounded by a small gap to allow for slight deflections. The head is connected to the flexure beam, with sensitive strain gages placed

in the high strain region near its base. The desired measurement comes from the displacement of the sensing head or strain imposed on the system. Through calibration, the direction and magnitude of the shear stress is determined. Initial design studies were conducted on the generic cantilever beam concept to determine if it was possible for a skin friction gage to perform favorably under conditions at Arnold Engineering Development Center.

1.3.3. Arnold Engineering Development Center

The High-Enthalpy Ablation Test Unit ($HEAT$) Arc-Heated Facilities at Arnold Engineering Development Center ($AEDC$) provides the aerospace industry with aero-thermal ground test simulations of hypersonic flight [20]. Arc heaters are widely used in the development of high-speed vehicles, including military/civil space transportation and space access vehicles, reentry vehicles, high-speed transports, scramjet combustors, and hypervelocity ordnance and munitions systems. The arc-heated facilities at $AEDC$ are unique as they are the only state-of-the-art, high-pressure arc facilities in the world.

One such arc tunnel at $AEDC$, and where the gage will be tested at, is the $HEAT$-H2 test unit which utilizes an N-4 Huels-type arc heater [21]. The heater employs a high-voltage, direct current electric arc discharge to heat the air. The electrical arc discharge is then confined to a water-cooled plenum section to achieve high-pressure test flows. The combination of high-enthalpy test gas and high plenum pressure makes it possible to attain simulated hypersonic flight conditions in excess of Mach 20 at pressure altitudes from 20 to 50 km (70 to 160 kft) and total temperatures of up to 7,200 K (13,000 $°R$). Such operating conditions are possible for long exposure periods of 30 minutes and more [22]. The general $HEAT$-H2 arc tunnel specifications are presented in Table 1.

Table 1: *HEAT*-H2 Arc Tunnel Specifications [21]

Parameter	Value	Units
Max. Run Time	Up to 30	min
Nozzle Mach No.	3.4 to 8.3	
Nozzle Exit Diam.	13.0 to 107 (5.0 to 42.0)	cm in
Stagnation Pressure	Up to 10	atm
Stagnation Enthalpy	2,750 - 15,000 (1,200 – 6,500)	kJ/kg Btu/lb_m
Mass Flow Rate	1.0 to 4.5 (2 - 10)	kg/s lb_m/s
Facility Power	Up to 42	MW

1.3.4. AEDC Case study

Initial design studies confirmed that a skin friction gage can be designed to perform favorably under conditions at $AEDC$ for short duration tests. These preliminary analyses identified thermal distribution, sensing head displacement, and modal frequencies for a generic skin friction gage following earlier Virginia Tech designs. Verification was accomplished through the use of *ANSYS* [23], a general-purpose finite element model analysis package. Solution methodology and the analytical verification of *ANSYS* is described later in Chapter 5.3: *Finite Element Model Analysis*.

The heat transfer analysis identifies the thermal state of a generic stainless steel gage after a one second test run cycle. Flow conditions are assumed at Mach 3.4, with convective heat properties at $h = 1{,}500\ W/m^2 \cdot K$ ($264\ Btu/hr \cdot ft^2 \cdot °R$) and $T_{aw} = 3{,}900\ K$ ($7{,}000\ °R$). The exposed surfaces of the gage are estimated to reach a maximum temperature of 960 K ($1{,}720\ °R$) which is well under the pliable region of the materials. Additionally, thermal penetration does not reach more than about 12.7 mm (0.5 in) down from the surface, thus the region near the sensitive electronic components experience a negligible rise in temperature.

The structural analysis identifies stresses imposed on the components as well as the sensing head displacement. The Eckert method [24] was employed to estimate wall shear loading. A detailed description of prediction techniques are discussed later in Chapter 5.2: *Skin Friction Estimations*. The wall shear stress is expected to be as high as $\tau_w = 2{,}750\ Pa$ (0.40 psi) with a correlating coefficient of skin friction value around $C_f = 0.0035$. The deflection experienced by the sensing head is 0.025 mm (0.001 in), which is less than maximum deflection rating of the flexure by a factor of safety of 12. Additionally, stress and strain predictions were well within the limitations of the materials.

Lastly, the dynamic response of the system to include the first six modal frequencies was also determined. The frequency range is between 0 to 10,000 Hz. Though no vibration requirements were set by $AEDC$, vibration verification maybe necessary in the future to determine the damping capabilities of the gage.

1.3.5. Approach

Gage verification will consist of a rigorous process designed to systematically evaluate individual aspects of the gage and their functionality. To begin, each skin friction gage must first undergo static calibrations of its strain sensor measurement system. This will consist of hanging known masses from the end of the cantilever beam to simulate wall shear stress. These shear stress values are then correlated to the voltage output from the strain sensor unit. All primary deflection axes will be calibrated. The gage will then be thermally cycled to quantify the sensitivity of the strain sensors to various temperature conditions. A new temperature compensating calibration curve will be devised from these results.

The gage will then be extensively tested for remnant air bubbles in the oil filling in Virginia Tech's vacuum chamber. With the gage inside, the pressure is pumped down to near

vacuum conditions, and the strain sensor voltage output will be monitored. All possible gage orientations will be tested. If the gage remains unaffected under the vacuum, it will be deemed ready for wind tunnel testing.

Cold flow testing will be performed at Mach 3.0 in the Virginia Tech Hypersonic Tunnel. The experimental results will be compared to analytical predictions to see if they are in good agreement and if the gage is working properly. In the same facility, the gage will then undergo heated flow testing up to air stagnation temperatures of 655 K (1,180 $°R$). If the trials are successful, the gage validation testing is complete. Once the gage has proven to be fully functional and up to standard, the final step is to test it at the $AEDC$ Arc-Heated Facilities.

1.4. Outline

The following chapters detail the work performed in this study:

Chapter 2 gives an overview of skin friction gages with insight into different measurement methods and techniques. The chapter also explores entire gage hierarchy and final design choice of this study. Research shows that information on gage sub-systems, with an introduction in to their underlying principles, makes them essential for gages in high-enthalpy flow applications.

Chapter 3 presents the design methodology for direct, non-nulling, skin friction gages. This approach addresses design considerations and geometric constraints, as well as potential errors prone to such systems. The chapter also provides an overview of the study's unique components in order to account for the strain gage units and bellows. In addition, this chapter explains the proper procedures and practices for gage calibration and oil filling.

Chapter 4 describes the general facilities and instrumentation used throughout this study. It also provides the specifications, layout, and flow properties for the Virginia Tech Hypersonic

and $AEDC$ Arc-Heated Facilities. Lastly, the chapter presents information on the measurement devices and electrical equipments used to obtain and analyze the experimental data in detail.

Chapter 5 identifies theoretical and computational approaches to predict the performance of the skin friction gages. Shear stress in the Virginia Tech Hypersonic Tunnel is initially modeled by analytical and numerical methods. These estimations are based on known flow properties, measured boundary layer information, and computational fluid dynamics. The performance predictions set a foundation on which to compare and justify the experimental results.

Chapter 6 presents a detailed description of the skin friction gages used in this research. This description includes the material selection process, design considerations, as well as insight into the functionality and purpose of each component. The chapter then explains gage construction, assembly, and static calibration in detail. Lastly, the chapter follows the development of the first skin friction gage and evolutionary changes that made the second skin friction gage successful.

Chapter 7 presents the experimental results from the Virginia Tech Hypersonic Tunnel. The chapter thoroughly analyzes the performance of each skin friction gage and presents in chronological order. The first gage proves the general design concepts and implementation of the strain gage unit. The second gage successfully integrates and implements the bellows, oil filling, and thermal management system.

Chapter 8 analyzes the uncertainty for the skin friction gages. It explores three categories of measurement errors: calibration, data acquisition, and data reduction. The chapter introduces a variety of error sources and presents a summary of uncertainty conclusions.

Finally, Chapter 9 presents the conclusions and recommendations of this study. The contributions of this study will be summarized. It also discusses how well the goals and objectives of this research were met. Lastly, it provides suggestions and recommendations for future work with direct skin friction gages in high-enthalpy flow.

2. Survey of Skin Friction Measurement Devices

Chapter 2 gives an overview of skin friction gages with insight into different measurement methods and techniques. The chapter also explores entire gage hierarchy and final design choice of this study. Research shows that information on gage sub-systems, with an introduction in to their underlying principles, makes them essential for gages in high-enthalpy flow applications.lpy flow applications.

2.1. Methods of Measuring Skin Friction

The first skin friction investigation dates back over a century ago with a British engineer named William Froude [25]. In 1872, Froude conducted a series of hydrodynamic experiments by towing streamlined catamaran planks at various speeds through water by use of the measurement apparatus shown in Figure 2. This led him to develop his law of skin friction similarity at a time when the qualitative effects of Reynolds number and boundary layer theory were not well understood.

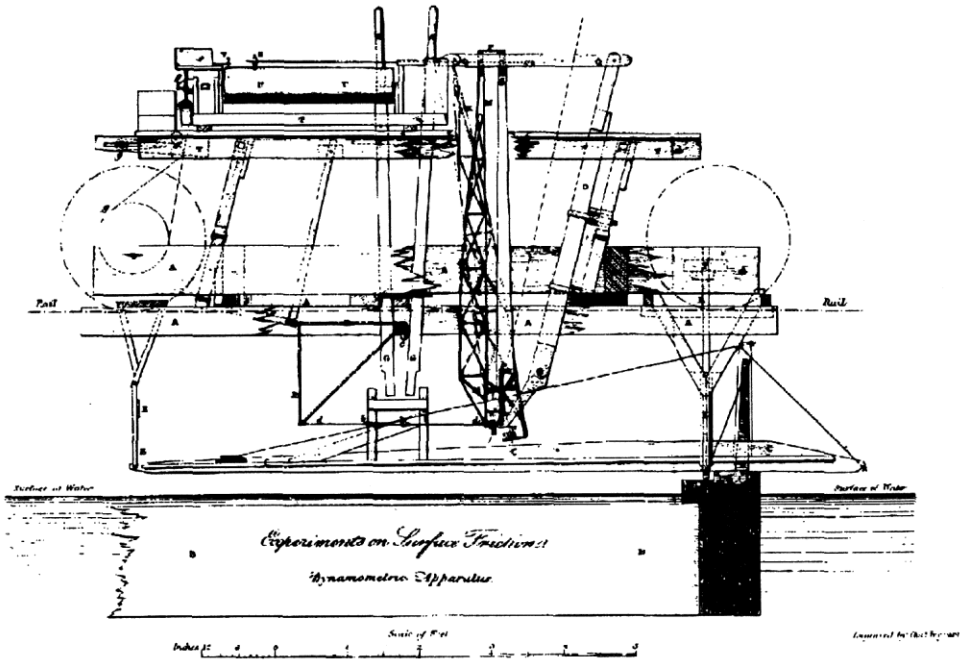

Figure 2: Measurement Apparatus used by William Froude [25]

Over the last 100 years, various techniques have been developed and tested to experimentally measure skin friction. For further reference, Winter [26] published a detailed history on the chronological development of measurement techniques. Additionally, in a collaborated effort under Schetz, an overview of movable element skin friction gages has been compiled in tabulation format [27].

Methods can be categorized into two fundamental areas of measurement technique: indirect and direct methods. They are distinguished by their approach and the physical quantity in which they measure. Indirect methods require properties of the boundary layer to be known *a priori* and to be defined well. The flow quantities are then related back to shear stress through analytical correlations. Direct methods require no prerequisite knowledge about the flow and therefore do not impose any assumed laws. Instead, direct methods rely on a floating element which directly measures the tangential frictional forces of the flow. The measurement technique hierarchy is depicted in Figure 3. The highlighted path is the technique utilized in this research.

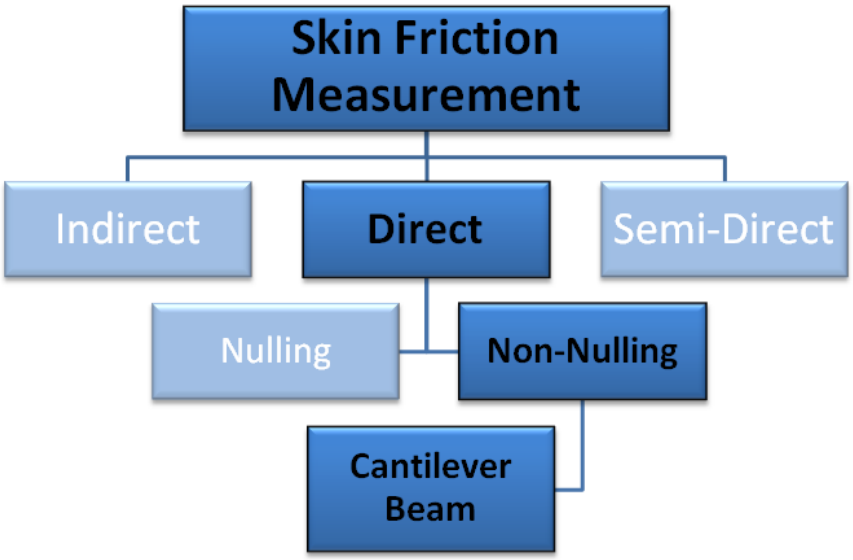

Figure 3: Classification Hierarchy of Skin Friction Measurement Techniques

In the early studies of skin friction, indirect methods were considered the more feasible option. However, the advent of high-speed aircraft led to a greater interest and surge in the research for more precise measurement devices, especially in the study of compressible, turbulent flows. Complimented by technological advances, direct methods have become the more practical and widely preferred means of measuring skin friction. A chart of the unique advantages and disadvantages of direct and indirect methods was developed by Pulliam [28], and is shown in Table 2.

Table 2: Advantages and Disadvantages of Skin Friction Measurement [28]

Measurement Technique		Advantages	Disadvantages
Direct Measurements (Force)			
➢ **Non- Nulling**		• flow and fluid independent • able to determine direction • non-intrusive	• small force • high cost • low frequency response • complex and cumbersome in size
➢ **Nulling**		• flow and fluid independent • able to determine direction • non-intrusive • high frequency response	• small force • high cost • subject to misalignment
Semi-Direct Measurements			
➢ **Oil Film Interferometry**		• flow and fluid independent • able to determine direction • non-intrusive	• temperature sensitive • shear stress, shear gradient, time limited • requires optical access
➢ **Liquid Crystals**		• flow and fluid independent • able to determine direction • non-intrusive	• temperature and pressure sensitive • requires optical access • low sensitivity • limited time window • shear stress limited
Indirect Measurements			
➢ **Analogy**	○ Heat Transfer (Reynolds Analogy)	• dual purpose sensor • low cost • high frequency response	• low precision measurement • not able to determine direction • limited temperature range with high temperature sensitivity • requires knowledge of free-stream
	○ Mass Transfer	• low cost	• calibration not available • low precision measurement • not able to determine direction • limited temperature range with high temperature sensitivity • requires knowledge of free-stream
➢ **Flow About Obstacles** (Viscous Sub-layer)	○ Sub-Layer Fence	• simple • low cost	• difficult calibration • susceptible to misalignment • assumes Law of the wall • requires knowledge of boundary layer conditions
	○ Stanton Tube	• simple • low cost	• susceptible to misalignment • assumes Law of the wall • requires knowledge of boundary layer conditions
➢ **Profile Measurement** (Law of the Wall)	○ Preston Tube	• simple • low cost	• flow calibration required • susceptible to misalignment • assumes Law of the wall • boundary layer thickness limited • requires knowledge of boundary layer conditions
	○ Hot-Wire	• simple • provides high frequency data	• assumes law of the wall • fragile and temperature limited • requires knowledge of fluid viscosity
	○ Laser Doppler Anemometry	• non-intrusive • provides high frequency data	• requires optical access • requires seed particles • requires knowledge of fluid viscosity

2.1.1. Indirect Methods

As noted before, indirect methods are based on some prior knowledge or assumption of the flow conditions. Many skin friction measurement techniques are classified under this approach method. A summary of the most popular of these techniques, including their associated calibrations and underlying principles, are presented in Figure 4. For further reference, a detailed discussion on indirect methods can be found in Nitsche [29].

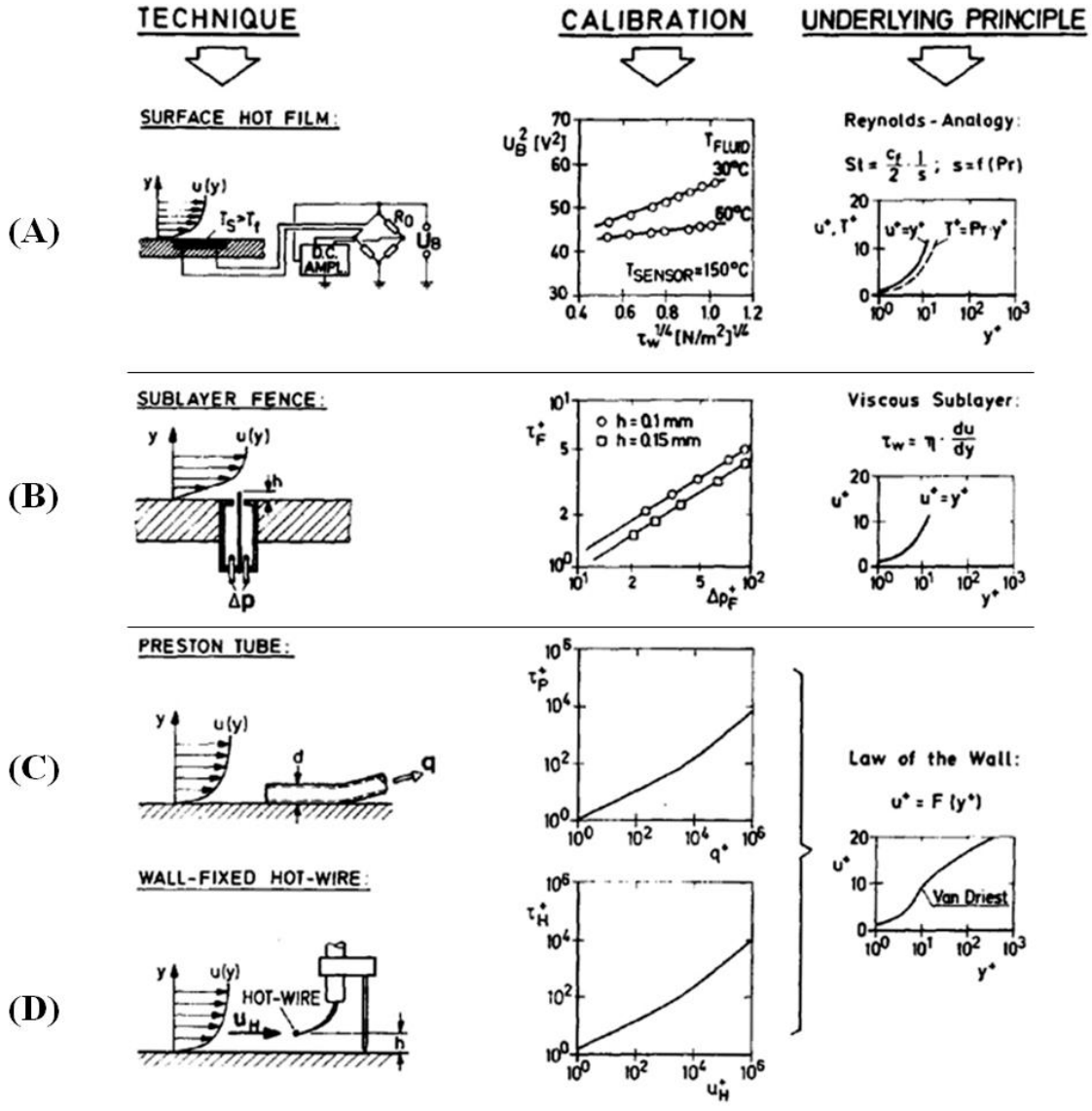

Figure 4: Examples of Indirect Wall Shear Measurement Techniques [29]

Indirect methods are best suited for steady, two-dimensional, incompressible flows where the flow properties are consistent and predictable. Thus, flows where the free-stream properties are difficult to define cannot be accurately considered. This eliminates many conditions to include: unsteadiness, compressibility, transition, separation, three-dimensionality, and changing thermo-physical properties.

Analogy

Analogy techniques define the relationship of skin friction to heat and mass transfer. These physical property changes are observed within the velocity laminar sublayer near the surface of the wall. Surface hot-film or hot-wire techniques, as illustrated in Figure 4A, are all based on Reynolds Analogy which directly relates skin friction to heat transfer through the relationship,

$$St \cdot \mathrm{Pr}^{2/3} = {}^{C_f}/_{2} \qquad \textbf{Equation 4}$$

where St is the Stanton number, and Pr is the Prandtl number. A wire is heated to a temperature greater than that of the flow and as air moves past it, the wire cools. A constant-temperature anemometer measures the convective heat loss across the wire and correlated this to wall shear through a calibration.

The other method, similar to Reynolds Analogy, relates skin friction to the mass transfer of material from the wall surface. Both techniques are highly sensitive to temperature fluctuation and thus are not suited for complex flows. Even in simple flows, they are unable to determine the direction of shear stress or provide a precise quantitative measurement.

Flow about Obstacles

The viscous sublayer technique utilizes a small obstacle on the surface which the flow must go around, and thus creating a pressure difference in the boundary layer. The induced pressure gradient and velocity distribution are used to derive shear stress through the laminar sublayer laws of similarity (Equation 5). Numerous obstacles have been implemented as skin friction meters, but only the sub-layer fence and Stanton tube are widely used.

$$u^+ = y^+, \quad u^+ = \frac{u}{u^*}, \quad y^+ = \frac{y\,u^*}{v} \qquad \textbf{Equation 5}$$

The sub-layer fence was first introduced by Konstantinov in 1955 [26]. As shown in Figure 4B, a small vertical strip protrudes through the surface into the boundary layer. Even in a flow with a strong pressure gradient, its small size allows it to remain within the laminar sublayer and make compressible flow measurements due to its minimal impact on density variations. To its disdvantage, its small size also makes it hard to geometrically define and therefore calibrate.

The Stanton Tube is similar in concept to a Pitot-tube and is simple to construct. It is composed of a static pressure port that is flush and tangent to the surface. The port is obscured by a razor-sharp lip to produce a small opening facing into direction of the flow [30]. The setup projects upward a small distance from the surface on an order of 0.12 mm (0.005 in). A schematic of the Stanton Tube is shown in Figure 5.

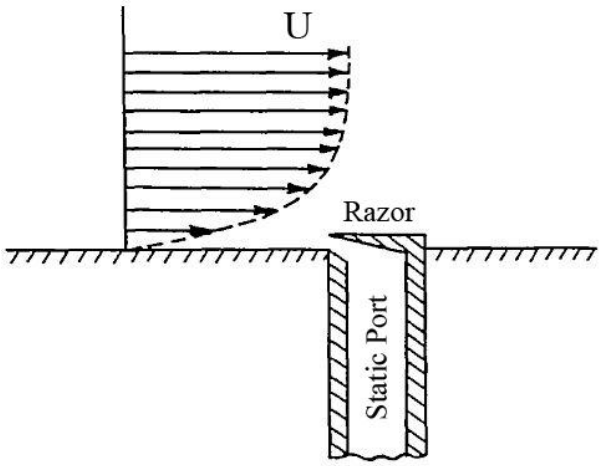

Figure 5: Stanton Tube [30]

The small opening of the Stanton Tube lies within the laminar sublayer of the turbulent boundary layer. This design trait reduces the effects of pressure gradients and compressibility on the results. Unfortunately, all the same problems associated with the sublayer fence still apply here and is complicated by additional error sources stemming from the size and orientation of the razor and pressure orifice.

Profile Measurement

The last class of indirect measurement techniques focuses on the velocity profile in logarithmic region of the turbulent boundary layer. Clauser's (1956) work [31] comprehensively demonstrates that all turbulent profiles are in agreement with the universal law and the correlation indicated in Figure 6. This is known as the Clauser chart or *law of the wall* plot and applies for steady, two-dimensional, constant-density flows.

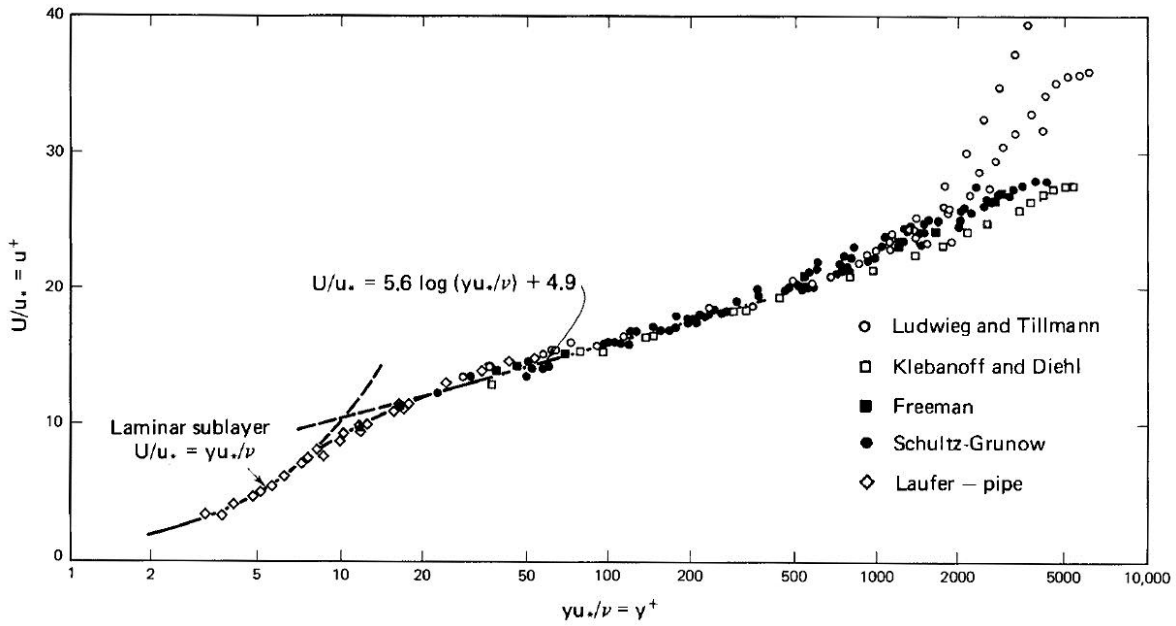

Figure 6: Universal wall law plot for turbulent boundary layers [31]

Shear stress is related to the velocity profile in the logarithmic region defined by Equation 6, such that u/U is a function of $y \cdot U/v$ where the friction parameter $U \cdot u^* = \left(C_f/2\right)^{1/2}$ is accounted for. The three popular methods that implement this technique are the Preston tube, wall-fixed hot-wire, and laser Doppler anemometry.

$$\frac{u}{u^*} = A \cdot \log\left(\frac{y\,u^*}{v}\right) + B \quad or \quad \frac{u}{U}\frac{U}{u^*} = A \cdot \log\left(\frac{y\,U}{v}\right) + A \cdot \log\left(\frac{u^*}{U}\right) + B \qquad \textbf{Equation 6}$$

The Preston tube, as illustrated in Figure 4C, consists of a circular Pitot tube lying flush to the surface. It is similar in principle to the Stanton tube as it relates the Pitot-static pressure measurement, tube dimensions, and the properties of the flow to one another in order to determine the shear stress on the wall. However, unlike the Stanton tube, it is much larger in size and not only senses the laminar sublayer, but the entire *law of the wall* which includes the overlap and logarithmic regions as well. Its larger size creates measurement uncertainty as it

requires many correction factors for situations including heat flux, misalignment, pressure gradients, and wall roughness.

The wall-fixed, hot-wire method, as illustrated in Figure 4D, measures the velocity profile in the logarithmic region by means of a constant-temperature anemometer and correlates it to shear stress through a calibration. It has a few advantages over the Preston tube as the wire is much smaller in size and is less intrusive to the flow. Additionally, it takes a measurement at a known distance from the wall, instead of a displaced distance, which simplifies the correlation to shear stress. Unfortunately, as with most hot-wire techniques, the method is very sensitive to temperature variance, which is even more difficult to control in the logarithmic region. For obvious reasons, all these intrusive techniques are problematic in high-enthalpy flows.

Variations to these two techniques have been used to eliminate the need for the *law of the wall* contributions in the calibrations. Nitsche [29] used several Preston tubes of different sizes and orientations with much success. The same idea can be performed with the hot wire method through the use of multiple wires.

The laser Doppler anemometry (LDA) is another common profile measurement technique. In a typical LDA setup, two beams of collimated and coherent laser light cross within the flow stream to produce an interference pattern. Tracer particles are seeded into the flow upstream and pass through the fringes. The particles reflect the light, generating a light pulse which can be measured, and allows for the flow velocity to be statically determined. The tracer particles are the biggest concern as they may not survive in high temperature flows or follow the flow accurately near shocks or the wall. This technique also requires optical access, which may be unavailable in many test situations.

2.1.2. Semi-Direct Methods

Semi-direct methods pertain to a class of wall shear stress measurement techniques which measure shear stress directly, but unlike direct methods, are severely limited by the flowfield conditions. These methods have in common the ability to globally measurement skin friction with rather good spatial resolution, while remaining non-intrusive to the flow [14]. Unfortunately, they are often highly sensitive to flow properties and require a good deal of optical access to the test article in which to make the necessary measurements. These techniques are useful and advantageous in simple test cases, but are not suitable for three-dimensional, complex, high-enthalpy flows. The two semi-direct methods most commonly used are the oil film interferometry, sometimes referred to as Laser Interferometer Skin Friction ($LISF$) Meter, and shear-sensitive liquid crystals.

Originally developed by Tanner and Blows [32], oil film interferometry is based on a relatively simple concept. A thin film of silicone oil is applied to a polished test article in the flow. As it is subjected to shear stresses, the thickness of the oil film will decrease. A laser interferometer is used to measure the time rate of thinning of the oil film which can then be related to skin friction. To accomplish this, one component of the laser beam reflects at the air-oil interface (R_1) while the other component is reflected at the surface of the test article (R_2). Fringe patterns are devised from the path length difference, and related to the thickness of the oil film. A diagram of the oil film interferometry process is depicted in Figure 7.

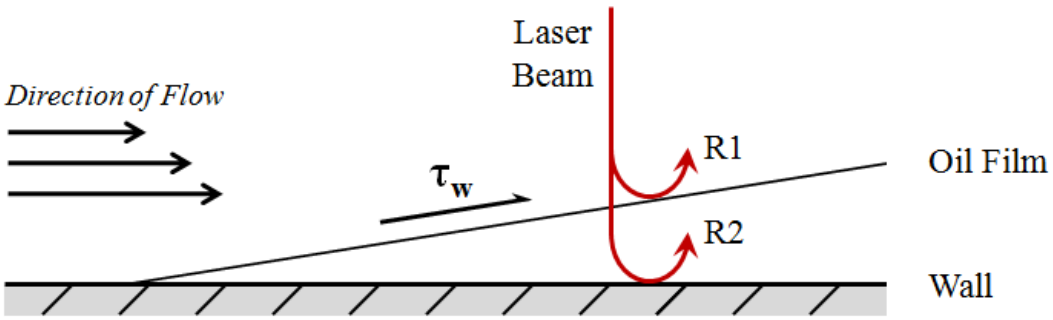

Figure 7: Oil Fill Interferometry Method

The method is very sensitive to temperature change due to its dependency on the viscosity of the oil. It is also very susceptible to both temperature and pressure gradients since the underlying oil flow equations assume these to be zero with constant wall shear stress. The direction of the flow should be known beforehand as the oil film must be approximately perpendicular to the flow streamlines [33].

The second method of using shear-sensitive liquid crystals was first explored by Klein and Margozzi [34]. Liquid crystals are weakly ordered, viscous, and exist in a non-uniform, fluid-like state. The nature of their helical structure causes them to be extremely optically active. As a measurement tool, liquid crystals are applied in layers on top of the test article and arranged relative to the layer above and below it. Under applied shear stress, the local pitch of the liquid crystals is altered. During a test case, they are illuminated by an unpolarized white light, and the incident light is reflected back in a highly directional manner. This reflection is captured at different viewing angles and the net result is a three-dimensional color spectrum. Through careful calibration, these color patterns can be interpreted into a shear stress pattern across the entire test article [35].

The shear-sensitive liquid crystals are non-intrusive and require no knowledge of the directional orientation of the flow streamlines. However, similar to the previous method, it is very sensitive to temperature and pressure changes of the flow. This makes the necessary

calibration very difficult to conduct accurately. The liquid crystals are also limited as they will crystallize within a matter of a day which causes them to lose their light scattering ability, thus the need to be replaced often [36].

2.1.3. Direct Methods

By now it is apparent that the experimental determination of shear stress through semi-direct and indirect methods is subject to many uncertainties. Direct force measurement methods take an entirely different approach and are generally more reliable and accurate than the other techniques with a broader range of applicability. Direct methods are based on a very simple principle in which a floating element, flush with the wall, measures the tangential forces imparted by the flow. The element, typically circular in cross-section, is surrounded by a small gap to allow for movement and is supported by a flexure. The displacement of the element or strain imposed on the system is measured, and through calibration, the direction and magnitude of the shear stress is determined.

Since direct methods are non-intrusive to the flow and do not rely on any physical assumptions regarding the nature of the boundary layer, they are inherently very suitable for surface friction measurements [37]. Historically, a number of different systems have utilized this direct approach with varying degrees of success. Direct measurement techniques generally can be sorted into two categories: nulling and non-nulling.

Nulling Gages

Nulling designs use a restoring force mechanism to return the floating element back to a neutral position. Since the restoring force is equal to and opposite to the shear stress, the floating element experiences a zero net displacement. The first successful gage of a nulling design is credited to Dhawan [30] in 1953 when he used it to measure skin friction in the subsonic regime

for laminar and turbulent boundary layers. A schematic of the device Dhawan developed is illustrated in Figure 8.

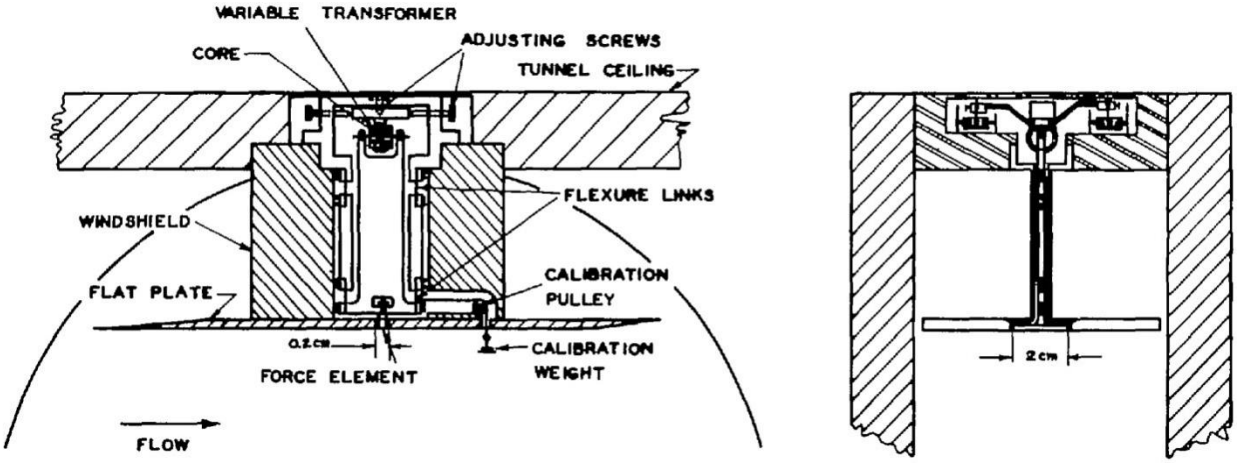

Figure 8: Nulling Design Skin Friction Gage built by Dhawan [30]

To its advantage, all the components exposed to the flow do not move and the flow remains undisturbed, which inherently reduces the uncertainty from the measurements. However, such designs are mechanically complex and cumbersome in size. This disadvantage makes them prone to error and slow to respond to flow phenomena, i.e. low frequency response. The nulling technique has had limited success in high-speed applications but is generally used in two-dimensional, unheated flows.

Non-Nulling Gages

Non-nulling designs are much more basic in concept as they do not have a restoring force mechanism. See Figure 1 for a schematic of one such concept. The floating element is allowed to deflect very slightly under shear loads while the strain in the supporting flexure is measured and related directly to skin friction. Due to its simplicity, the non-nulling configuration has many advantages when compared to a nulling design. Its design, fabrication, and maintenance are less complicated, and due to its smaller size, is much more manageable for engineering

applications. All of this makes it less susceptible to error and gives it a higher frequency response.

On the other hand, non-nulling gages are more subject to misalignment problems, which will be discussed later in Chapter 3.2.1: *Misalignment Effects*. It is important for the floating element to not protrude into the flow or come in contact the wall. The effects of misalignment can be virtually eliminated by stiffening the flexure to make it more resistive to shear force loading and limit its displacement to very small values.

Numerous types of non-nulling gage designs have been explored over the years. One early concept, as shown in Figure 9, is the parallel-linkage supporting design. The floating element is supported by two beams to eliminate tilting and prevented misalignment problems. Movement due to applied shear is monitored by a Linear Variable Differential Transformers (*LVDT*) at the base. Unfortunately, the use of two flexures requires a larger sensing surface and thus reduces its sensitivity.

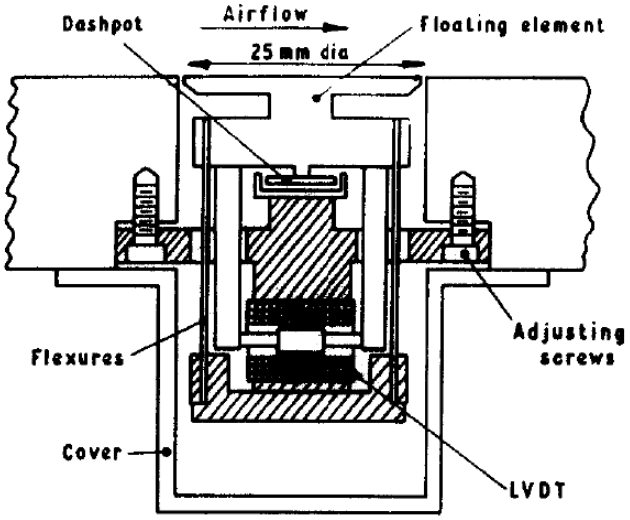

Figure 9: Parallel-linkage Supporting Arrangement built by Winter [26]

Another type of design is where the floating element is supported by tethers around its periphery. Strain gages are mounted on each tether to measure displacement. This allows for a very compact design but exposes the strain gages to the flow, making the design sensitive to motion normal to the wall and temperature variation. A silicon micro-machined example [38] of this design type is shown in Figure 10.

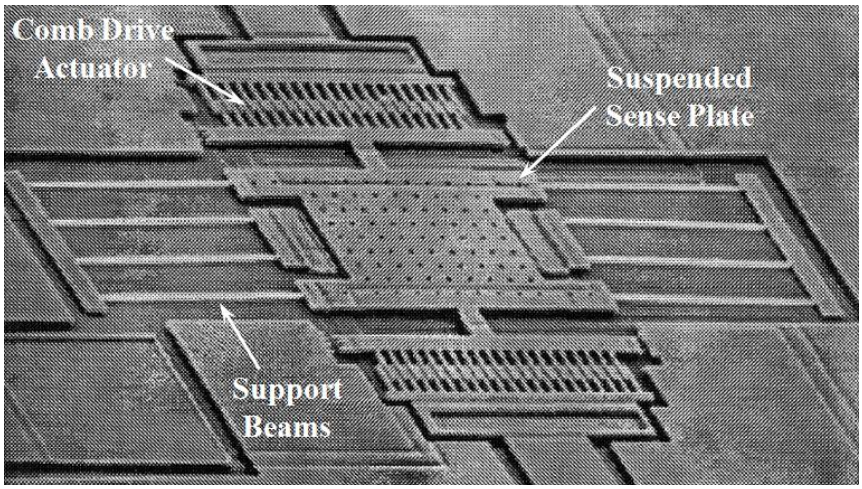

Figure 10: Silicon Micro-machined Version of a Table-Top Design [38]

In recent years, sensory technology has evolved and some non-nulling gages now incorporate fiber optics. Such gages use lasers to measure deflection directly rather than electronics to measure strain. Successful examples of fiber optic skin friction sensors have been developed by Pulliam (2000) [28] and Orr (2004) [39].

The most popular non-nulling design used today, and the one used in this study, is the cantilever beam concept. An example of such a configuration was shown previously in Figure 1. A non-nulling, cantilever beam design has the capability to measure multiple components of the wall shear stress in three-dimensional flows, thus eliminating directional ambiguity. Additionally, errors from temperature mismatches can be minimized if the sensing head is constructed of similar geometry and materials as the surrounding wall. The cantilever beam

design benefits from being sensitive to small wall shear values while remaining insensitive to much larger normal pressure values.

In principle, direct measurement methods offer the simplest and most straight-forward methodology to successful obtaining shear stress quantifications than any other technique. The direct measurement, non-nulling, cantilever beam arrangement is clearly an ideal choice for high-enthalpy flow applications. An additional benefit includes the flexibility in design and capability of incorporating a variety of essential sub-systems.

2.2. Skin Friction Gage Sub-Systems

In this study, two primary sub-systems are incorporated into the gage design to allow it to adequately function in high-enthalpy flow environments. The thermal management system actively cools the gage by pumping water throughout the system to control thermal effects. The oil filling and bellows system provide viscous damping to reduce gage sensitivity to vibration and pressure influences.

2.2.1. Thermal Management

The heat transfer through the skin friction gage greatly influences the ability to determine the accuracy of the measurement and survivability of the gage under the harsh conditions to which it is exposed. In a facility like $AEDC$ where the stagnation temperatures reach upward of 7,200 K (13,000 $°R$), thermal management systems are important for a variety of reasons. Detailed descriptions of common thermal effects influencing the gage are explored later in Chapters 3.2.2: *Thermal Effects* and 3.3.2: *Strain Gage Thermal Effects*. Two past researches at Virginia Tech who have developed thermal management systems for skin friction gages are Chadwick (1992) [9] and Smith (2001) [16].

Chadwick experimented with several means to manage the thermal effects in very hot flows. He first incorporated an internal active water-cooling system within the floating element to eliminate non-uniform temperature effects between it and the surrounding wall. Due to the limitation of the small interior cavity, assembly was very difficult and the effectiveness of the cooling proved to be only marginal. He later included self-temperature compensating strain-gages and an external cooling system around the housing. These improvements had greater significance on the accuracy of the strain gages and reduced the uncertainty in the shear stress measurements to approximately 15%. A schematic to Chadwick's $GASL$ skin friction gage design is seen in Figure 11.

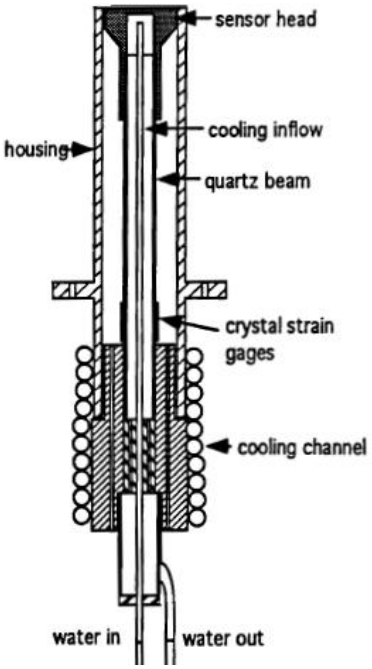

Figure 11: Chadwick - *GASL* Test Design [9]

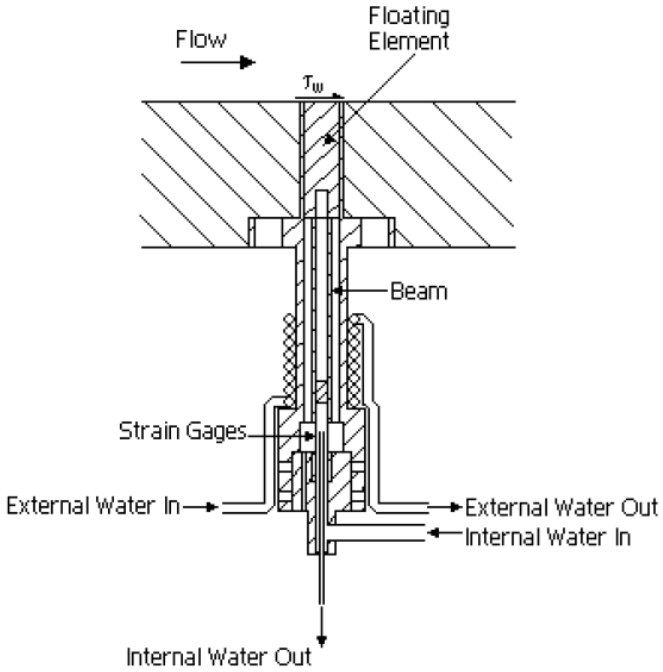

Figure 12: Smith - Gage Design Two [16]

Smith built upon Chadwick's active water-cooling systems by adding silicon oil to fill the gage's interior volumes. The schematic of his second skin friction gage design is shown in Figure 12. Similarly, Smith's design routed cooling tubes both internally and externally around housing in order to control the temperature of the strain gage sensors. Unfortunately, this setup

revealed some serious problems. The internal cooling tubes were transmitting small forces to the strain sensors, thus pre-loading the gage. Water leaks were also common due to difficulties in sealing the junctions between the rubber and copper tubing. Lastly, since the gage was mounted upside down in the test section, oil would consistently leak out. In the end, the water-cooling system and oil-fill were completely eliminated in favor of a different gage design concept.

2.2.2. Oil Fill and Bellows

Viscous damping is widely used for system modeling due to its linearity and is the damping method of choice of modern day skin friction gages. Viscous damping is caused by the dissipation of energy that occurs in the liquid lubrication surrounding the vibrating system. Viscous forces are generated by the friction between the vibrating object as it moves through the fluid particles and is directly proportional to their relative velocity.

At Virginia Tech, several different viscous damping techniques have been employed with success. Filling the internal volume with oil has been the most common means and has four beneficial purposes. First, the oil fills in the small gap surrounding the floating element and provides a continuous surface to the external flow, thus eliminating any disruption the gap causes to the boundary layer flow. Second, this encapsulates the sensitive strain gages in an oil of low thermo-conductivity to protect them from thermal effects. Third, the oil fill minimizes the effects of pressure gradients across the sensing head. Fourth, the viscous nature of the oil provides strong damping from environmental vibrations. The main disadvantage commonly found in the oil fill techniques was that oil would slowly leak out of the small gap surrounding the floating element. This left a residue on the surface and inconsistent volumes of oil within the gage, thus making calibration and testing difficult. In some applications, this was unacceptable

and even serious liability to the facility. Figure 13 illustrates a standard oil filled gage that would be susceptible to leaking.

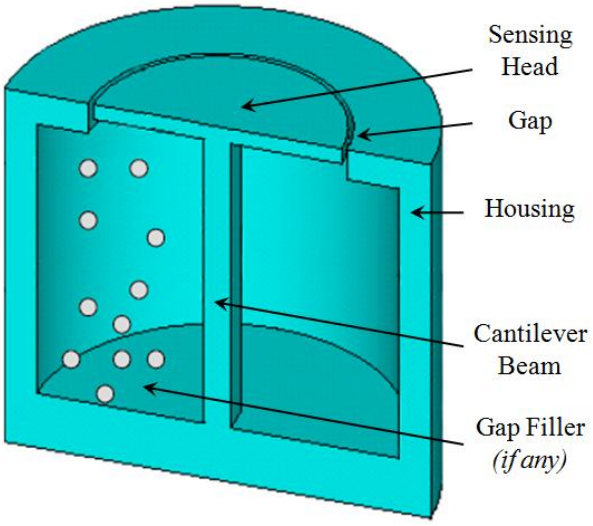

Figure 13: Schematic of a Common Oil Fill Technique [17]

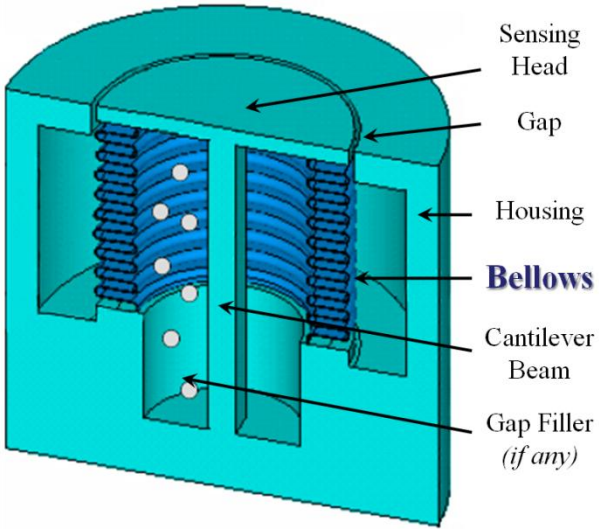

Figure 14: Schematic of Bellows Concept [17]

Work has been done to eliminate these problems while still maintaining all the positive attributes previously discussed. Novean (1996) [11] successfully developed a gage in which he replaced the oil with a rubber filling. The gage suffered from sensitivity issues and measurement resolution was lost due to increased resistance forces. Gage calibration proved to be an even greater obstacle. Sang (2001) [1] used an oil fill but overlaid a thin rubber sheet on the surface of the gage to prevent oil from leaking out. The gage itself was very complex and he had problems adhering the rubber to the metal structure. Though both these designs were met with some success, but they were restricted by the thermal limitations of the rubbers they employed.

In a later efforts, Rolling (2007) [17] and Sang (2007) [18] introduced the use of bellows. Seen above in Figure 14, the bellows form a cavity that contains the oil filling and prevents air bubbles from developing. The gage was made of copper and incorporated and off-the-shelf strain gage unit. Unlike Sang's prior research, the gap surrounding the sensing head was not restricted by any forms of rubber. The bellows is buried deep within the structure and out of the

direct flow stream. The configuration shields hot gas streams and particulate matter from impinging the sensitive interior of the gage. Preliminary tests in the Virginia Tech Supersonic Tunnel were successful. However, the bellows system broke down over time, and the oil leaked out of the gage. It is speculated that the epoxy used in the bellows assembly disintegrated after repetitious testing or failed to adhere to the different materials. The skin friction gage incorporating the bellows concept designed and tested by Sang is seen in Figure 15.

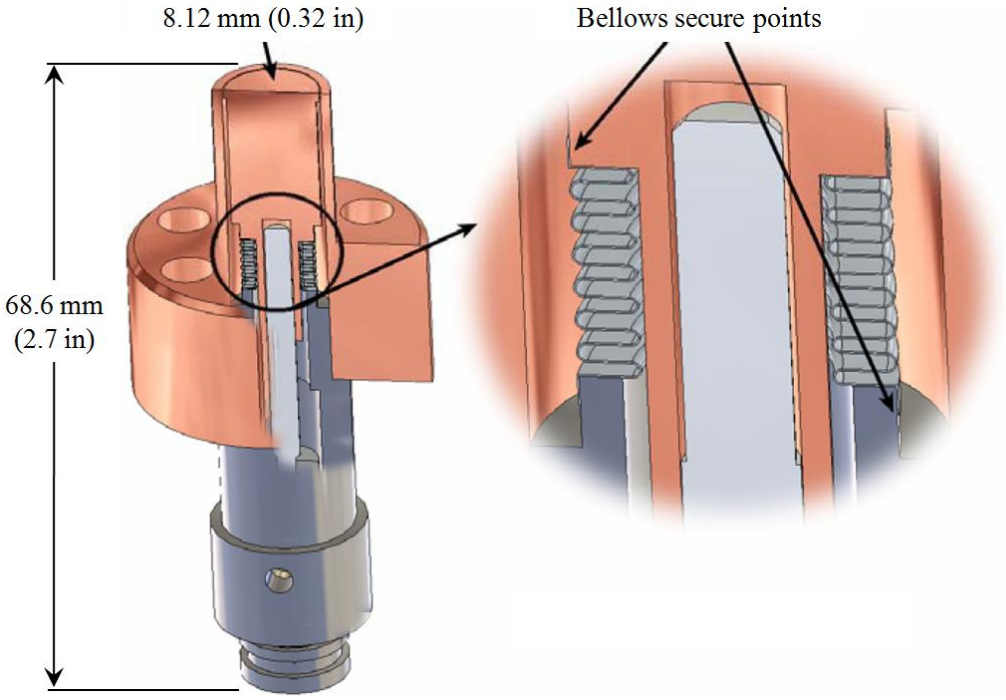

Figure 15: Sang - Sensor Concept [18]

2.3. Skin Friction Gage Design Overview

Through this research, two separate gages were designed and fabricated. They are considered prototype designs for high enthalpy flow applications, and thus are designated appropriately as Prototype One (*PT*-1) and Prototype Two (*PT*-2). Both are classified as direct-measuring, non-nulling, skin friction gages in a cantilever beam arrangement. The *PT*-1 and *PT*-2 designs are shown in Figure 16.

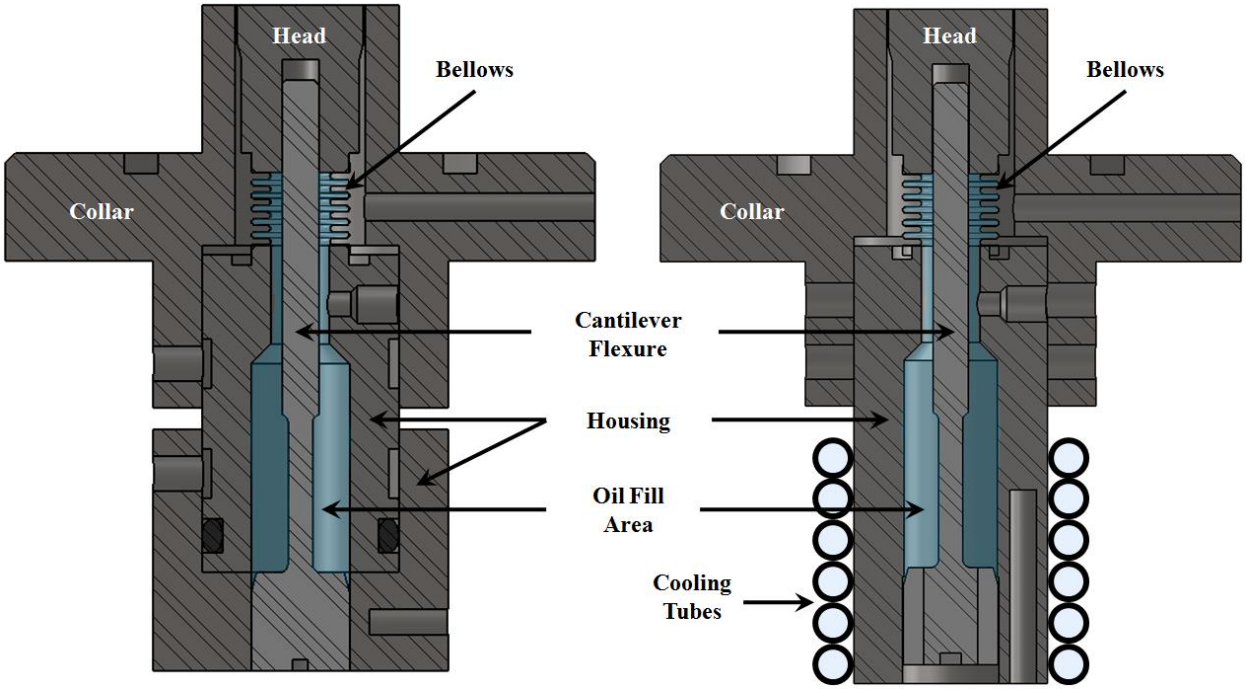

Figure 16: Skin Friction Gages from this Research to Scale: *PT*-1 (left), and *PT*-2 (right)

PT-1 and *PT*-2 are design solutions to measure the nominal wall shear stress of the Virginia Tech Hypersonic Tunnel and *AEDC HEAT*-H2 test unit. Both gages share the same general attributes presented in Figure 1. Each gage is made up of four primary components: the sensing head, cantilever flexure, housing, and collar. Both gages also incorporates a bellows unit, and *PT*-2 utilizes a thermal management system. The number of components is kept to a minimum for simplicity and robustness of the design. These gages are similar in concept, but vary slightly in material and geometry. This is due to the evolution of the design with further understanding of the problem. *PT*-2 has been finely tuned to provide the best solution to meet the goals of this research. The components and variation in both gage designs are discussed at length later in Chapter 6: *Skin Friction Gage Designs*.

3. Design Overview and Constraints

Chapter 3 presents the design methodology for direct, non-nulling, skin friction gages. This approach addresses design considerations and geometric constraints, as well as potential errors prone to such systems. The chapter also provides an overview of the study's unique components in order to account for the strain gage units and bellows. In addition, this chapter explains the proper procedures and practices for gage calibration and oil filling.

3.1. General Design Attributes

The fundamental measurement of a direct, non-nulling, skin friction gages is the elastic strain (ε) along the supporting flexure axis at each strain sensor location. This perpendicular strain is in line with the elongation or shortening of the cantilever beam and shows changes along the beam length. The strain gage unit is intended to respond to the desired input of wall shear (τ_w). The wall shear is the dominating and intended source of induced strain on the system. However, due to the general design attributes of the gage, strain gage unit may also respond to various interfering inputs. The most common of these inputs include pressure (P_w), bending moment (M_o), temperature (T_w) and heat flux ($\dot{q}_w$), and acceleration (a) [17]. The five (nominal set of load conditions) potential sources of strain applied to a cantilever beam are seen in Figure 17. Due to the geometric constrains of a cantilever beam, the inertial loads and wall shear are assumed axial. For a high-enthalpy, short duration test run, the acceleration and heat flux are assumed constant.

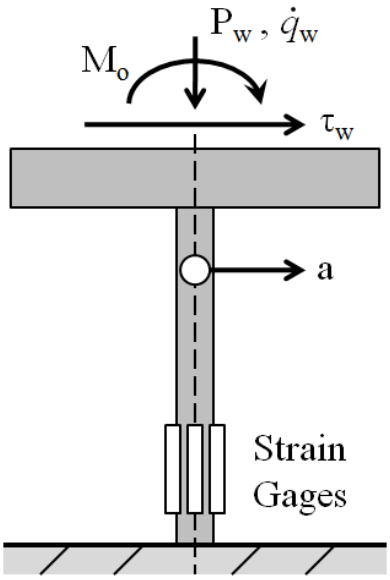

Figure 17: Load Configuration for Simple Cantilever Beam

For an axially varying pressure, $P(x)$, an equivalent moment (M_o) and uniform point load (P_w) can be substituted. In the case when a 2-D shock impinges on the head of the gage, the static pressure on the front half is lower than that of the back, thus creating a moment. Since no impinging shocks are present in this study, the equivalent moment is ignored. Gages with moment compensation have been developed at Virginia Tech [17]. The remaining pressure point load acts perpendicular to the sensing surface and generally has minimal influence on a cantilever beam arrangement [40]. Uniform changes in the static pressure apply a constant but relatively small strain along the length of the flexure.

The inertial loads are assumed axial as they also acts primarily in the mean stream-wise flow direction. As a result, an equivalent acceleration (a) shear can be determined. Acceleration is caused by the motion of the object being measured and is proportional to the applied force. Due to the small mass of the gage, the strain produced by inertial loading is usually much smaller than that from wall shear, and thus acceleration can be ignored.

The heat flux ($\dot{q}_w$) component acts perpendicular to the sensing surface. Over the short duration during a wind tunnel run, heat flux is assumed constant. Any temperature distribution throughout the cantilever beam will be gradual and the strain experienced along the flexure will be uniformly distributed. This justifies the assumption that strain varies directly with temperature.

3.2. Errors in Direct Skin Friction Measurements

Direct, skin friction gages are susceptible to measurement errors related to head misalignment, temperature variation, and oil filing. In some cases, the influence due errors may be of the same order of magnitude as the small shear stress values one is trying to measure. These are important considerations that must incorporated into the gage design itself.

3.2.1. Misalignment Effects

An important area of uncertainty is that surrounding the geometry of the floating element and gap. Many forces from the flow may act upon this region to include the shear force, lip force, and normal force. The floating head must only be sensitive to the shear force. The lip force is applied around the side of the head, while the normal force is applied from the top of the head. These undesired sources of error stem from two potential sources. First, the presence of a gap in the wall, and potential protrusion or recession of the floating head can disrupt the boundary layer flow. This produces a pressure gradient in the flowfield and a resultant off-center normal force. Second, misalignment effects will change the exposed surface area of the floating head and thus directly creating a lip force. A schematic of these phenomena are shown in Figure 18.

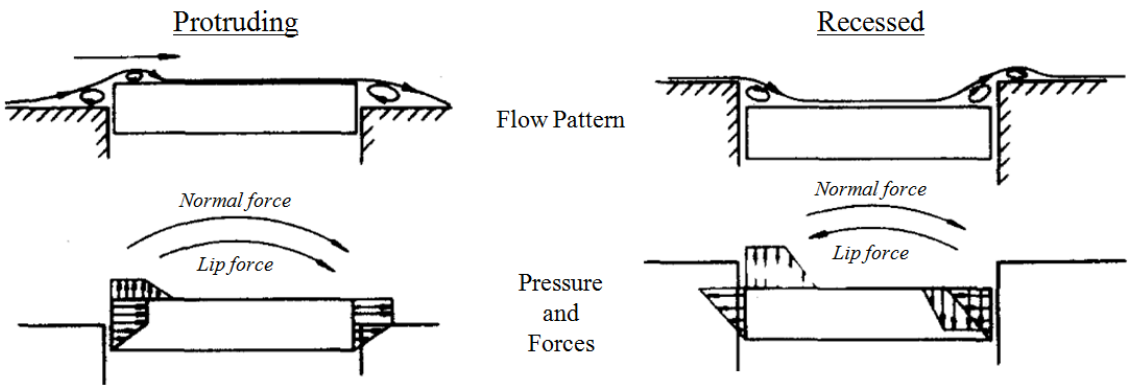

Figure 18: Effects of Misalignment in Direct Skin Friction Gages [41]

A number of extensive studies have been devoted to these prominent issues [41 – 50]. Some of the more notable work was done by Allen [41]. He identified important floating head geometric parameters and their contribution to measurement uncertainties. These parameters are illustrated in Figure 19, where G is the gap size, Z is the misalignment, and C is the lip size.

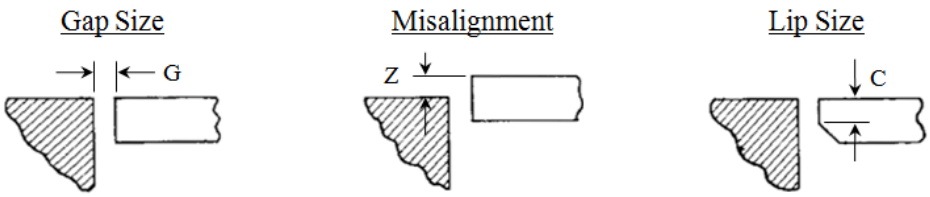

Figure 19: Floating Head Geometric Variables [41]

Allen discovered that while a perfectly aligned floating head would have minimal error, optimizing different geometric parameters could effectively reduce the errors caused by any head misalignment. A sample result from one of his case studies is seen in Figure 20. This figure shows the effects of misalignment on the skin friction gage for different gap sizes. The diameter of the floating head is given by the variable D.

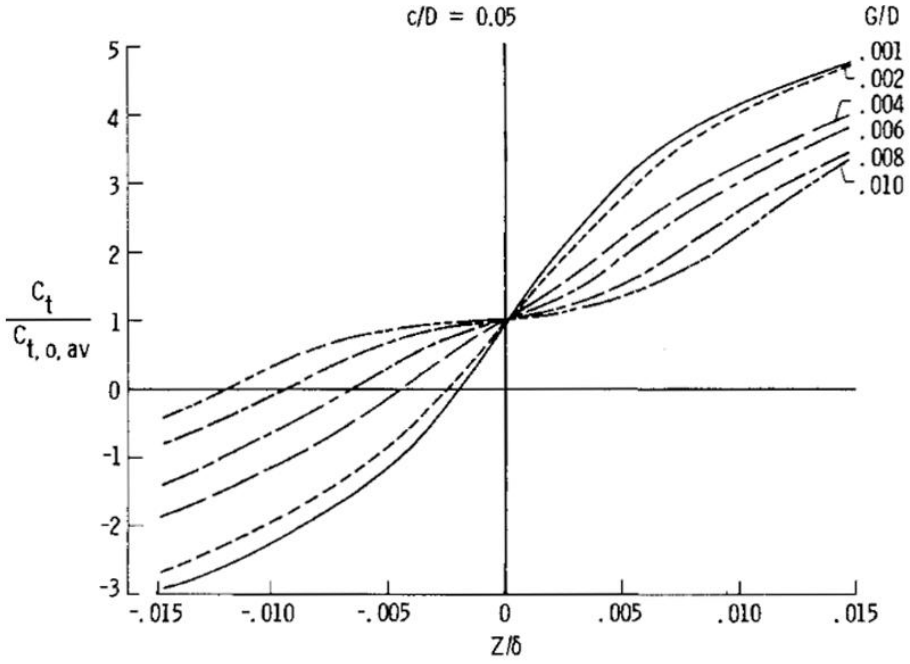

Figure 20: Effects of Head Misalignment and Gap Size on Total Force [41]

Allen concluded that misalignment errors could be reduced by increasing gap-to-diameter (G/D) ratio, and lip-to-diameter (C/D) ratio. He also found that the larger the gap size, the less sensitive the gage was to misalignment.

It must be noted that Allen's work was done in unheated, supersonic flow ($M = 2.2$) on a relatively large floating head ($D = 127\ mm$), nulling gage. Though this provides a useful source of information on how to minimize errors, it is difficult to say how it would relate to a smaller design in high-enthalpy flows. Thus, Allen's work is more primarily used as a guide, and not necessarily considered a strict design rule.

In a non-nulling design, an additional misalignment concern comes from the deflection of the floating head. Due to the nature of the cantilever beam arrangement, under the action of a load, the head not only deflects but also undergoes a small angular tilting. This tilting causes the head to protrude slightly into the flow on one side, and recess on the other side. To prevent this source of error, a beam of sufficient stiffness can be used to make the displacement and tilting

negligible. A head deflection relationship is later derived in Section 3.4: *Head Deflection*, to quantify this amount in order analyze the gage design under expected loads.

3.2.2. Thermal Effects

Uncertainty due to temperature variation effects can be introduced in a number of ways. First, the nature of semi-conductor strain gages makes them very sensitive to temperature changes themselves as will be explained later in Section 3.3.2: *Strain Gage Thermal Effects*. Second, thermal distortions will affect the structural integrity of the entire skin friction gage system.

The gage is composed of several different components, each of which has its own material properties. These distinctions define the operational limits of the gage. For instance, the stainless steel surface of the wall will melt at approximately 1,720 K (3,100 $°R$) [51], the strain gages breakdown at 500 K (900 $°R$) [52], and the nickel alloy bellows will become brittle at 450 K (810 $°R$) [53].

Another effect of temperature variation occurs where the surface flow conditions heat the floating head and the surrounding surface of the wall at different rates. A rapidly changing wall temperature affects the local heat flux dramatically, and by Reynolds Analogy is accompanied by a significant change in local wall shear. This has been experimentally confirmed by Westkaempfer (1963) [54] and Voisinet (1978) [55], but with no agreement to the magnitude of its effect. To minimize any such temperature differences, safest course is to design the gage so that the floating head and surrounding surface are of the same thickness and material.

3.2.3. Oil Fill Effects

In addition to the benefits, there are several difficulties related to filling the interior volume of a skin friction gage with oil. First, it is important to ensure all air bubbles are

removed from the gage during the oil fill process. If any do remain, they will expand during a reduced-pressure test run and exert an extraneous force on the internal components of the gage as exaggerated by the cartoon in Figure 21. This is due to the fact that the bubbles are isolated at the ambient air pressure while the gage experiences a much lower pressure during testing which is often the case in high-speed flows. The undesirable force will preload the cantilever beam and thus contaminate the wall shear results.

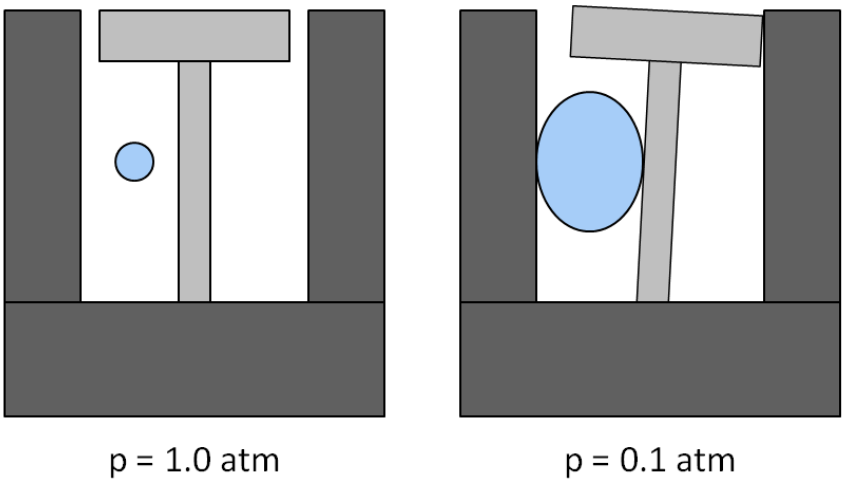

Figure 21: Error Caused by Air Bubble

The second concern with oil filling is the potential for oil leaks. Many skin friction gages that use the oil fill technique are not completely sealed. In these cases, the gages rely on a specific orientation and the high viscosity of the oil to prevent them from leaking. However, during testing a small amount of oil will still typically flow out which requires the oil level of the gage to be constantly monitored and refilled. Additionally, oil smears downstream of the test facility are usually met with dissatisfaction. Oil leakage is preventable by completely sealing the fill cavity of the gage as is done in this research by the use of a bellows system.

3.3. Strain Gage Theory and Practice

Several different strain gage applications have been explored for non-nulling, cantilever beam, skin friction gage concepts. Due to the high levels of expected wall shear and restrictive deflection range, a strain gage with high unit resistance and sensitivity is desired. MacArthur (1963) [56] took the first step by using piezoelectric crystals and although it proved to be a very sensitive method, it only provided transient data. Winter and Gaudet (1970) [57] used resistance foil strain gages when they became more manageable in size, which allowed sensitive measurements in a static environment. Schetz and Nerney (1977) [58] made a significant step by using semi-conductor strain gages which improved the signal output 100 fold. Since then, the Schetz research group has produced a series of skin friction sensors based on semi-conductor strain gages with great success.

3.3.1. Strain Gage Fundamentals

A strain gage is a measurement sensor whose change in electrical resistance is a function of applied strain, where strain is the ratio of the amount of deformation of a specimen to the original length of the specimen (Equation 7). When external forces are applied to the strain gage, it deforms slightly along the surface to which the strain sensors are attached. As a result, the resistance of the sensor material changes and yields a change in its electrical output. Simply stated, a strain gage converts mechanical motion into an electronic signal.

$$\varepsilon = \frac{\Delta L}{L} = \frac{\Delta R / R_o}{GF} \qquad \textbf{Equation 7}$$

In the above equation, L is the length of the conducting wire, R is the nominal strain gage resistance, and GF is the gage factor. Gage factor is the sensitivity rating of a strain gage. The principle equation illustrates how the resistance of the wire increases with increasing strain and

vice versa. Strain gage configurations are arranged in a Wheatstone bridge circuit as seen in Figure 22.

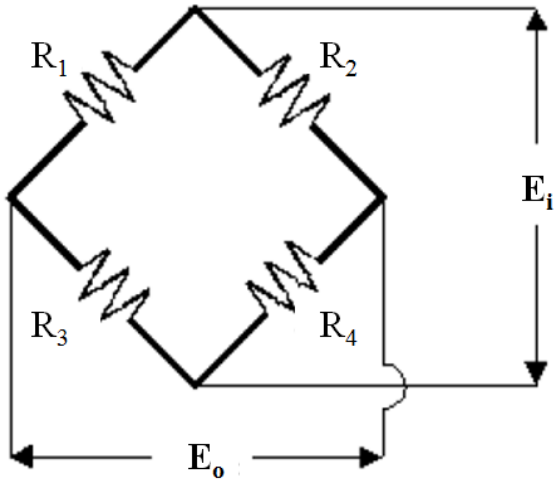

Figure 22: Wheatstone Bridge Circuit

A Wheatstone bridge measures an unknown electrical resistance by balancing two legs of the circuit. By applying a constant excitation voltage to the circuit, the corresponding change in the output voltage provides a direct measure of the strain. In this study, the strain gage unit was equipped with two internal Wheatstone half-bridge circuits. Each bridge was completed by a signal conditioning amplifier unit. For a cantilever beam arrangement, the output voltage for a bridge circuit is,

$$E_o = E_i \cdot GF \cdot \varepsilon \qquad \textbf{Equation 8}$$

where E_o is the output voltage and E_i is the excitation voltage. A relationship between the applied forces and the output voltage reading of the gage is obtained through a calibration. This is an essential step in the measurement of shear stress as will be seen in a later section.

3.3.2. Strain Gage Thermal Effects

Electrical resistance strain gages are very sensitive to temperature variations. This is true for a multiple of reasons. One is the inherit change in resistance of the system due to a change in temperature. This effect could potentially be on an order of magnitude equivalent to the resistant changes due to strain of the small displacements one is trying to measure. For commercial strain gages, the sensitivity of resistance to temperature is specified by the temperature coefficient of resistance (TCR). The TCR rating for the gage used in this study is $\pm$ 0.01%/K (0.03%/°R) at full scale deflection. This relationship is not linear, but the manufacture provides a polynomial coefficient correction curve to correct the output due to temperature for a 55 K (100 °R) range.

Another reason strain gages are susceptible to temperature errors is due to mismatch of thermal expansion rates. These rates vary between the strain sensors, adhesive backing, and the specimen to which they are bonded. Therefore, the strain sensors will experience loading if the beam expands thermally at a rate greater or a slower than the strain sensors themselves, even if the beam is unloaded.

There are a few methods by which to compensate for these temperature effects. In self-temperature compensation (STC) gages, alloys with very low thermally induced strain properties are used for the gage wire. The alloys Constantan and Karma are the two most common materials for this application. Another method is to use a dummy gage in a half-bridge or full-bridge Wheatstone configuration. Since paired bridge components are affected by temperature change in the same way, the ratio of resistance does not change and thus the output voltage does not change as well. Lastly, it is possible to include temperature changes in the gage calibration, as is present in Section 3.6: *Gage Calibration*.

3.3.3. Strain Gage and Selection

The strain gage system that was selected for this research was the Deflection Sensor Cartridge (DSC) manufactured by Kistler-Morse [52]. These units have been used successfully in some earlier skin friction gages at Virginia Tech. The DSC is a fully customizable, complete multipurpose displacement transducer, factory tested and ready for installation. It has many features and advantages that make it superior in most respects to other types of transducers and sensors. This point is creatively illustrated in Kistler-Morse's cartoon feature shown in Figure 23. Overall, the unit is a very good fit for the application at hand.

Figure 23: Kistler-Morse Marketing Brochure [52]

First and foremost, the DSC is a commercial off-the-shelf product ($COTS$) offered at an affordable price. This relieves the tedious work of attaching strain gage sensors to the cantilever beam and the overall assembly of such a meticulous device. Secondly, the unit is small enough for this study's application. It has a maximum length of 38.1 mm (1.5 in) and max diameter of 6.4 mm (0.25 in). Lastly, the DSC is extremely sensitive while maintaining high precision control, yet stiff enough so that the movement of the floating element is minimal. Overall the unit remains very simple. There are no discontinuities, quadratures, dead bands, wipers, sliders, or bearings to distort the output data. The particular model used in this research was the DS-6AB4-210 (DSC-6) as shown Figure 24.

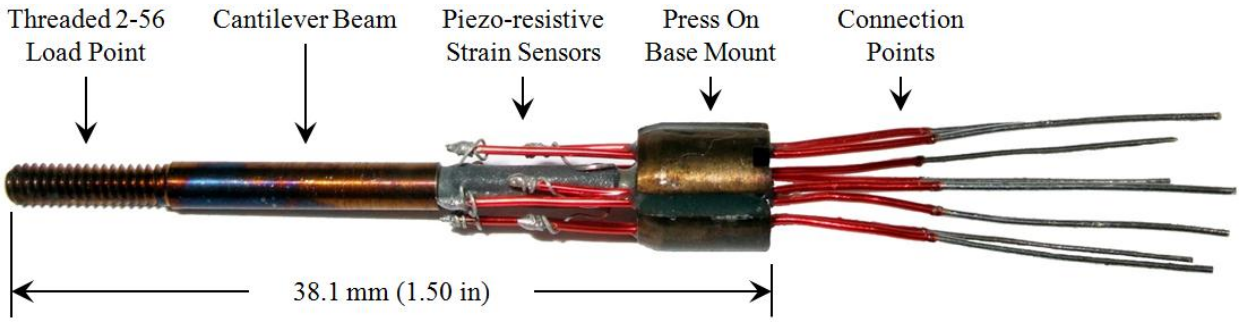

Figure 24: Kistler-Morse *DSC*-6 Unit

The DSC-6 is equipped with a press-on base mount and a 2-56 UNC-3a threaded load point. It has two, bi-directional axes with a 90° $\pm$ 2° offset capable of measuring displacement in two orthogonal directions simultaneously. Each axis is composed of two 1,000Ω strain gages to make up the half-bridge variable piezoresistive strain sensor which transforms mechanical displacement into a resistance change. A full Wheatstone bridge was completed through a Measurements Group 2310 signal conditioner. The DSC is constructed so that the strain sensors undergo tension and compression simultaneously to assure continuous linearity $\pm$ 0.05%. The unit has a maximum full-scale tip deflection of $\pm$0.305 mm (0.012 in). Deflections beyond its maximum capacity will damage the gage and render erroneous results. The projected gap size between the floating head and surrounding collar, 0.127 mm (0.005 in), serves as a stopper to prevent unexpected deflections. The standard operating temperature range is from 200 K (360 $°R$) to 505 K (910 $°R$) with a $\pm$ 0.01 $\%/K$ (0.03 $\%/°R$) null stability. The thermal envelope can be expanded to 755 K (1,360 $°R$) with an optional ceramic encapsulate to thermally protect the strain sensors. However, the encapsulate was not used due to previous problems in which it would swell up when exposed to oil and thus preload the gage.

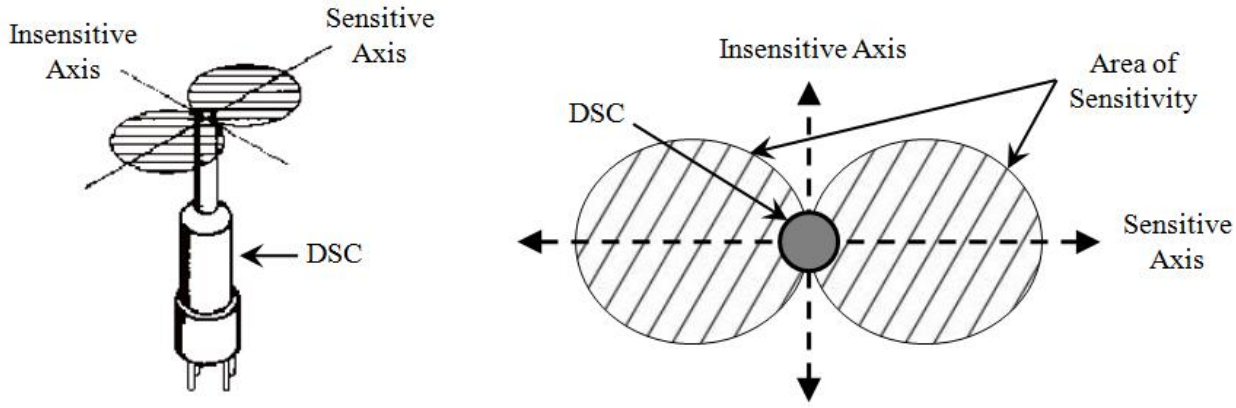

Figure 25: Sensitivity Regions of one of the Single Axes on the *DSC*-6 Unit

The *DSC* possesses regions of sensitivity along both strain gage axes. As shown in Figure 25, sensitivity of one of these axes is dependent upon the gage orientation and does not produce exact two-dimensionally orthogonal output components. The best results come from orienting the gage in which one axis is aligned with the expected flow direction to measure the full magnitude of the shear stress while the other axis is perpendicular. Finally, it must be noted that Kistler-Morse no longer makes *DSC* units as a standard item. The units in this study had to be specially ordered.

3.4. Head Deflection

An important assumption used for the analysis of all gages in this research was that the linear relationship devised between the deflection at the head and the force exerted on the *DSC*. The head component acts as a cantilever beam extension due to the fact that it is much stiffer than the *DSC* and is securely mounted in place. Thus, any deflection beyond the end of the *DSC* is assumed linear. Kistler-Morse models the *DSC* as a mass spring damper system and states the *DSC*-6's spring constant (k_{DSC}) as 8,750 N/m (50 $lb_f/\ in$) [52]. The deflection of the *DSC* is therefore determinable and related to the deflection at the head of the gage through a few simple relations. The relationship between the *DSC* and head is illustrated in Figure 26.

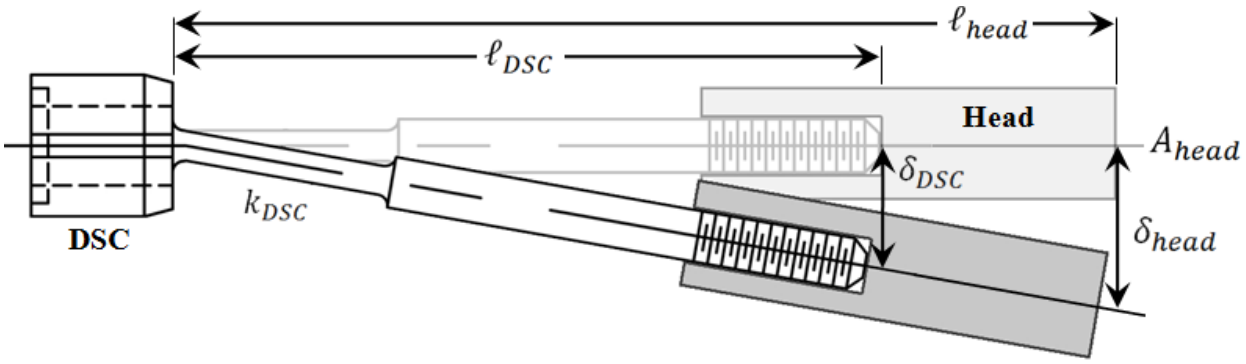

Figure 26: Gage Sensor - Head Deflection Relationship

In order to calculate the deflection of the head (δ_{head}), the measured force at the end of the head is first transferred to a moment at the base by its length (ℓ_{head}). The force is the product of the shear stress (τ_w) and surface area of the head (A_{head}). The base moment can then be transferred back to an equivalent force experienced at the end of the DSC by the moment arm (ℓ_{DSC}). The deflection of the DSC is then calculated using the known spring constant. Finally, using equivalent triangles and the small angle approximation, the deflection at the head can be deduced using Equation 9.

$$\delta_{head} = \left(\frac{\ell_{head}}{\ell_{DSC}}\right)^2 \left(\frac{\tau_w \ A_{head}}{k_{DSC}}\right) \qquad \textbf{Equation 9}$$

As mentioned before, a non-nulling gage design must minimize head deflection to control measurement uncertainties. Additionally, knowing the deflection is vital to ensuring the safety of the gage. The resulting head deflection due to the anticipated shear stress levels ($\delta = 10^{-3}\ mm$) is below the deflection threshold. However, deflection due to undamped vibrations could potentially reach a higher order ($\delta = 10^{-1}\ mm$). Such severe deflections could have the head impact the housing or exceed DSC's maximum deflection limit. Therefore, deflections of this magnitude need to be predictable in order to avoid concerns pertaining to measurement and survivability.

3.5. Bellows

The incorporation of a bellows provides a protective shroud in which to contain the oil to the interior cavity of the gage. This configuration protects the strain sensors from convective heat transfer while allowing nearly unconstrained motion of the overall system. The bellows that were chosen for this research are $COTS$ products manufactured by Servometer [53]. Servometer is the foremost manufacturer of electro-deposited nickel bellows and their special nature makes them well suited for precision instrument applications such as this. A general assortment of Servometer bellows is shown in Figure 27.

The electro-deposited nickel manufacturing process allows for greater control over the bellows size and wall thickness than any other process. Servometer bellows can be made as small as 0.5 mm (0.020 in) outer diameter with a wall thickness as thin as 0.0076 mm (0.0003 in). This makes the bellows extremely flexible where normally such designs are stiff and useless for sensitive applications. The maximum operating temperature is about 450 K (810 $°R$) at which point the nickel embrittles. This limit is never reached as the bellows is to be buried within the housing and in contact with the oil. The bellows is seamless and non-porous, thus no dirt or moisture can lodge in seams and cause contamination in critical applications. Lastly, despite the intricate manufacturing process Servometer bellows can be purchased in low quantities and at reasonable prices.

Figure 27: Servometer Assorted Bellows [53]

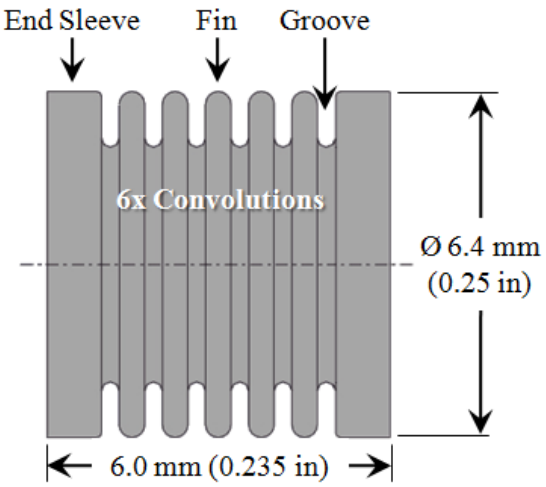

Figure 28: Bellow Model FC-4-L

The particular bellows model used in this research was the FC-4-L as shown Figure 28. It is small as dimensioned, has six convolutions, and a nominal wall thickness of 0.038 mm (0.0015 in). The model was chosen based on the geometric design space constrained by the DSC and ideal head shape.

The success or failure of this bellows application depended on the proper procedure for integrating it into the rest of the gage. The goal was to seat both end sleeves of the bellows into the well and lip contours located on the head and housing of the gage. This had to be done carefully without compromising the integrity of the components and must completely leak proof the interior cavity. Component alignment and preloading were also concerns. Two methods were used throughout this study: solder and epoxy. The attachment point and general assembly are illustrated in Figure 29.

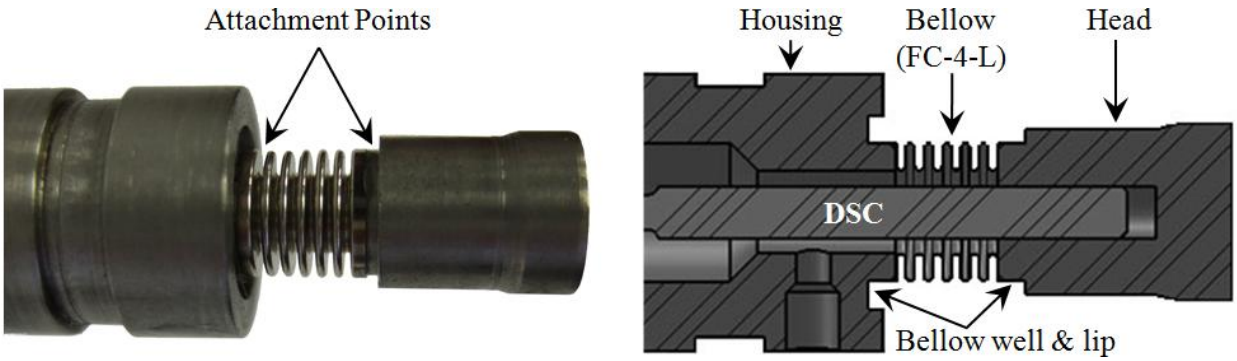

Figure 29: Bellow Application: Physical Gage (left), and CAD Drawing (right)

Soldering is an extremely delicate process since there was little room for error between the melting point of the solder and the temperature limit of the bellows. This was outsourced to Servometer as they were better equipped and more knowledgeable on the subject. High quality silver solder (95/5) was selected for its ability to work with nickel and stainless steel. The process was done without the DSC inserted to prevent any damage to the unit. Lastly, Servometer leak tested the attachment points to $10^{-9}\ cc/sec$ of Helium with a mass spectrometer. The equivalent rate amounts to one cubic centimeter of helium leaked over 32 years. The alternative method to attaching the bellows was with high-temperature epoxy. This was only done for the housing component, which was the further of the two attachment points away from hot flow. The high-temperature epoxy proved to be an effective method and could be conveniently performed in house.

3.6. Gage Calibration

The skin friction gages were calibrated for static wall shear by means of a hanging point mass system. The gage was secured horizontally so that the desired calibration axis was in the vertical direction and parallel to gravitational forces. A piece of string was taped to the top center surface of the head and a miniature paper “bucket” was attached to the opposite end. This configuration is sketched in Figure 30.

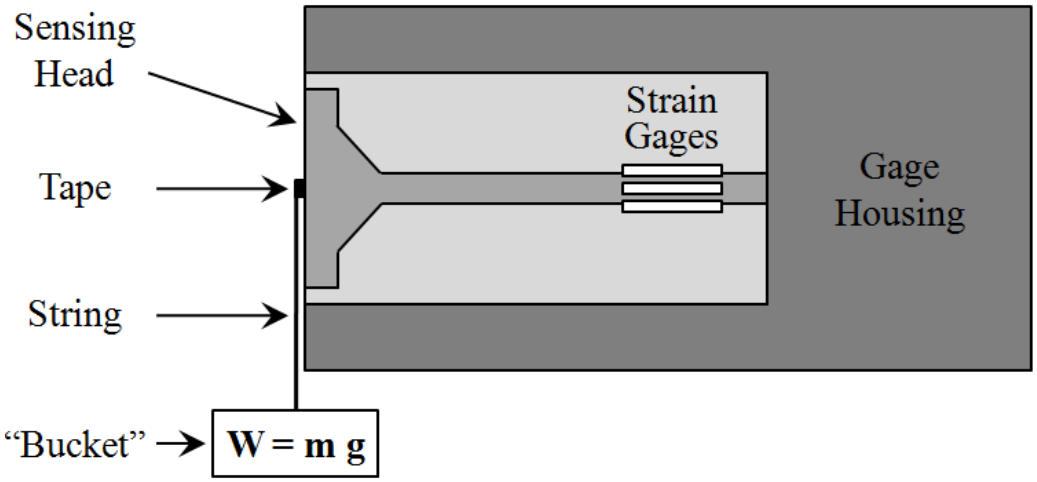

Figure 30: Static Wall Calibration Setup

The voltage output of the DSC was monitored and recorded by the data acquisition system. The sideways positioning of the gauge as well as the minute weight form the tape, string, and bucket were accounted for by zeroing (balancing) the signal conditioners prior to adding the calibration weights. Known mass standards ranging from 200 to 5,000 mg were then placed in the bucket to simulate wall shear stress. This process was carefully performed to prevent any form of pendulum action which would have moved the load vector off the measurement axis. Several tests were conducted while varying the amount and order of mass standards to verify no hysteresis was present and the data variance was minimal. The gage was rotated and calibrated through all of the four primary deflection axes ($+X, -X, +Y, -Y$) to ensure the gage was insensitive to the load application direction.

The hanging point mass calibration reveals a curve fit in the units of volts per gram of mass applied. This correlates to the desired units of volts per Pascal of shear force through,

$$\tau_w = \frac{m \cdot g}{A_{head}} = a \cdot E_o \qquad \textbf{Equation 10}$$

where a is the calibration constant, E_o is the total change in output voltage, and A_{head} is the surface area of the head. The equivalent wall shear stress is thus equal to the hanging mass multiplied by gravity all divided by the area of the sensing head.

An example of a typical calibration curve is shown in Figure 31. The plot reveals the relationship between output voltage and wall shear in both directions of each axis. The least-squares regression of the curves makes it evident that they are highly linear with an R^2 value equal to one and variance on the order of 10^{-4}.

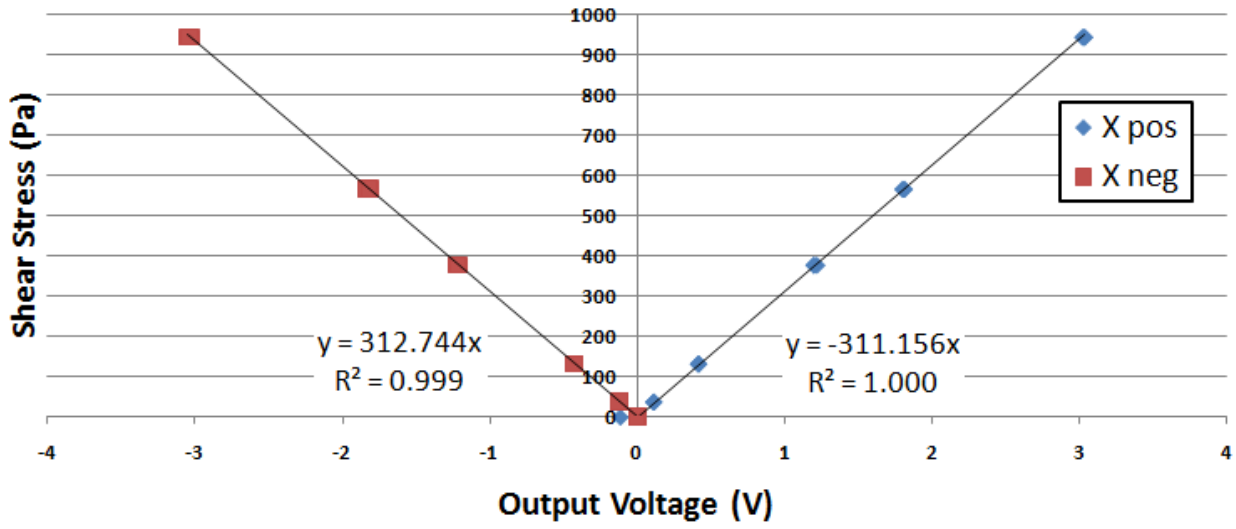

Figure 31: Shear Stress Calibration

Calibrations were performed on all iterations of the gage. This was done to observe if the sensitivity of the sensor changed under various conditions. The first calibration comparison was done before and after the gage cavity was filled with oil. No noticeable difference in the gage measurement outputs were detected between either of the cases.

The second calibration comparison was performed both with and without the active cooling system in operation. The strain sensors, did in fact, show sensitivity to various temperature conditions, thus a new calibration curve was devised. The active cooling system was used to flush hot water around the base of the DSC. Once a steady-state temperature was

reached, a shear stress calibration similar to Figure 31 was conducted. This was repeated at various gage base temperatures ranging from 291 to 301 K (524 to 542 $°R$). The slope of the calibrations curve for each individual trial is plotted against the recorded base temperature as seen in Figure 32.

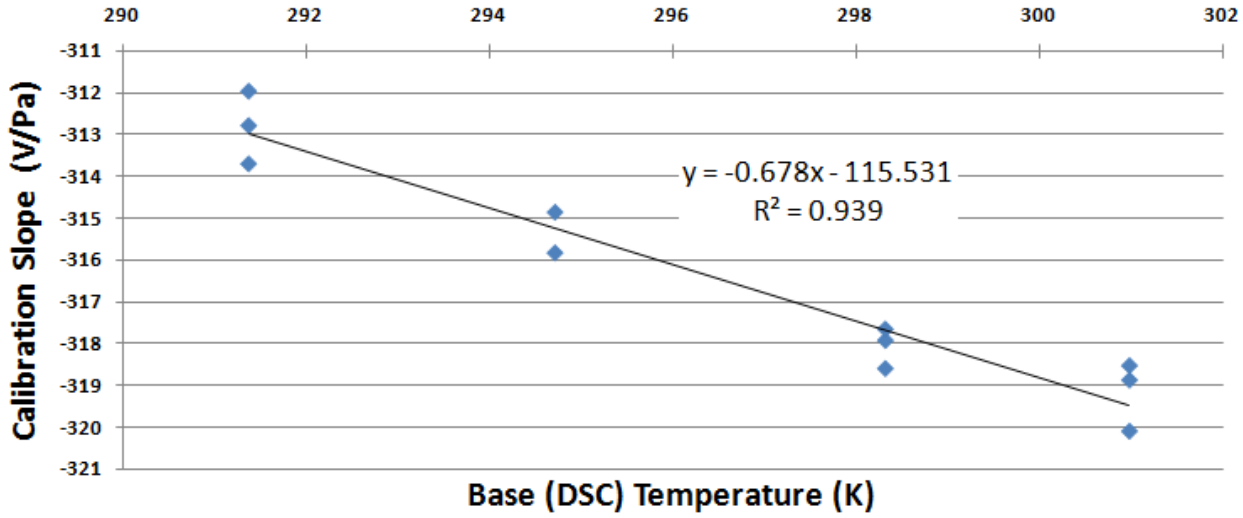

Figure 32: Improved Shear Stress Calibration with Temperature Compensation

Figure 32 illustrates the new calibration slope and makes the sensitivity of the strain sensors to various temperature conditions evident. The original calibration equation can then be updated to include the new temperature confiscation data, where the calibration constant a is now a function of T_{DSC},

$$a = (T_{DSC} \cdot b + c) \qquad \textbf{Equation 11}$$

where b and c are the calibration constants. Thus Equation 10 becomes,

$$\tau_w = \frac{m \cdot g}{A_{head}} = (T_{DSC} \cdot b + c) \cdot E_o \qquad \textbf{Equation 12}$$

3.7. Oil Fill

Oil filling the gage is a simple in principle, yet sensitive, procedure. The goal is to evacuate all traces of air within the gage by replacing it with oil and sealing it within. In traditional oil fill methods, the gage is placed in the oil before a vacuum chamber is pumped down. In order for the method to work, the air must flow out while the oil flows in. This is accomplished by having more than one port or a large enough gap for simultaneous flow. Consequentially, it was much harder to seal the gage or, in the case of the gap, the gage cannot be sealed at all. Additionally, due to air/oil interference, air bubbles have a tendency to adhere to the interior surfaces of the gage. This can be overcome by vibrating the entire chamber and cycling the vacuum process several times. The air bubbles will eventually detach from the surfaces, but they have the potential of still getting stuck if there is not a direct path to escape. The interior of the gage thus had to be simple and designed for these additional constraints.

It was clear that traditional oil fill methods would not be suitable for this research. A new method had to be devised. The gage was oil filled by implementing an intuitive process and equipment developed by Luna Innovations. This procedure is depicted in Figure 33.

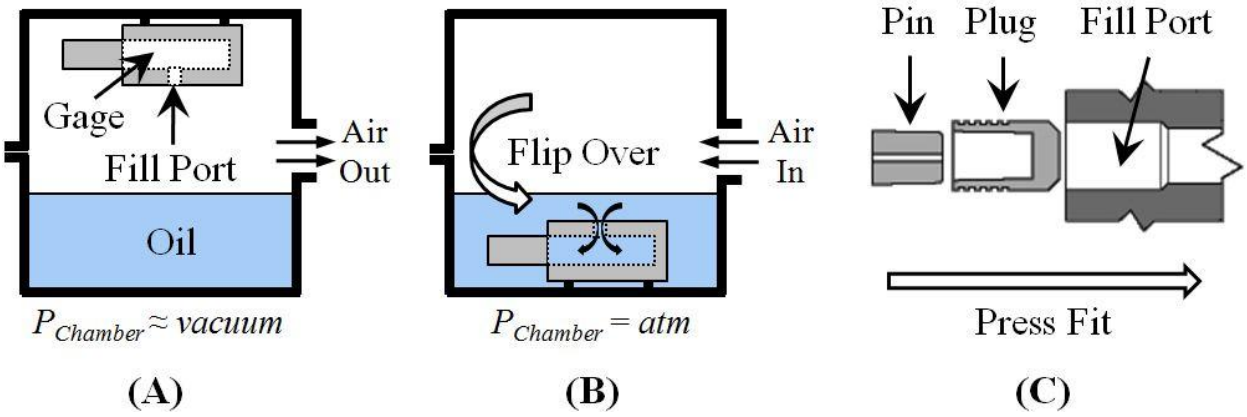

Figure 33: Gage Oil Fill Procedure

The Luna Innovations vacuum chamber is composed of two primary sections: a top and a bottom as shown in Figure 34. The gage is secured to the top half with the oil fill port facing outward and the bottom half is filled with a few inches of oil, as depicted in Figure 33A. MultiTherm PG-1 mineral oil was used in this study [59]. The two halves are then sealed together and the pump is engaged. Air and moisture are extracted out of the complex interior of the gage and outgases from the oil as the chamber reaches near vacuum conditions. Ideally, this step should be performed for at least two days to ensure the chamber is thoroughly void of any contaminants.

The chamber is then flipped upside down, so that the gage is immersed in the oil as seen in Figure 33B. Oil will begin to settle into the gage through the oil fill port. After an hour, the pump is then shut off and the chamber is slowly bled back to atmosphere to prevent any violent disruptions in the oil. Any remaining vacuum pockets within the gage will be immediately replaced by oil due to the now present pressure differential across the reservoir and the interior of the gage.

The final step is to plug the oil fill port while the gage is still under the oil to ensure no air bubbles enter the interior. This was done by gently pressing a *LeePlug* pin and plug system [60] into place as shown in Figure 33C. The *LeePlug* has the advantage of being extremely small ($\emptyset = 2.36\ mm$), effective at high pressures ($p = 100\ MPa$), and easy to install. Finally, the gage may be removed from the oil, cleaned, and made ready for use.

Figure 34: Luna Innovation Vacuum Chamber

Figure 35: Virginia Tech Vacuum Chamber

After the gage was filled with oil, it was tested for remnant air bubbles in the Virginia Tech vacuum chamber as shown in Figure 35. The chamber was equipped with a pressure line and electrical interface for the gage. As the air was pumped out, the pressure level and strain gage outputs were monitored by the data acquisition system. Since the gage was not exposed to shear stress, any variation in the strain gage readings would correlate to internal pressure forces imposed by air bubbles. If the gage remained unaffected under the vacuum, it was deemed ready for wind tunnel testing.

4. General Facilities and Instrumentation

Chapter 4 describes the general facilities and instrumentation used throughout this study. It also provides the specifications, layout, and flow properties for the Virginia Tech Hypersonic and $AEDC$ Arc-Heated Facilities. Lastly, the chapter presents information on the measurement devices and electrical equipments used to obtain and analyze the experimental data in detail.

4.1. Virginia Tech – Hypersonic Tunnel

The small-scale, blow-down, Hypersonic Tunnel (HST) at Virginia Tech is designed to provide supersonic and hypersonic flows through the range of Mach 2 to 7 [61]. A schematic of the facility is shown in Figure 36. The duration of the run varies on an order of about 2 to 3 seconds and depends weakly on the test conditions. Due to the blow-down nature of the tunnel, during a run the flow stagnation pressure and temperature decrease slowly while relative flow parameters and Mach number remains constant. This facility was obtained through our close and long-term collaborations with the Institute of Theoretical and Applied Mechanics of the Russian Academy of Sciences in Novosibirsk, Russia [62].

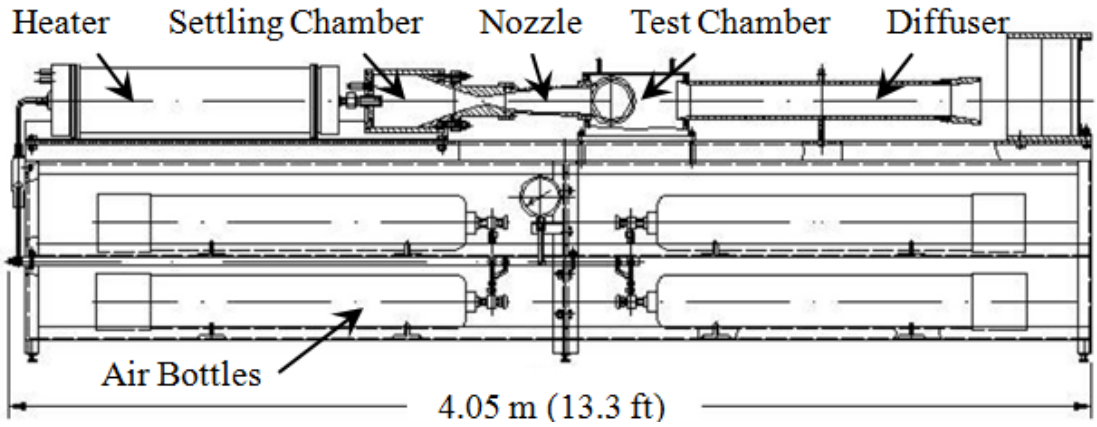

Figure 36: Schematic of the Virginia Tech Hypersonic Wind Tunnel [61]

The air (or other working gases) is supplied by a high-pressure compressor and stored in eight bottles under the frame with a total volume of 320 dm^3 (11.3 ft^3) and maximum pressure of 15 MPa (2,175 psi). During a run, the airflow is regulated by a time control device which enables the fast-acting control valve. Air flows from the bottles through the electric stove heater and into the plenum chamber. The heater is capable of heating the flow stagnation temperature up to 800 K (1,440 $°R$) to prevent condensation at hypersonic speeds. From there, the flow passes through an interchangeable converging-diverging nozzle and into the tech chamber with the inner dimensions of 300 × 100 × 60 mm (11.8 × 3.9 × 2.4 in). Finally, the air moves out through the diffuser, dispersed through a splash-plate, and is ventilated outside.

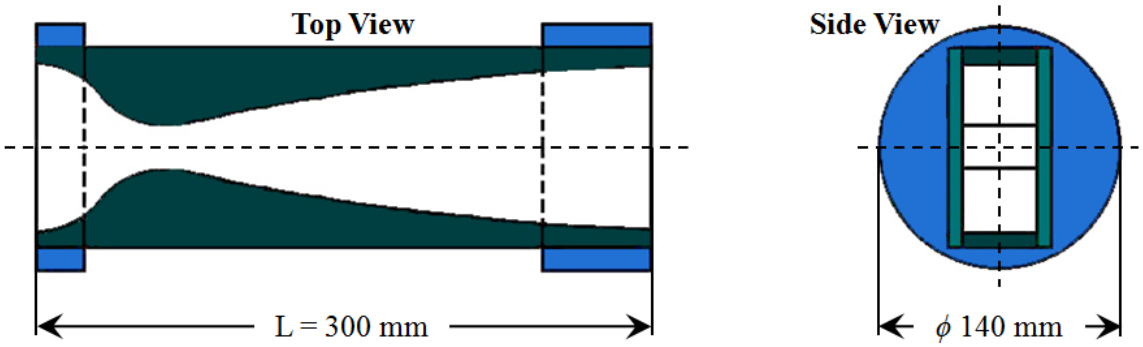

Figure 37: Mach 3 – *HST* Rectangular Nozzle

For this research, the tunnel was equipped with a rectangular converging-diverging nozzle to achieve a nominal Mach 3 flow in the test chamber as shown in Figure 37. The rectangular shape simulated a two-dimensional flow condition and provided a level surface to integrate the flat plate on to. The electric heater was used to simulate various high-enthalpy flow conditions up to 655 K (1,180 $°R$).

4.1.1. Hypersonic Tunnel Gage Setup

The gage is set up through the bottom of a flat-plate so that the head is flush with the flow surface. Its centerline is offset 25.4 mm (1.0 in) back from the edge of the nozzle. A nozzle extension is fitted over the length of the plate to maintain a constant cross-sectional area ratio and to prevent the tunnel from un-starting. This setup is depicted in Figure 38.

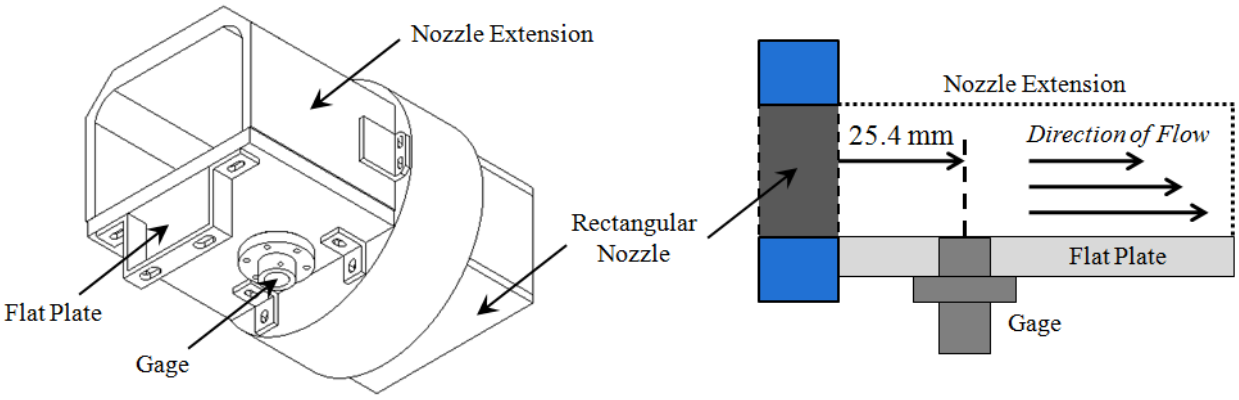

Figure 38: Hypersonic Wind Tunnel Setup

Two J-type thermocouples are incorporated into the gages. Both are ungrounded sheathed MTSS series probes from Omega [63] capable of a 5 Hz response rate. The locations of the thermocouples within the PT-2 gage are shown in Figure 39.

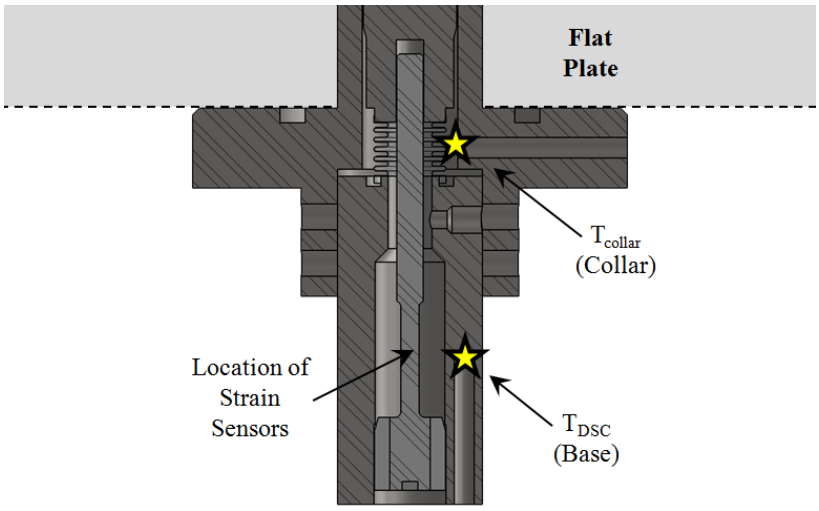

Figure 39: *PT*-2 Thermocouple Placement

Due to physical limitations, both thermocouples could not directly measure the temperature in the regions of most interest but were close enough to serve as approximate representations. The first thermocouple is located in the base near the highly sensitive strain sensors of the DSC. The second thermocouple is located in the air gap around the bellows region and closely mimics the temperature of the collar approximately 12.7 mm (0.5 in) below the surface.

4.1.2. Boundary Layer Survey Equipment

Boundary layer survey equipment consists of a triple-rake, traverse, and a control system. The traverse moves the triple-rake from nearly flush with upper nozzle wall to about 6.5 mm (0.25 in) below the wall. This is conducted through the top of the HST test cabin and is sealed off by rubber gaskets.

The traverse is a BiSlide twin rail precision positioning system made by Velmex [64]. It has dual axis capabilities though only the vertical axis is used for boundary layer surveying. The system is driven by a Vexta 2-Phase stepper motor [65] rated at 1.8° per step. This relays the traverse slide at 0.0025 mm (9.8×10^{-5} in) per step and velocity at about 10 mm (0.4 in) per second. The traverse is controlled by a Velmex VXM stepper motor controller [66]. It is operated through manual joystick control as well as remote operation via the automated tunnel control program.

A sequential control loop moves the traverse at incremented steps and records its actual position. The duration the traverse is paused at a sample point depends on the response time of the measurement equipment. The triple-rake samples for 200 milliseconds at 500 Hz. During a 3.2 second run in the HST, five sample points are measured.

The triple-rake measurement system consists of two pressure probes and one temperature probe as seen in Figure 40. From left to right, the first item is the cone-static probe. It consists of a hollow tube capped with a 9.5° half-angle axisymmetric copper cone connected to a pressure transducer. Four small pressure ports are located around the surface of the cone with an interval spacing of 90° to reduce the misalignment effects with respect to the flow. The remaining two probes both have a small flat opening at the tip of the tube to produce a standoff normal shock. The center probe measures total temperature and has a Type-E thermocouple inside. This probe is lined with bleed holes behind the thermocouple in order to obtain a high recovery factor. The last item is the Pitot probe which connected to a pressure transducer that measures the total or stagnation pressure. The outer diameter of the three probes is 1.7 mm (0.07 in) and they are separated by 7.0 mm (0.28 in) from centerline to centerline. The overall dimension of the triple-rake head is 82 mm (3.2 in) by 32 mm (1.2 in). Figure 41 shows the triple-rake and traverse in the test section of the wind tunnel.

Figure 40: Triple-rake Equipment

Figure 41: Triple-rake in Wind Tunnel

The local Mach number is derived from the Pitot and cone-static probe measurements according to the Rayleigh-Pitot formula and polynomial curve fit solution of the Talyor-Maccoll equation. Relations the sample point displacement to the local Mach number yields the

boundary layer profile. All other flow quantities are determined from compressible flow and boundary layer flow relationships.

4.1.3. Electronics

Several measurement devices to include thermocouples, pressure transducers, and strain gages were used to obtain the experimental data in the Virginia Tech HST. The output voltages of these devices are amplified by Measurements Group 2310 signal conditioning amplifiers [67]. The amplifier units were capable of an excitation voltage range from 0.7 to 14 DC V, and a signal amplification Gain from 1 to 11,000. They are equipped with a low-pass Butterworth signal filter with cut-off frequencies of 10, 100, 1,000, and 10,000 Hz, a Wheatstone bridge completion feature, and auto-balancing feature.

BNC cables connect the amplifiers to a National Instruments PCI-MIO-16XE Data Acquisition (DAQ) board which was capable of sampling the data at a rate of 500 Hz [68]. The DAQ board, used in conjunction with a National Instrument AMUX-64T multiplexer-board, offers 64 analog and 16 digital input and output ports. The DAQ board is equipped with a cold-point-junction and is capable of reading out thermocouple data on analog input ports. The output voltages were interpreted through various Labview programs [69] and saved for further analysis. A block diagram of the electrical setup for the gage calibration, vacuum chamber test, and wind tunnel test is seen in Figure 42.

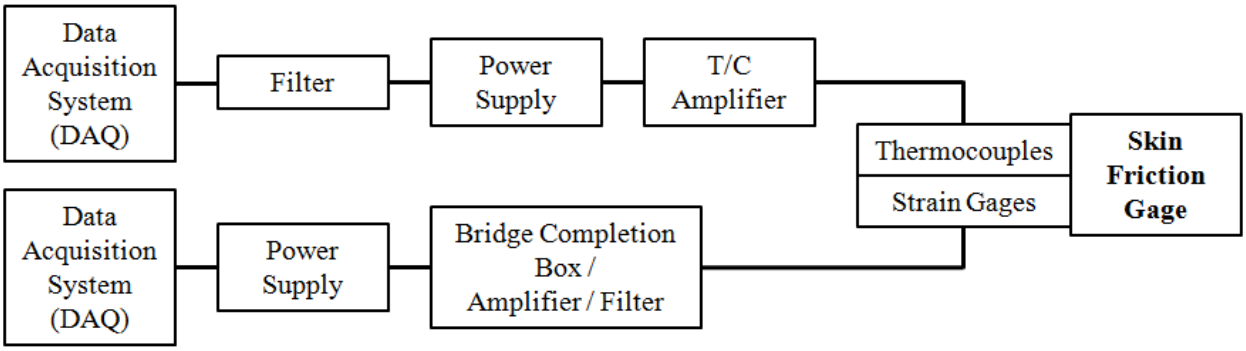

Figure 42: Block Diagram of Electrical Setup at the VT *HST* Facility

In this study, the DSC unit's dual Wheatstone bridges were completed with a pair of 2310 signal conditioning amplifiers. Since the skin friction gage was tested in similar flow environments and wall shear levels, the amplifier settings always remained the same. An excitation voltage of 10 V and an output Gain of 1,000 was applied to the DSC circuits. Higher excitation voltages would have improved the signal to noise ratio, however it was found that using an excitation in excess of 10 V caused signal drift due to self heating. A 10 Hz cut-off frequency on the low-pass Butterworth filter was used eliminate background electrical interference.

4.2. Arnold Engineering Development Center – Arc-Heater Facilities

The $HEAT$-H2 test unit at Arnold Engineering Development Center (also known as Linde) is a Huels arc-heated tunnel. A schematic of the $HEAT$-H2 configuration is shown in Figure 43. The working gas (generally air) is injected tangentially into the swirl chamber to generate a strong vortex spiral which provides arc stability. The working voltage across the magnetic spin coils around the anode and cathode sections exert a $J \times \beta$ torque on the arc discharge. This augments the swirl in the arc column and ensures a uniform radial distribution at the high heat flux zone in the arc-electrode contact site [21].

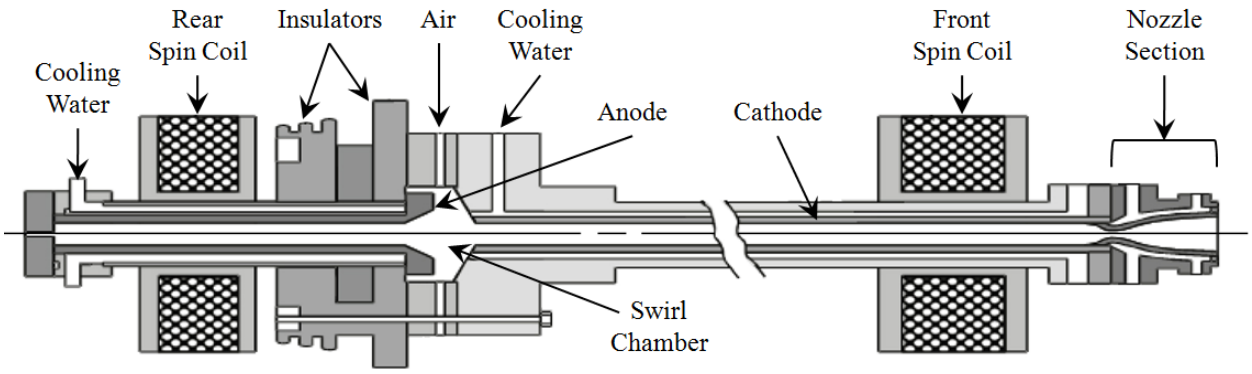

Figure 43: Schematic of the *AEDC HEAT*-H2 Huels Arc-Heater Configuration [21]

The H2 arc tunnel is evacuated by the Propulsion Wind Tunnel Plenum Evacuation System (PES) compressor plant and operates with a subatmospheric test cell. Test models are inserted into the tunnel by means of a water-cooled, five-strut, rotary model positioner system (MPS). The platform for the MPS is located directly behind the arc-heater tunnel as shown in Figure 44. The MPS features an axial drive to selectively position each test article into the test free jet under preset dwell times.

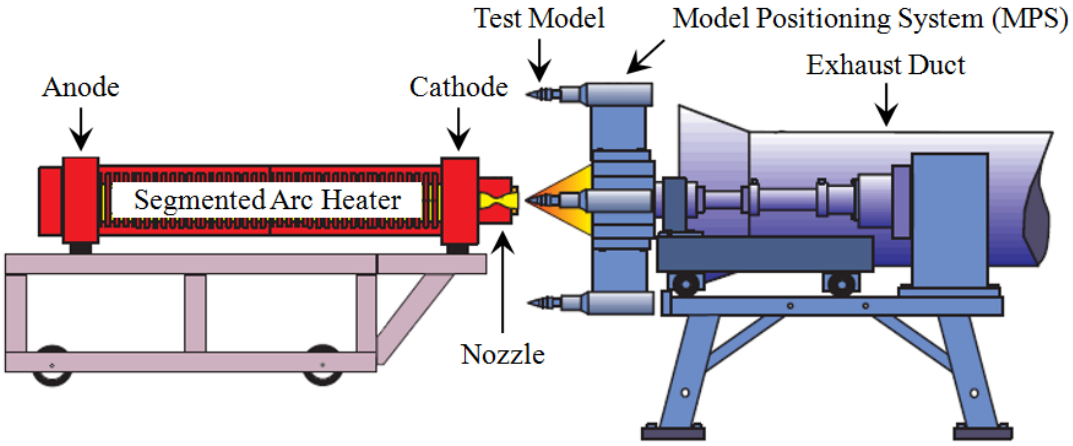

Figure 44: H2 Model Positioner System [21]

The skin friction-gage developed in this study will be tested on the Q3/Q4 15° wedge calorimeter platform depicted in Figure 45. The calorimeter is uncooled and is made of copper with a flat stainless steel test plate. It has an interior cavity to contain instrumentation and a

hollow sting to run accessories through. The Q3/Q4 will be mounted to the five-strut MPS and rotated in the flow for no more than one second durations.

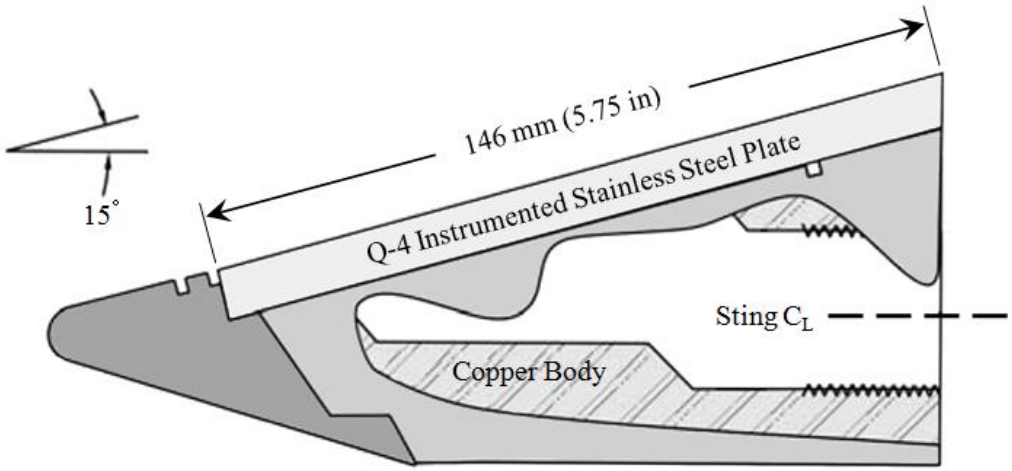

Figure 45: Q3/Q4 15° Wedge Platform and Test Plate [21]

5. Theoretical and Computational Approaches

Chapter 5 identifies theoretical and computational approaches to predict the performance of the skin friction gages. Shear stress in the Virginia Tech Hypersonic Tunnel is initially modeled by analytical and numerical methods. These estimations are based on known flow properties, measured boundary layer information, and computational fluid dynamics. The performance predictions set a foundation on which to compare and justify the experimental results.

5.1. Flow Properties

Different measurement devices were strategically placed to best understand the gage and flow properties over the entire test matrix. The temperature and pressure measurements of the flow were taken at the centerline of the nozzle, outside the viscous layer. The flow conditions in the *HST* at the various heater temperatures are displayed in Table 3.

Table 3: VT Hypersonic Tunnel Flow Conditions

T_{heater} (C)	20	100	200	300	400	500	600
T_{heater} (K)	293	373	473	573	673	773	873
$P_{o,1}$ (kPa)	760	820	860	910	960	980	1,020
$P_{o,2}$ (kPa)	250	270	290	300	320	330	340
$P_{e,2}$ (kPa)	31.5	33.5	35.9	37.3	39.3	40.4	42.0
$T_{o,2}$ (K)	276	348	412	470	530	590	655
Mach #	2.92	2.95	2.94	2.94	2.94	2.95	2.92

The *HST* control valve releases a constant and regulated mass flow of air during each run cycle. As seen in Table 3, the values of the flow conditions increase as the plenum heater temperature increases. The only condition that remains constant throughout the test series is the

Mach number with a nominal value of 3.0. The triple-rake survey was conducted nominally at the beginning of the plate.

Subsequent boundary layer (BL) growth can then be modeled as steady, flat-plate flow to the location of the gage. The triple-rake pressure ratio ($P_{o,2}/P_{e,2}$) was used as an indicator of the BL thickness as it remains constant outside of the viscous flow. Figure 46 summarizes the measured boundary layer results at various temperatures. At all of the flow conditions, the BL is approximately 3.5 - 4.5 mm thick. For the purpose of the skin friction estimations, the average BL thickness was estimated at 4.0 mm (0.16 in).

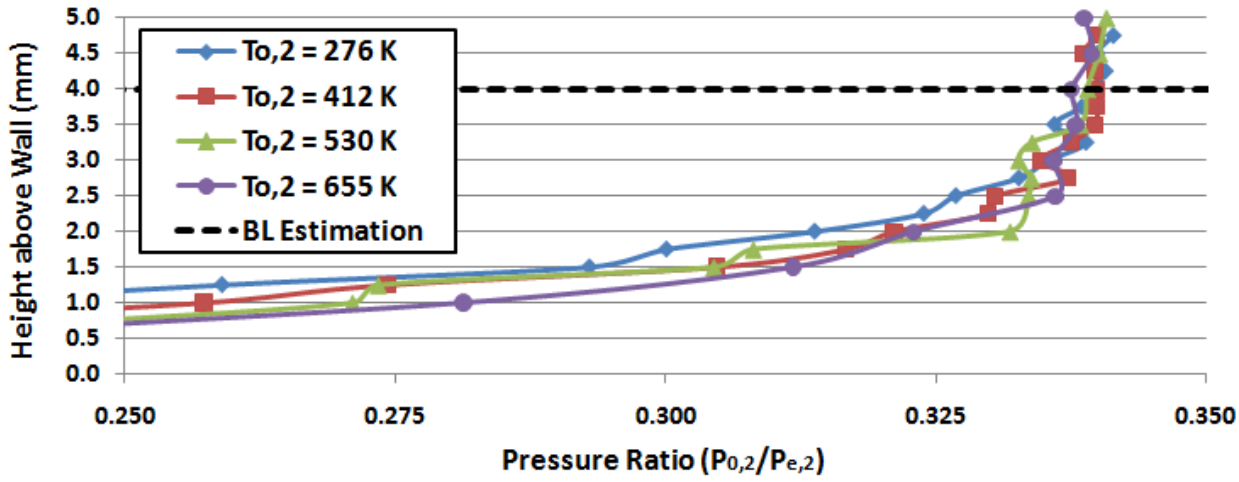

Figure 46: Boundary Layer Profiles

The thermocouple in the collar flange as seen in Figure 39 represented the plate wall temperature T_w. The T_w measurements during run cycles at various flow conditions are presented in Figure 47. In addition, the total plenum pressure of the wind tunnel is superimposed to indicate the run cycle.

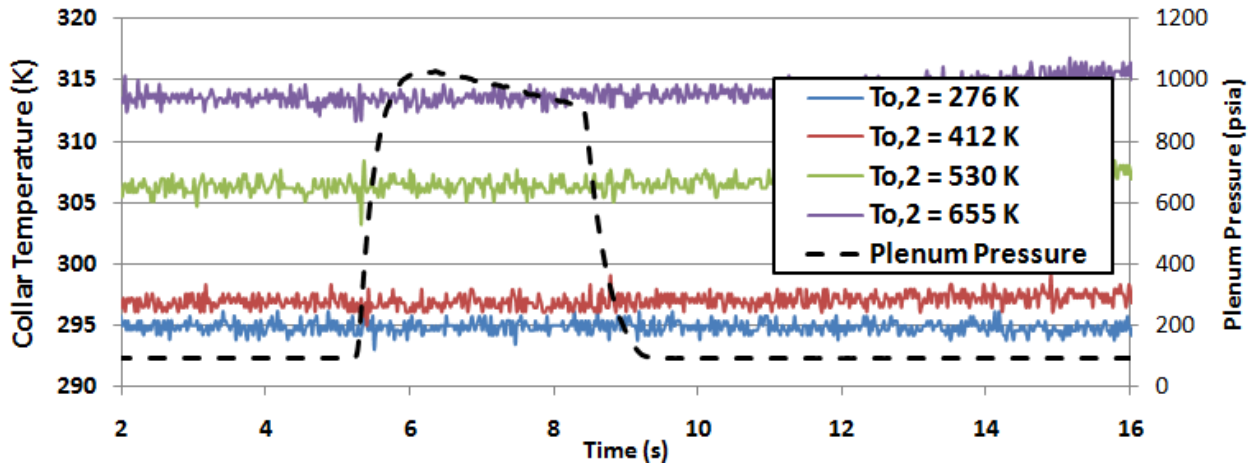

Figure 47: Wall Temperatures at Various *HST* Flow Conditions

The temperature reading in the collar remains constant over the test run period. Therefore, the heat flux is not significant enough to penetrate deeper than 12.7 mm (0.5 in) down from the surface during this time. However, as seen in the post run data, the collar does eventually warm up slightly. For example, at $T_{0,2} = 655\ K$ (954 $°R$), the collar experienced a 6 K (10 $°R$) increase from its initial stable temperature of 310 K (558 $°R$). Within 10 minutes of the run, the temperature returned to its initial starting point. Since the *HST* takes approximately 40 minutes to charge, this has no influence on consecutive test runs.

It is also important to note that the whole wind tunnel, composed of steel, conducts the heat produced by the active heater. As a result, the entire gage heats up as seen in both of the gage's thermocouple readings. Since the data is consistent for each flow condition, this is considered the stable temperature of the system.

5.2. Skin Friction Estimations

Skin friction estimations are derived through a series of calculations and approximations. This well-accepted approach for skin friction estimations is found in Appendix B: Equation Sets. Three analytical models were also utilized to predict skin friction: Van Driest II, Gersten-

Herwig, and Eckert. These methods predict the ratio between the constant physical properties (incompressible) skin friction $\left(C_{f-inc}\right)$ to the compressible skin friction $\left(C_{f-comp}\right)$ at the same Reynolds number. They are a function of Mach number, free-stream static temperature, wall temperature, and the recovery factor. Compressibility effects, high Reynolds number (turbulence), and heat transfer are all considered in each of the employed models. The generalized skin friction ratio is expressed in Equation 13 as the compressible turbulent boundary-layer transformation factor (F_c).

$$\frac{C_{f-comp}}{C_{f-inc}} = F_c \qquad \textbf{Equation 13}$$

The Van Driest II (1956) model was developed using the Von Karman mixing length model for incompressible flow and Crocco's turbulent relation [70]. The Eckert (1955) model is based on reference temperature concepts [24]. The Gersten-Herwig (1960) model relates the reference temperature to the film temperature, the arithmetic mean of the wall and outer temperatures [71]. The first factor F_c of the three correlations is as follows:

$$F_c \text{ (Van Driest II)} = \frac{T_{aw}/T_e - 1}{(\sin^{-1}\beta_1 + \sin^{-1}\beta_2)^2} \qquad \textbf{Equation 14}$$

where β_1 and β_2 are functions of temperature,

$$\beta_1 = \frac{T_{aw}/T_e - T_w/T_e - 2}{\sqrt{(T_{aw}/T_e - T_w/T_e)^2 - 4T_w/T_e}} \qquad \textbf{Equation 15}$$

$$\beta_2 = \frac{T_{aw}/T_e - T_w/T_e}{\sqrt{(T_{aw}/T_e + T_w/T_e)^2 - 4T_w/T_e}} \qquad \textbf{Equation 16}$$

the subscripts w and e indicating conditions at the wall and in the mainstream, respectively. Thus, T_e is the BL edge temperature, and T_w is the surface temperature, and T_{aw} is the adiabatic wall temperature. The remaining two F_c factors are:

$$F_c\ (\text{Gersten/Herwig}) = \left(1 + \sqrt[3]{Pr}\ \frac{(\gamma - 1)}{4}\ M^2\right)^{-1} \qquad \textbf{Equation 17}$$

$$F_c\ (\text{Eckert}) = \frac{T^*}{T_e} = \frac{(0.5)T_w + (0.22)T_{aw} + (0.28)T_e}{T_e} \qquad \textbf{Equation 18}$$

where T^* is the reference temperature, and Pr is Prandtl's number.

To further refine the skin friction estimations, an implicit numerical methods application for turbulent boundary layers was used in conjunction with the three analytical models. Compressible Turbulent Boundary Layer ($CTBL$) is a JAVA based computer code developed at Virginia Tech. The program is capable of producing boundary layer and thermal boundary layer growth models based on specified flow conditions [72].

The $CTBL$ applet served two purposes. First, it is capable of predicting the same flow conditions originally measured by the triple rake based upon the variable 2-D Mach number profiles in the nozzle as seen in Figure 48. Second, it is utilized to predict flow growth over the 1-D flat plate area from the edge of the nozzle to the location of the gage.

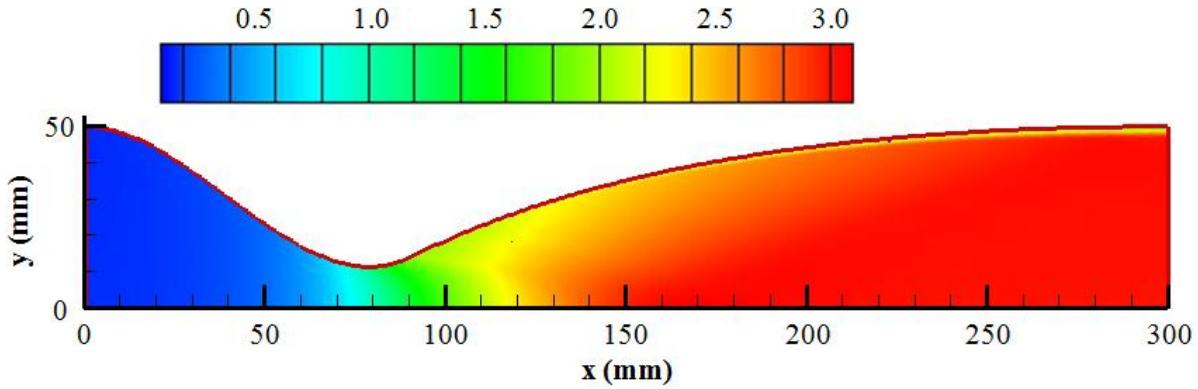

Figure 48: CFD model of Mach 3 Rectangular Nozzle of the VT Hypersonic Tunnel

Thus, six total estimations can be determined for a given set of flow conditions: three using the models based on the triple-rake data and three more using the models based on the CTBL data. Table 4 summarizes the different friction estimations for the Virginia Tech HST at a

flow stagnation temperature of 350 K (630 °R). Figure 49 illustrates the wall shear stress estimations over the entire test matrix range of temperatures.

Table 4: Skin Friction and Heat Flux Estimations for the VT *HST* at Mach 3, $T_{0,2} = 350\ K$

	Experimental BL Thickness			CTBL Applet Prediction		
	Van Driest II	Gersten - Herwig	Eckert	Van Driest II	Gersten - Herwig	Eckert
C_f	0.0014	0.0012	0.0011	0.0014	0.0012	0.0010
$\tau_w\ (Pa)$	201.5	172.1	154.9	197.3	168.5	151.7
$h\ (W/m^2 \cdot K)$	301.9	257.8	232.1	295.7	252.6	227.4
$\dot{q}_w\ (W/m^2)$	9,610	8,210	7,390	9,410	8,040	7,240

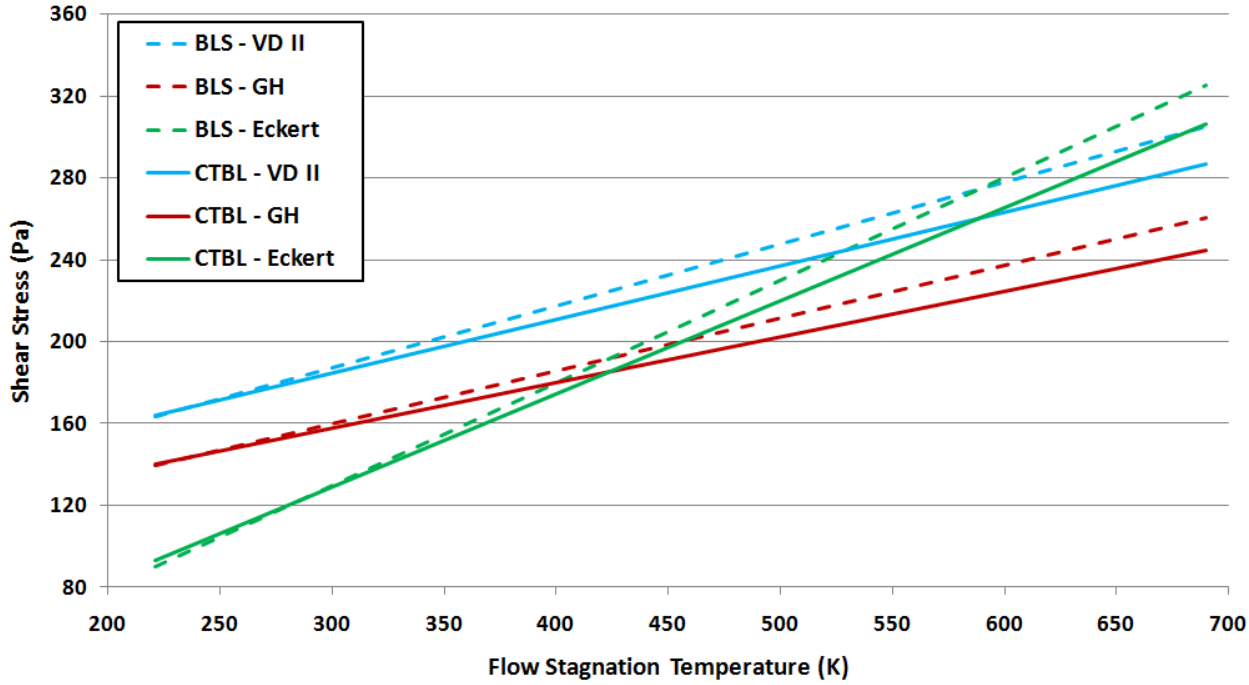

Figure 49: Friction Estimations for the Virginia Tech Hypersonic Tunnel at Mach 3

This study reveals how difficult it is to make accurate wall shear estimations. Even while using the exact same flow conditions, the three correlation models produce results that vary as much as 40%. Despite the differences in these estimations, these models do form a reasonable range of expected values with which to compare to the experiment's skin friction measurements.

This is greatly beneficial due to the fact that there is no previous skin friction test data for the Virginia Tech HST.

Compared to the relatively simple conditions found in the HST, the flow becomes increasing more difficult to model in high enthalpy flow facilities such as $AEDC$. Dissociation of the hot reacting flows breaks down the simpler transformation models as the perfect gas law no longer applies. Fortunately, the Eckert reference enthalpy method still holds and can be applied to the conditions expected at $AEDC$. Of course, modern CFD methods can also be applied.

5.3. Finite Element Model Analysis

The general-purpose finite element model (FEM) analysis package, ANSYS, was used to verify the conduction heat transfer throughout the gage as well as to make further predictions in high enthalpy flow. The software incorporates powerful pre-processing, solving, and post-processing modules. *ANSYS* has the ability to perform static/dynamic structural (both linear and non-linear), modal, spectral, thermal, acoustic, electro-magnetic, and computational fluid dynamics analyses. The thermal analysis in *ANSYS* is based upon the heat balance equation from the principle of conservation of energy. The finite element solution calculates nodal temperatures in which to obtain other thermal quantities. Before the software package was implemented, it was important to first analytically verify the approach, user input choices, and results.

Schneider [73] devised a solution to transient heat conduction problems for a simple, semi-infinite solid model with a constant film coefficient on the surface. The solution is expressed by,

$$\frac{T - T_i}{T_{aw} - T_i} = 1 - \text{erf}\left(\frac{x}{2\sqrt{\alpha\tau}}\right) - \left[\exp\left(\frac{hx}{k} + \frac{h^2\alpha\tau}{k^2}\right)\right]\left[1 - \text{erf}\left(\frac{x}{2\sqrt{\alpha\tau}} + \frac{h\sqrt{\alpha\tau}}{k}\right)\right] \quad \textbf{Equation 19}$$

where T is the local temperature, T_i is the initial temperature of the solid, and α is the thermal diffusivity of the material. The boundary conditions for the differential equation accounts for convective heat transfer at the surface with a constant heat transfer coefficient. This assumption holds in the Virginia Tech and $AEDC$ tunnels as well. The heat transfer coefficient is dependent upon the physical properties of the flow. Over the short period of a wind tunnel run, the flow conditions are nominally constant, therefore h can be safely assumed to be approximately constant. This solution was used to check corresponding solutions obtained with ANSYS.

A higher fidelity model of the PT-2 gage to be described later was constructed in *ANSYS*'s native drawing package. The FEM uses the thermal Solid 87 element, which is a 3-D, 10-node structural tetrahedral with quadratic temperature field interpolation. The grid of the model was produced using the smart mesh parameter in *ANSYS*. The tool creates smaller mesh elements in areas of potentially high stress concentration. The coarseness of the mesh was set to the value 1, which is the finest mesh available. The final grid for the PT-2 model consisted of 909,548 nodes. The element and grid size choices provided a balance between computer resources available, computational time, and accuracy. The final meshed model is shown in Figure 50.

A nodal solution of PT-2 simulated under the most adverse HST test conditions is seen in Figure 51. The flow has a stagnation temperature equal to T_0 = 655 K (1,180 °R) with a constant heat transfer coefficient equal to $h = 275\ W/m^2 \cdot K$ (48 $Btu/hr \cdot ft^2 \cdot °R$). Boundary conditions were selected from the HST experimental flow analysis described in Chapter 5.2: *Skin Friction Estimations*. The model's initial state was set to the calibration temperature of 294 K

(529 °R). The convective heat transfer was evenly distributed across the top surface. The analysis identifies the thermal conditions three seconds after the beginning of the test run.

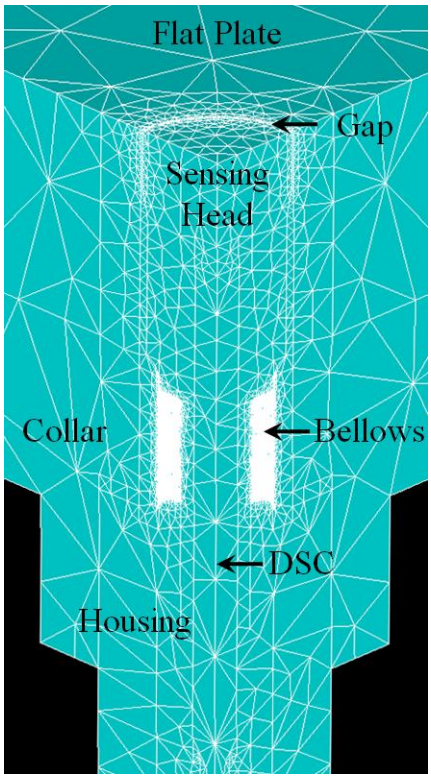

Figure 50: *ANSYS* Grid used for *PT*-2

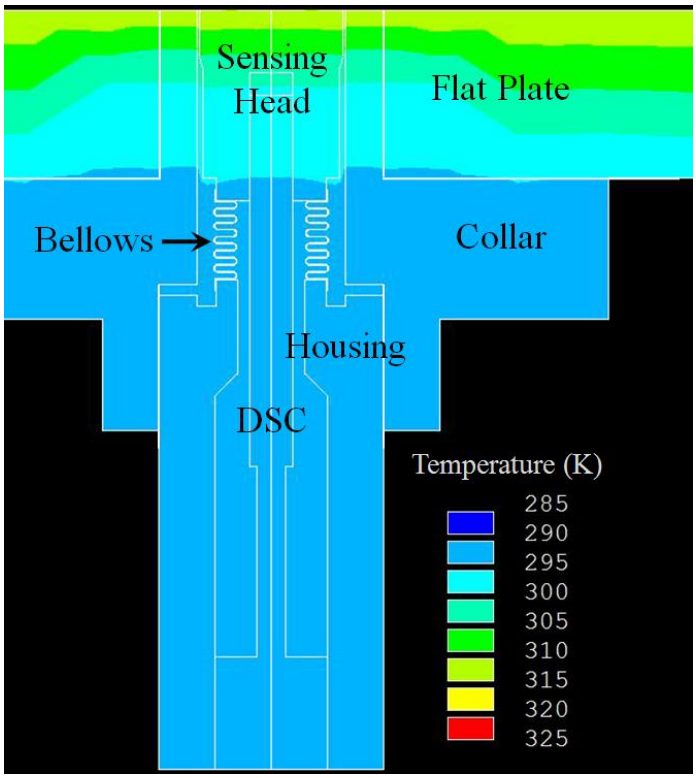

Figure 51: Nodal Solution *PT*-2 *HST* at $T_{0,2} = 655\ K$

Even in the HST worst-case scenario, the thermal penetration barely reaches the base of the sensing head. This leaves the sensitive components of the gage untouched, the bellows, and DSC. These predicted values agree closely with the two thermocouple readings from the HST experimental flow analysis and Schneider's analytical solution. Once confident in the FEM approach, the thermal analysis for the rest of the test matrix was performed in *ANSYS*. Small differences in the results indicate that the chosen grid is sufficient for the design work performed here and should provide a good basis for the comparison with future experimental work.

6. Skin Friction Gage Designs

Chapter 6 presents a detailed description of the skin friction gages used in this research. This description includes the material selection process, design considerations, as well as insight into the functionality and purpose of each component. The chapter then explains gage construction, assembly, and static calibration in detail. Lastly, the chapter follows the development of the first skin friction gage and evolutionary changes that made the second skin friction gage successful.

6.1. Design Overview

Through this research, two separate gages, PT-1 and PT-2, were designed and fabricated. A schematic overview of the design for both gages was shown previously in Figure 16. They are similar in design, but vary slightly in material and geometry. Each gage is compact in size with overall dimensions of 44.5 mm (1.75 in) tall by 19.1 mm (0.75 in) in diameter. Both gages consist of four primary components: the sensing head, cantilever flexure, housing, and collar. The components and variation in both gage designs are discussed at length below.

6.1.1. Sensing Head

The sensing head is made of a 303 stainless steel (303 SS). Several additional materials such as brass, copper, and aluminum were also explored and analyzed in the FEM suite $ANSYS$. Stainless steel was chosen primarily for its low thermal conductivity which slows the rate of heat transfer throughout the gage. It is also a common material for models in the arc-heat facilities at $AEDC$. The 303 grade was chosen for its availability and ease of machinability. Secondary justifications for 303 SS include: high temperature resistance, ease of soldering for the bellows

attachments, and similarity of material to the flexure. An assembly illustration of the sensing head, flexure, and bellows can be seen in Figure 52.

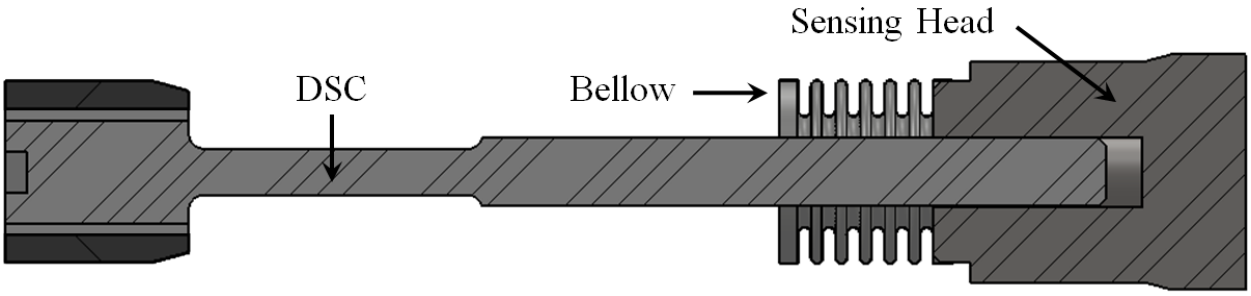

Figure 52: Assembly of the Sensing Head, *DSC* Flexure, and Bellows

The sensing head diameter for all gages was 8.12 mm (0.32 in), thus the $A_{head} = 51.9$ mm^2 (0.08 in^2). This size was chosen to meet the compact design goals of the gage and in conjunction with the flexure constraints to meet the design shear levels. The head is 10.8 mm (0.425 in) in depth with a slight taper in diameter approximately 2.5 mm (0.1 in) down from the top. This adds some additional clearance to the gap size while maintaining a similar thermal profile to the surrounding wall. The base of the head is dimensioned to sit and solder the FC-4-L bellows in place. A central well with a depth of 7.24 mm (0.285 in) and 2-56 UNC threading fastens the head to the flexure.

6.1.2. Flexure

The central beam of the DSC-6 summarized in Section 3.3.3: *Strain Gage and Selection* serves as the flexure for all skin friction gages in this study. The flexure is made of a 17-4 precipitation hardening (PH) corrosion-resistant steel ($CRES$). Built for high-strength, the steel is annealed and heat treated to H900 conditions. Dimensioned within $\pm$0.00254 mm (0.001 in) tolerance, it has a shaft length of 38.1 mm (1.5 in) and a shaft diameter of 2.36 mm (0.093 in). The flexure is set into a 6.35 mm (0.25 in) long by 6.35 mm (0.25 in) diameter base for press-fit

mounting applications. An assembly and part drawing of the DSC-6 is found Appendix A: Drawings.

6.1.3. Housing

The housing component encapsulates the DSC. Throughout the different gage iterations, the number of components and materials has changed. PT-1 is composed of a two-piece housing while the PT-2 housing consists of only one piece. Both 303 SS and brass versions were constructed for thermal analysis. The DSC is set into the base of the housing by a light press-fit and secured with EPO-TEK 353ND epoxy [74]. EPO-TEK 353ND is a low outgassing, high-temperature ($T_{max} = 625\ K$) epoxy designed for metallic application. During curing, the epoxy wicked around the DSC press-fit and protruding wires. The sensing head is screwed carefully onto the DSC, while the bellows are attached to the housing by solder or epoxy.

The inner cavity of the housing is 6.35 mm (0.25 in) in diameter and is designed as small as the DSC allows. Its overall dimensions are 28.7 mm (1.13 in) in length with an outer diameter of 12.7 mm (0.5 in). The LeePlug hole is located in the throat area of the housing, approximately 25.4 mm (1.0 in) up from the base.

6.1.4. Collar

The collar served as the joining component between the flat plate test model and the gage. It is constructed of 303 SS for the same reasons as the sensing head. The outer diameter of the collar was manufactured in tight tolerance for a light press-fit into the plate. The collar compresses an O-ring between the plate and is secured down by six bolts in a radial pattern. Pointed setscrews were used to adjust and hold the assembled friction gage in place. A small gap ($\sim$0.10 mm) exists along the circumference between the collar and housing components. The

sensing head, collar, and flat plate are all aligned as a flush surface. An assembly illustration of the friction gage, collar, and flat plate can be seen in Figure 53.

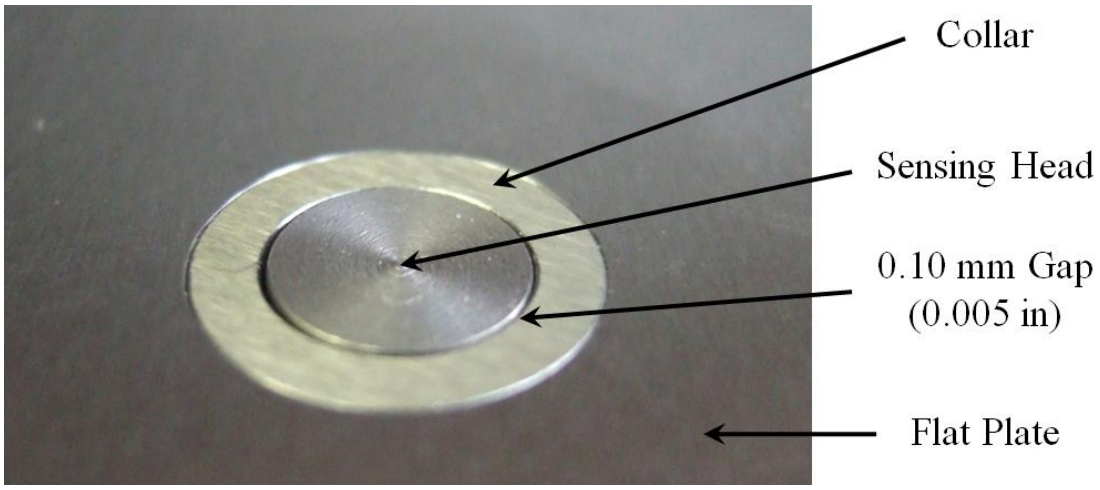

Figure 53: Assemble of the Friction Gage, Collar, and Flat Plate

6.2. Gage One: *PT*-1

The first skin friction gage, *PT*-1, was designed to incorporate many ideas and concepts such as the *DSC* unit, bellows, and LeePlug oil fill system. The test series identified the behavior and accuracy of its design, while laying a basis of wall shear stress measurements under different flow conditions in which to compare to the analytical predictions.

6.2.1. PT-1 Gage Design

The uniqueness of the *PT*-1 design compared to the Sang et al gage [18] is its two-piece housing which simplifies the assembly process of the gage. The bellows is secured to the top housing and sensing head by a silver solder application as described in Chapter 3.5: *Bellows*. The top housing assembly is shown in Figure 54.

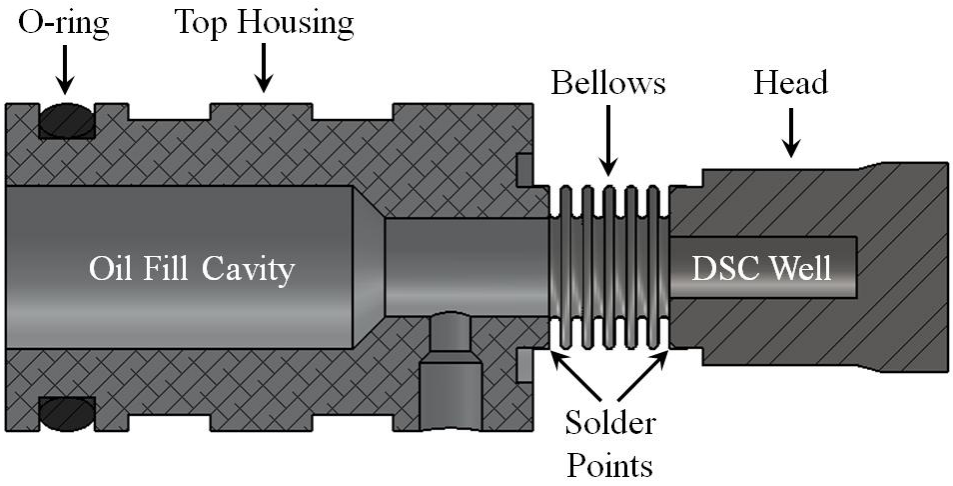

Figure 54: *PT*-1, Top Housing Assembly

Meanwhile, the DSC is press-fit into the base housing and secured with a high-temperature epoxy. The base housing assembly is shown in Figure 55. The assembly of the gage is done by carefully turning the base housing assembly into the top housing assembly until the DSC is fully threaded into the head. The assemblies are sealed with an O-ring and secured together with point setscrews.

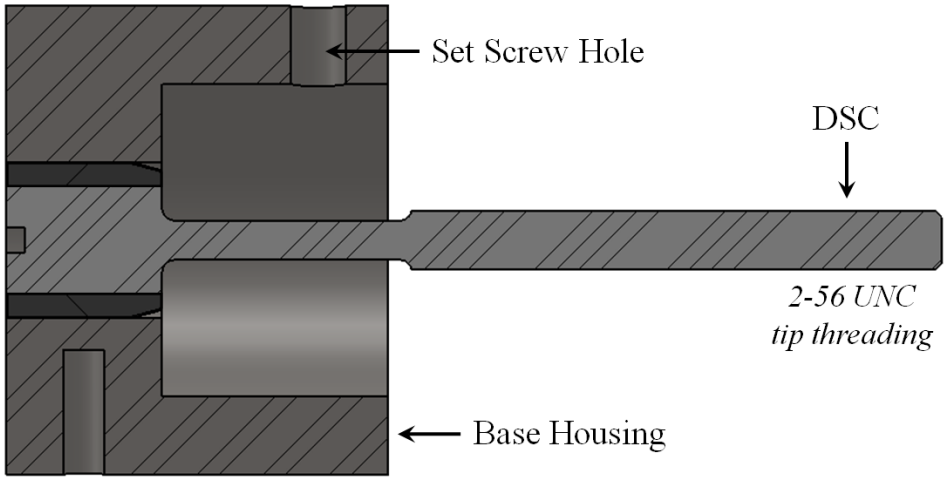

Figure 55: *PT*-1, Base Housing Assembly

Two builds were constructed under the PT-1 configuration. The distinction between them is in the application of parts. Build 1 was assembled per the initial design specifications, while Build 2 lacked the bellows and oil filling.

The two-piece housing turned out to be more problematic than beneficial. The slightest misalignment of components or error in machining tolerances proved to be devastating to the functionality of the gage. Due to the extreme sensitivity of the DSC unit, any pre-loading would dominate the shear stress measurements. This issue was revealed while observing the output signal when assembling the housing components. The DSC was being pre-loaded based upon the orientation of the housing components and any compression or tension in the bellows system. Despite many thorough attempts to resolve this issue, no final solution could be found.

Another serious problem arose once the gage was fully assembled. The vacuum chamber test revealed trapped air inside the oil. Even after repeating the oil filling process several times, this issue continued to occur. Two theories were developed as to why air may have been consistently getting trapped. The most likely is that air pocket originated from the top of the DSC around the threading in sensing head cavity or from between the two housing pieces near the O-ring. The spaces may have been too tight for air to be extracted during the oil pump down. Another theory is that the epoxy or oil fill may have been outgassing within the interior cavity. These problems associated with Build 1 had to be resolved before PT-1 could be tested in the wind tunnel.

Build 2 was assembled without oil filling or a LeePlug inserted, thus leaving the inner cavity of the housing open. This setup eliminates all possibility of an adverse pressure differential inside the gage created by trapped air bubbles in the oil. As the ambient pressure of the test section drops during a run, the empty LeePlug hole allows the pressure inside the gage to

equalize with the test chamber. Additionally, the bellows was completely removed under the suspicion that it was preloading the DSC. Under this stripped down configuration, all potential adverse loads were eliminated. However, as a consequence, the strain sensor was no longer protected and the gage was undamped. Though the modifications of Build 2 are far from the initial design intentions, they were necessary compromises over the Build 1 configuration and would serve adequately enough in the Virginia Tech HST. Figure 56 shows the fully assembled PT-1, Build 2 gage.

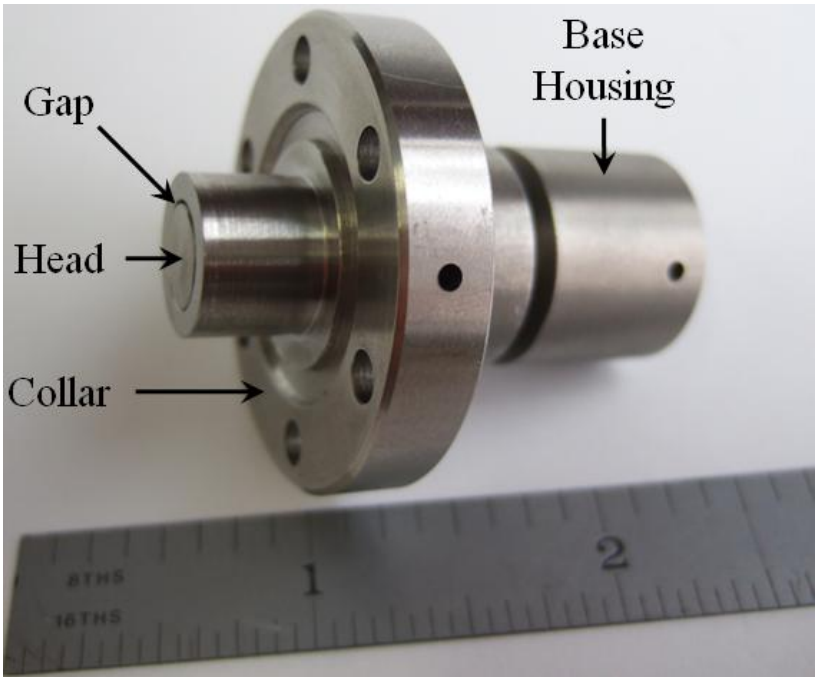

Figure 56: *PT*-1 Build 2

6.2.2. PT-1 Calibration Results

The calibration curve for PT-1, Build 2 is found in Figure 57. Numerous point load measurements were taken in both the positive and negative directions of each axis. Though the calibration curve was highly linear, the spread of data is greater than anticipated and desired. During small deflections, such as those experienced during calibration, no hysteresis effects were

detected. However, if the gage was loaded too quickly or too heavily (shear stress equivalent, $\tau_w > 1{,}000\ Pa$), hysteresis was evident. This effect is concerning as it could potentially occur during test runs under high vibration loading.

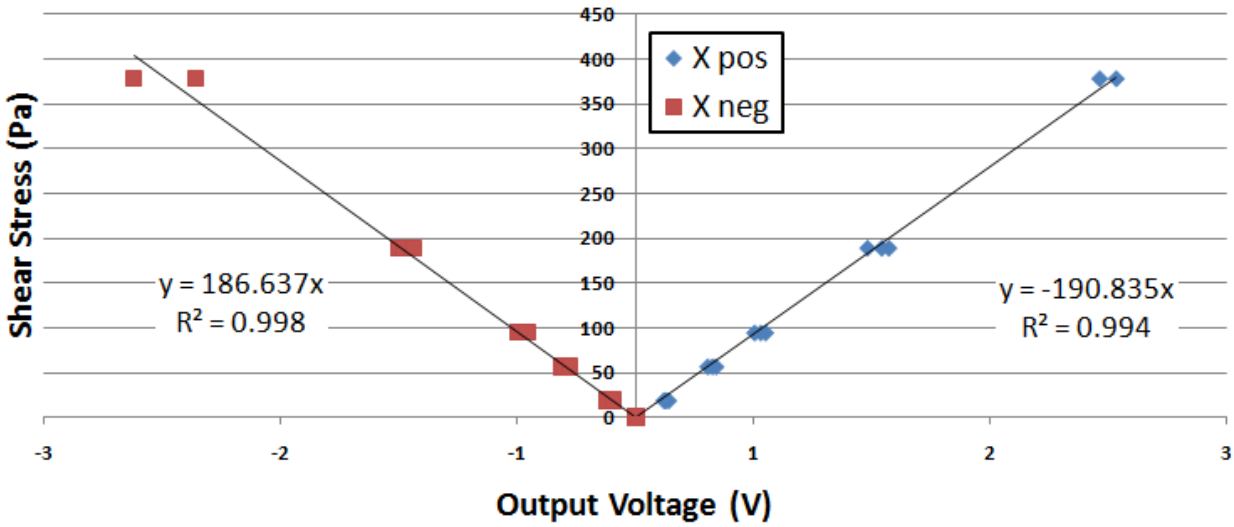

Figure 57: *PT*-1 Build 2 - Calibration Curve

PT-1, Build 2 was disassembled and assembled quite a bit while working to resolve its issues. During this handling, one of strain sensors on the *DSC* was broken, rendering that axis useless. With no secondary axis, the misalignment correction could not be applied thus adding to the uncertainty of the measurement.

6.2.3. Concluding Remarks Concerning the Gage Design of PT-1

The *HST* test results from the *PT*-1 Test series to be described later were disappointing. Skin friction measurements were obtained but not in direct concurrence with the analytical predictions. Repeatability was not achieved. The initial gage design and functionality was compromised due to several unforeseen problems. Though much effort was put into making this gage work, several key factors prevented its success, including, but not limited to, those depicted in Figure 58.

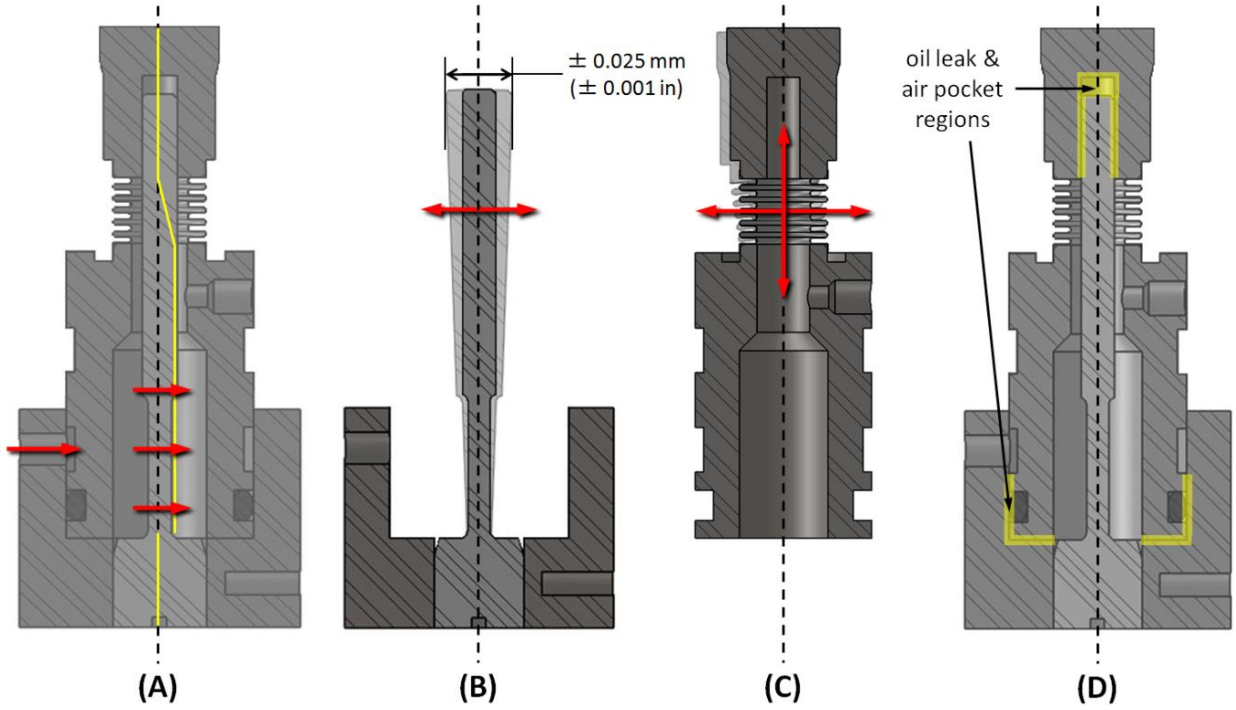

Figure 58: Potential Error Sources for *PT*-1

The two part housing was built to permit soldering of the bellows to simplify the assembly process but clearly instead complicated the gage design. As was evident, the slightest adverse force is enough to pre-load the gage. Joining the two housing components created a potential misalignment as the set screws imposed an adverse sideways force (Figure 58A). The DSC was mounted with the highest tolerance, but it was not perfectly perpendicular to the base as was required (Figure 58B). By connecting the head to the housing prior to assembly, the head was aligned with the bellows, but not within the DSC (Figure 58C). Finally, the two-part housing added a potential leak point for the oil to escape and a cavity for air pockets to form. Such a cavity is also present in the sensing head cavity and around the DSC threading (Figure 58D). Many of these problems could not be immediately fixed without a gage re-design. These design flaws were addressed in the second iteration of the gage.

No thermal analysis was conducted on PT-1. Since the gage configuration was modified so heavily in Build 2, it was hard to isolate any thermal effects. Once the immediate problems specified above were corrected for, heat measurements and thermal error could be addressed.

6.3. Gage Two: PT-2

The second skin friction gage, PT-2, was designed to improve upon the concepts of the first gage. It was the first gage to successfully incorporate the bellows and oil fill system as well as thermal management system. PT-2 was also intended to be the first skin friction gage capable of operating in the $AEDC$ test facilities.

6.3.1. PT-2 Gage Design

PT-2 is an improvement of design robustness. The biggest change was the housing alteration, which now consisted of only a single piece, see Figure 59. Both 303 SS and brass versions were constructed. The 303 SS was chosen for the same justifications as the rest of the gage components, while the brass housing was chosen for better thermal management. The assembly process is similar to that of PT-1. The sensing head still screws onto the DSC in the same manner. This time however, a ceramic epoxy was used to fill the inside of the sensing head cavity and along the threads of the DSC. Also, instead of pre-soldering the bellows to the housing, it was attached after the assembly with a high-temperature epoxy. This allowed the DSC alignment to direct the position of the sensing head instead of it being pulled to one side by a pre-soldered bellows.

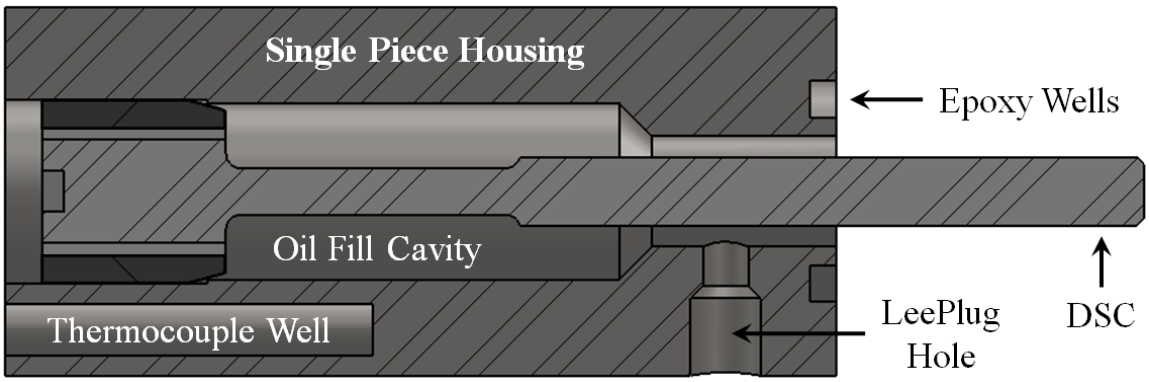

Figure 59: *PT*-2 Sing Piece Housing Assembly

The new housing assembly functioned as intended. All PT-2 gages were assembled without pre-loading the DSC unit. An added benefit to the redesign is the overall reduction in size of the gage. The new base is one third smaller with a diameter of just 12.7 mm (0.5 in). The DSC wiring out of the bottom of the base now turns 90° which also shrinks the operational dimensions of the gage. All this is especially important as PT-2 was designed to fit in the tight compartment of the test wedge cavity at $AEDC$.

The collar component was also altered. A standard epoxy was applied to set screw holes and gap surrounding the housing. This was done in order to prevent any flow through the small gap around the head and top area of the gage. Such circulation could potentially heat the gage more quickly, create a larger pressure differential around the sensing head, or load the DSC. Set screws were originally used to hold the gage in place, but the epoxy replaced them to secure the gage to the collar during the wind tunnel testing. Figure 60 illustrates the different areas and purpose of the epoxy application on PT-2.

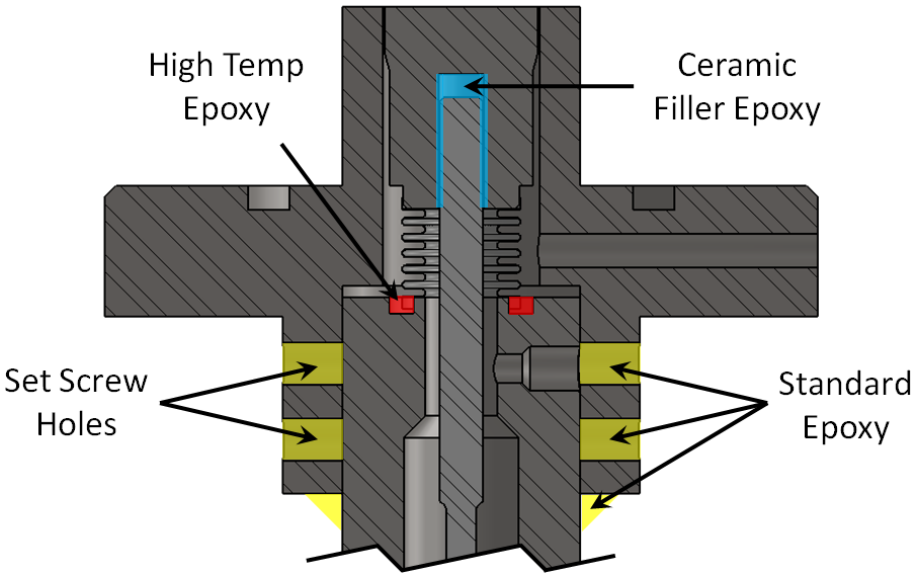

Figure 60: Epoxy Application on *PT*-2

Four different builds were manufactured under the *PT*-2 design. Build 1 was configured the same as *PT*-1, Build 2, without oil filling or a LeePlug inserted, leaving the inner cavity of the housing open. This was done to see how the new *PT*-2 features fared under the same test conditions as the earlier gage. Build 2 was identical to Build 1, but it was oil filled and sealed. Build 3 was also oil filled, but it had an active cooling system and brass housing. Since the thermal conductivity for brass is much higher than that of stainless steel, the active cooling could better control the temperature of the housing and thus any thermal effects imposed on the *DSC* unit. The copper cooling tubes were soldered on prior to inserting the *DSC* to avoid any unnecessary damage. Unfortunately, the brass build was never tested due to a dysfunctional *DSC* unit. The last configuration, Build 4, is the Build 2 model modified with the addition of an active cooling system. Since Build 2 was already assembled, metallic epoxy had to be used rather than solder to secure the copper cooling tubes. Photographs of the completed builds are seen in Figures 61 and 62.

Figure 61: *PT*-2, Build 2 (left), Build 3 with brass housing and soldered cooling tubes (right)

Figure 62: *PT*-2, Build 4 with cooling tubes attached with metalized epoxy

6.3.2. PT-2 Calibration Results

Numerous point load measurements were taken in both the positive and negative directions of each axis. The curve fit for all *PT*-2 build iterations proved to be highly linear. Compared to the *PT*-1 results, the calibration points had far less drift and showed no signs of hysteresis even at high levels of imposed stress. Only Build 4 incorporated the temperature calibration curve correction, as it was the only Build capable of regulating the housing temperature. The calibration curve for *PT*-2 Build 4 at $T_{DSC} = 294\ K$ (530 $°R$) in the positive axis can be found in Figure 63.

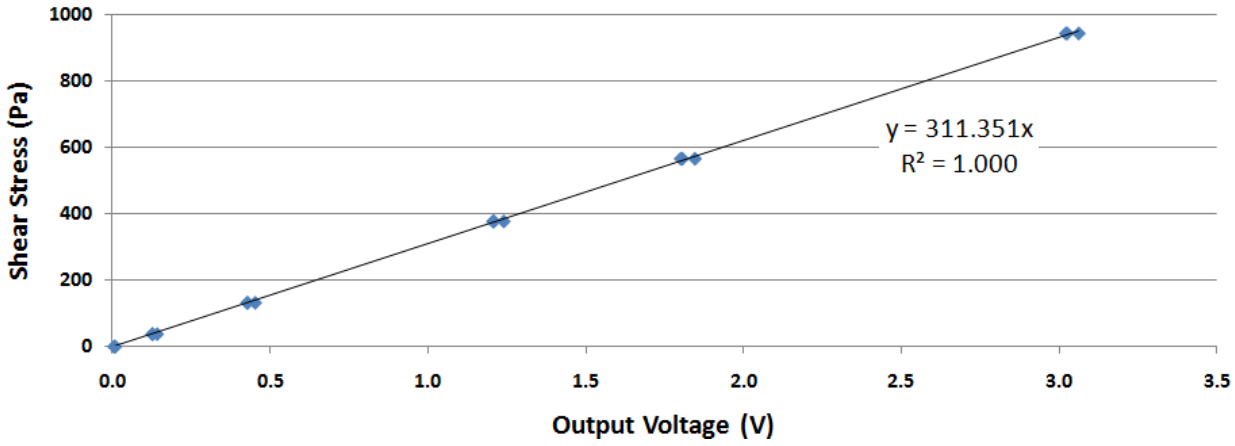

Figure 63: *PT*-2 Build 4 - Calibration Curve

One strain sensor broke in Builds 2 and 4, rendering each with only one working axis. In the case of Build 3, both axes broke, and the gage was unusable. Every one of the gages were assembled and handled with great care yet still the strain sensors were breaking. This is can be accredited to the fragile nature of the DSC unit and or lack of robustness in the design of the gage.

7. Virginia Tech Hypersonic Tunnel Testing

Chapter 7 presents the experimental results from the Virginia Tech Hypersonic Tunnel. The chapter thoroughly analyzes the performance of each skin friction gage and presents in chronological order. The first gage proves the general design concepts and implementation of the strain gage unit. The second gage successfully integrates and implements the bellows, oil filling, and thermal management system.

7.1. *PT*-1 Gage Results

Gage verification of *PT*-1, Build 2 was performed in the Virginia Tech Hypersonic Tunnel. Tests were conducted at various flow conditions corresponding to different air stagnation temperatures: $T_{0,2} = 276$, 412, 530, and 655 K. The gage was tested four to six times at each flow condition to verify its operability and repeatability of results.

A total of 18 seconds worth of data is recorded during each run cycle to include the time before the tunnel is engaged, the blow down, and after the tunnel shutdowns. The HST runs for approximately three seconds from the 5.5 to 8.5 second interval in the recorded data. The total plenum pressure of the wind tunnel is drawn into the test plots to indicate the duration of run.

Figure 64 illustrates an ideal shear stress test case under cold flow conditions. The DSC measurement prior to, during, and after a run should hold fairly constant with minimal signal noise. The DSC output begins balanced and should recover balanced after each run. High levels of vibration are expected during the violent startup and shut down periods of the tunnel and can be seen in the dynamic response of the system.

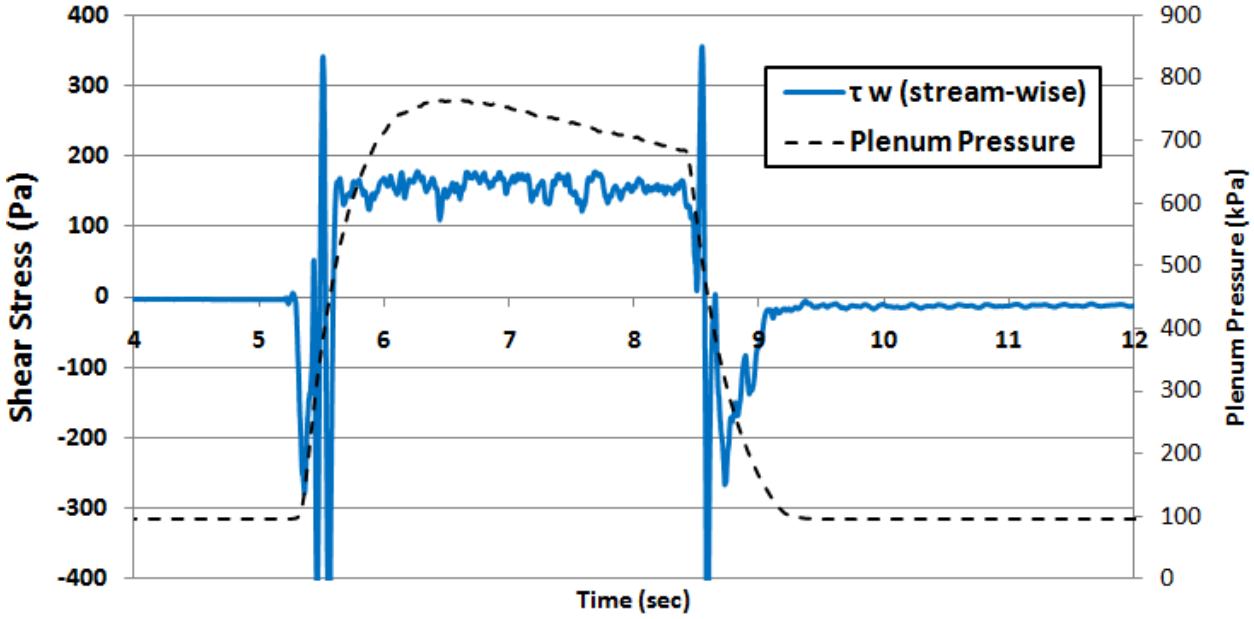

Figure 64: *PT*-1, Build 2 - Ideal Test Run

Unfortunately, very few of the runs under the *PT*-1, Build 2 test series were ideal cases. The *DSC* did not always recover to a balanced value immediately after the run. For approximately 10 minutes following the tunnel shutdown, the *DSC* showed signs of creep and hysteresis as the output signal wandered randomly before holding constant at a new value offset from the original balanced one. A typical test run is shown in Figure 65.

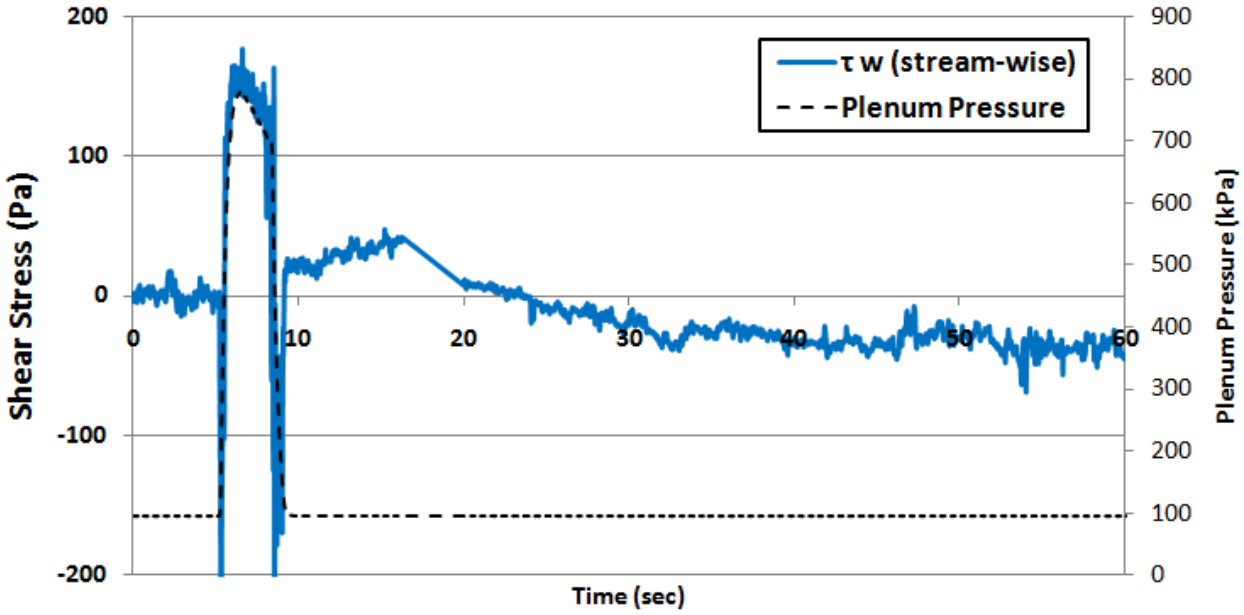

Figure 65: *PT*-1, Build 2 - Typical Test Run

The shear stress measurement was deduced from the average value over a one second time period in the run cycle once the initial tunnel startup vibrations subsided. Any offset in the pre-run value was subtracted from the measured shear stress value. This method assumes that the gage is not being pre-loaded, and the DSC is properly balanced. A summary of the entire *PT*-1, Build 2 test series is shown in Figure 66 overlaying the analytical predictions originally plotted in Figure 49.

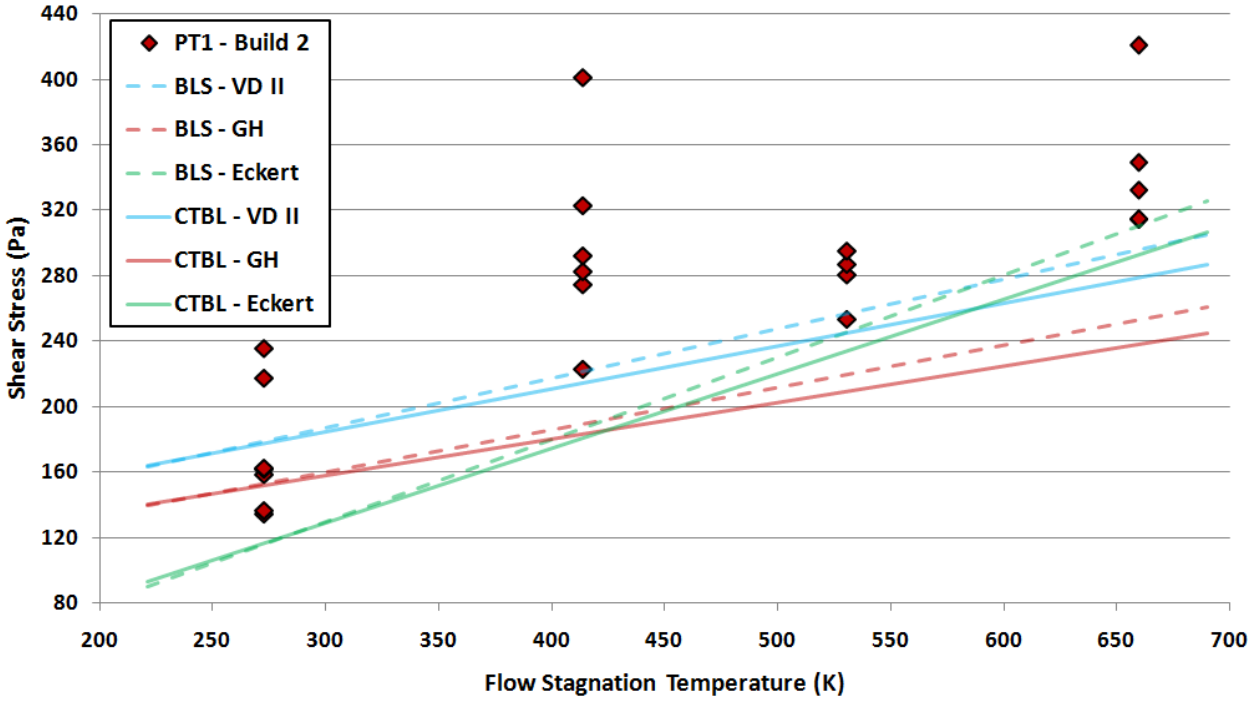

Figure 66: *PT*-1, Build 2 - *HST* Test Summary

As seen in Figure 66, the shear stress data points are not repeatable and show a spread error of up to 80% difference. No error bands could be determined due to the immense scatter of points. The overall trend is somewhat distinguishable and is also in fair agreement with the predicted values. The data point trend appears to be increasing with flow temperature. It is on the same order of magnitude but slightly higher than that of the analytical predictions.

7.2. *PT*-2 Gage Test Results

Gage verification tests of all *PT*-2 Builds were performed in the Virginia Tech Hypersonic Tunnel. Runs were conducted at more flow conditions than used previously for Gage *PT*-1. Each run corresponded to different flow stagnation temperatures ranging from $T_{0,2} = 275$ to 655 K (495 to 1,180 °R) at increments of approximately 60 K (180 °R). The gages were tested between two and six times at each flow condition to verify operability and repeatability of results. The following section discusses the test results from Builds 1, 2, and 4.

7.2.1. PT-2, Build 1

Build 1 was the only gage tested that had a fully functional DSC unit. As a result, the shear stress could be measured both parallel and perpendicular to the direction of the flow. Therefore, if the gage is aligned properly, the perpendicular axis should be unchanged while the parallel axis would indicate the full shear stress value experienced in the 2D flow of the tunnel. Slight variations in the data can be expected due to tunnel vibrations and the dynamic response of the system. The alignment of Build 1 was initially verified by the unheated flow test runs as shown Figure 67.

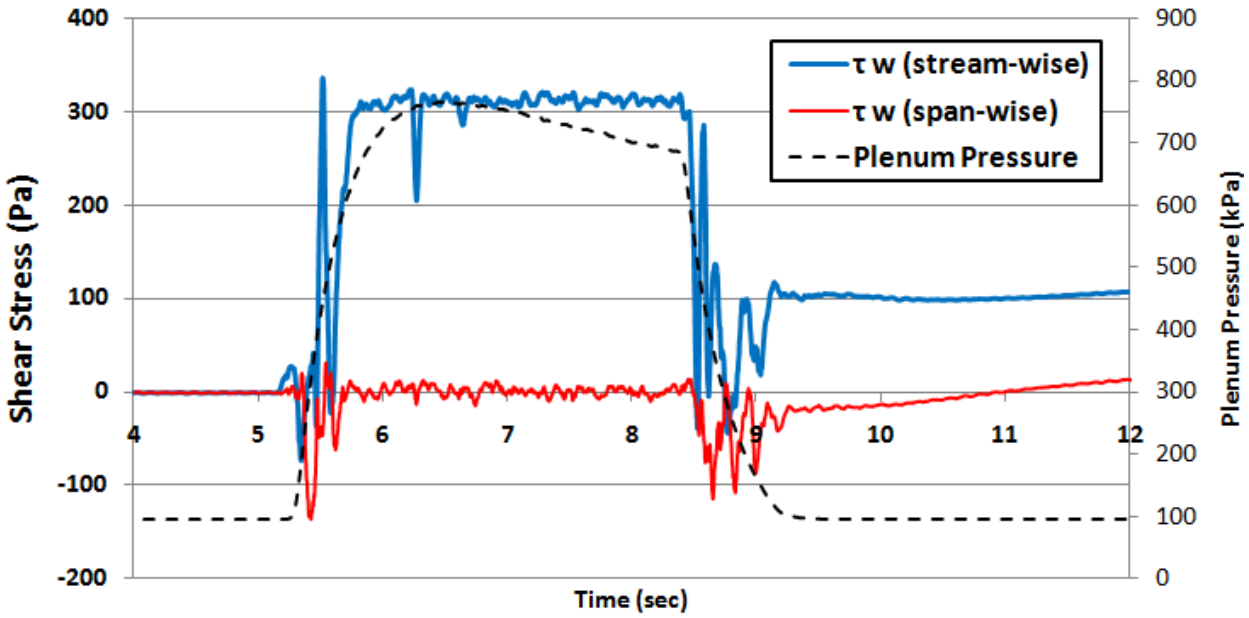

Figure 67: *PT*-2, Build 1 at $T_{0,2} = 275\ K$

As the gage was tested at higher flow temperatures, errors in the system became more pronounced. Figure 68 shows the results for a wind tunnel run at $T_{0,2} = 530\ K$ (954 $°R$).

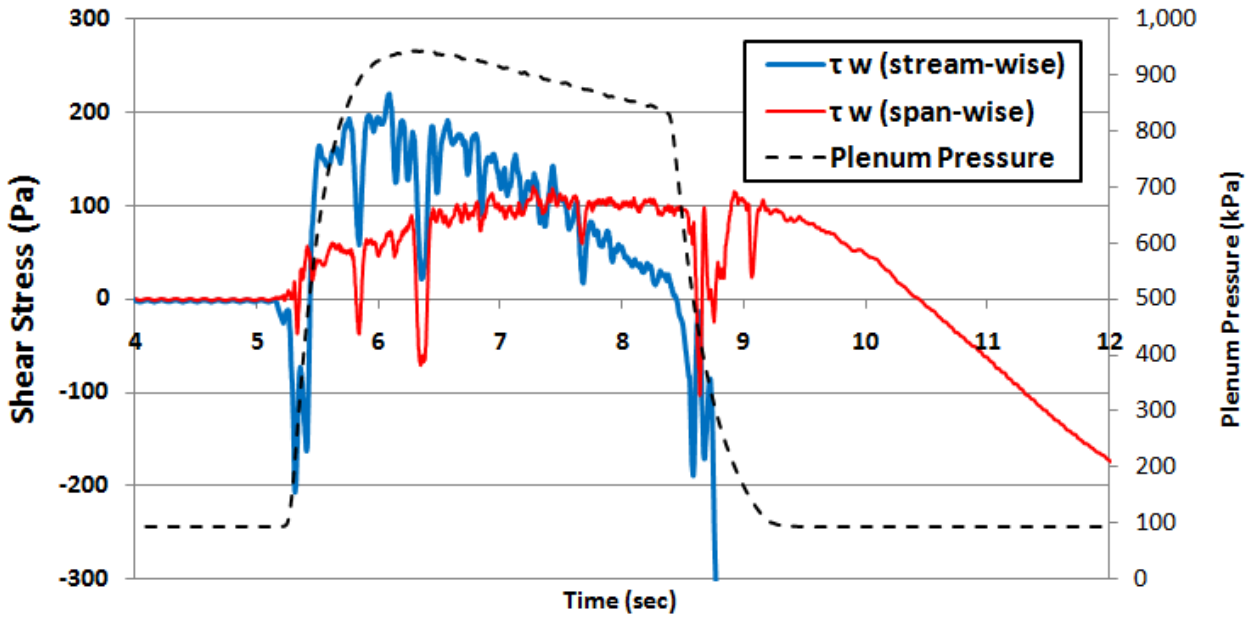

Figure 68: *PT*-2, Build 1 at $T_{0,2} = 530\ K$

The trends displayed in Figure 68 are repeatable but irregular and get progressively worse as the flow temperature increases. Many problems can be identified in the data of these test runs. First, the perpendicular axis no longer remains balanced and exceeds a shear stress reading higher than that of the stream-wise axis. Second, both axes drift significantly during the run. They are still affected by the plenum pressure but other influences are very evident. Third, the signal noise is no longer minimal as the measurements reach a variance as high as 40%. Lastly, the DSC output signal no longer recovers to its balanced position at the end of the run. During the unheated flow runs, the signal can be seen to recover in less than 10 seconds, whereas in heated air runs such as those in Figure 68, the offset was much larger and never recovered at all.

Though no intricate thermal analysis was done on Build 1, it is presumed with great confidence that the errors present in the test runs correlate primarily to temperature effects, with additional error possibly due to a lack of system damping. Compared to the PT-1 test results, PT-2, Build 1 experienced greater levels of error under identical test conditions and setup. There

are many possible sources for these results. First, the thinner walled housing may have had different insulating characteristics thus effecting thermal error. Second, the sealed collar may have adversely influenced the flow in some unpredictable way. Lastly, the DSC unit may have been damaged in some manner.

Build 1 proved that the PT-2 design resolved the pre-loading problems experienced under the PT-1 design. Though this was a significant step, thermal and vibration errors were still needed to be controlled. Build 2 would be the first gage to address both these areas.

7.2.2. PT-2, Build 2

In Build 2, the gage was filled with oil and plugged. With no internal cavities to trap air and by utilizing a more powerful vacuum system, the filling process was a success. The result from the unheated flow run is seen in Figure 69.

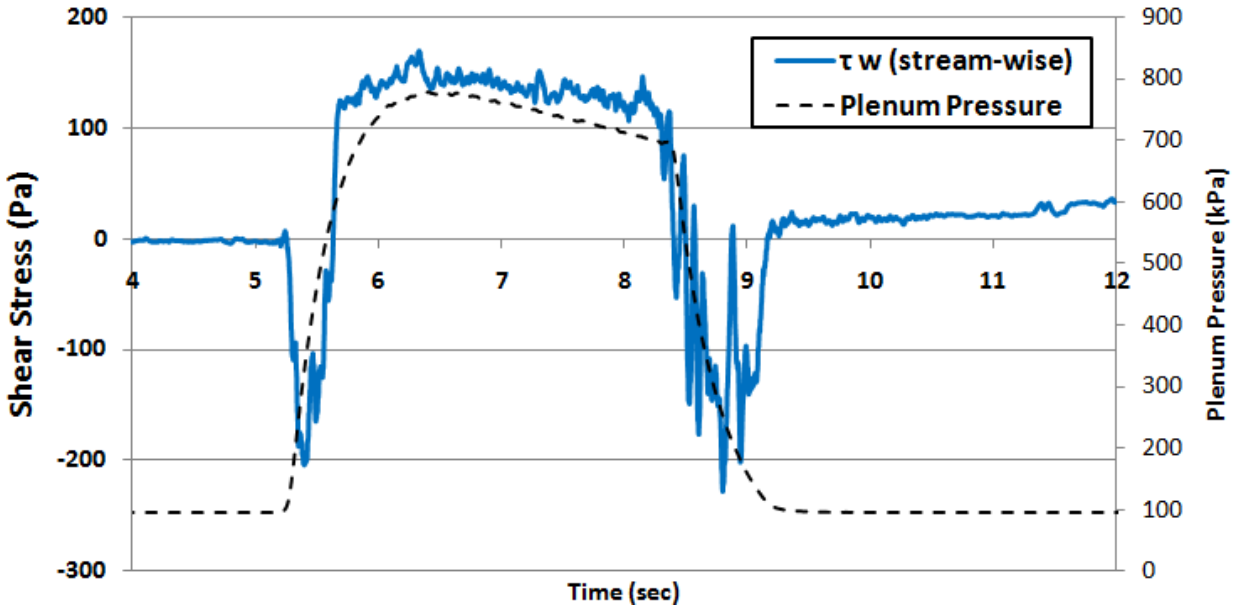

Figure 69: PT-2, Build 2 at $T_{0,2} = 275\ K$

Compared to the corresponding Build 1 unheated flow run (Figure 67), Figure 69 demonstrates an improvement in the dynamic response of the system. The signal noise is

reduced to a variance of 8.8% error versus the previous 11% error at cold flow conditions. More impressive is the damped vibrations that occur during the tunnel startup and shut down periods. The amplitude of the output signal is greatly suppressed, and the oscillations are almost eliminated. Other factors may influence vibrations in the signal such as temperature. However, these damping trends are consistent throughout the Build 2 test series even during the hot flow runs, thus the thermal influence on vibrations must be minimal. It is concluded that oil filling does in fact have a significant damping effect on the gage, thus reducing the uncertainty in the measurements.

Despite the addition of the oil filling in Build 2 at high flow temperatures, thermal error is still present in the system. This influence is clearly seen Figure 70 for a test run where $T_{0,2} = 655\ K$ (1,180 $°R$).

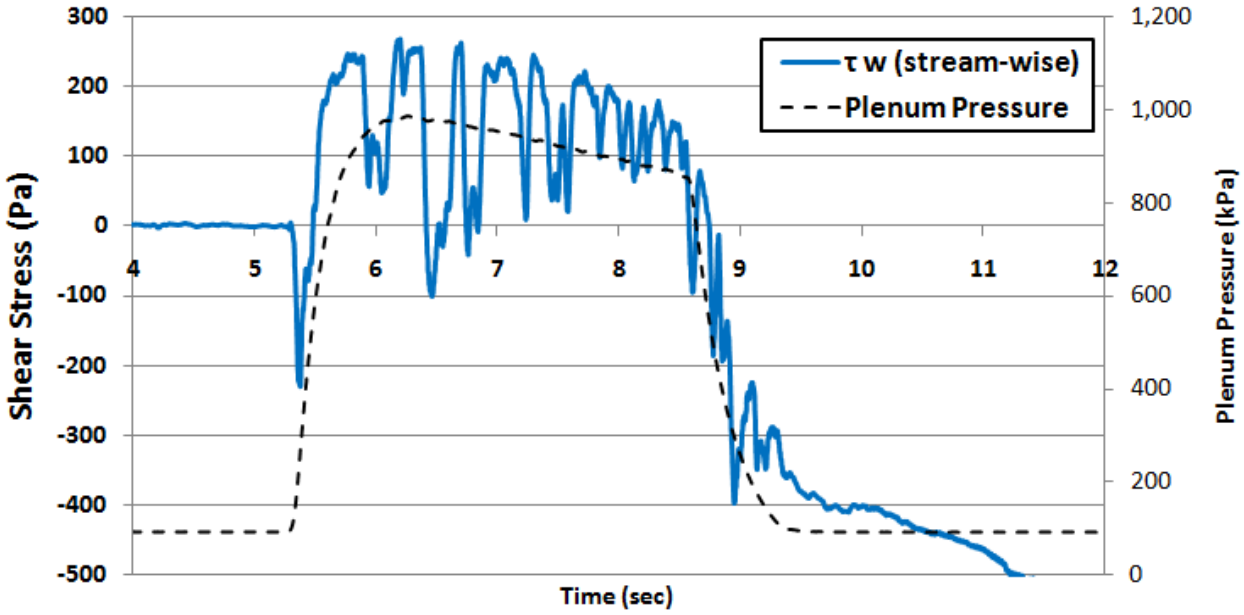

Figure 70: *PT*-2, Build 2 at $T_{0,2} = 655\ K$

Figure 70 shows a great deal of variance in the data reaching levels of 41%. In addition, the gage no longer recovers to the balanced position as before. Even after 10 minutes following

the run, creep and hysteresis are still present in the output signal. A summary of the entire PT-2 Build 2 test series is shown in Figure 71 alongside the analytical predictions. The estimated uncertainty error bands have been overlaid as well, marking the upper and lower data points.

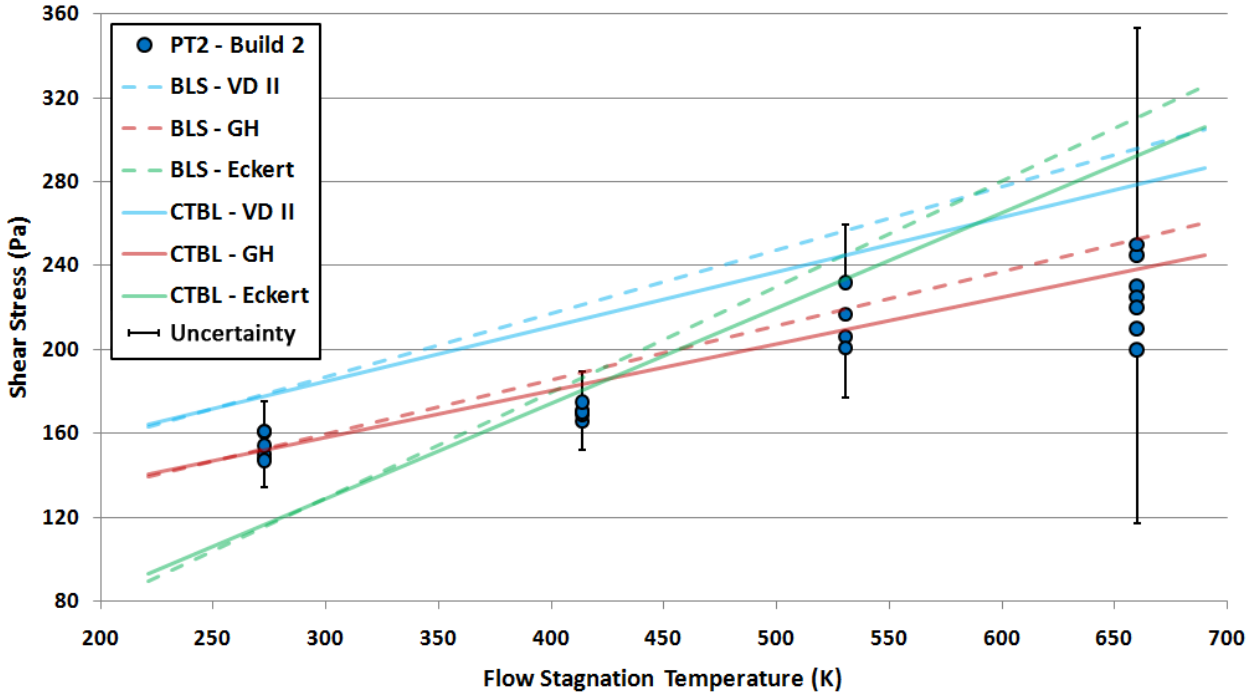

Figure 71: *PT*-2, Build 2 *HST* Test Summary

It can be seen that as the flow temperature increases, so too does the uncertainty of the data. Even in the unheated flow runs there is going to be some error influencing the gage, and for Build 2, the uncertainty is greater than desired. The DSC is extremely sensitive to temperature change, thus analyzing the temperature around the strain sensor region is essential to better understanding the gage. The thermocouple readings around the gage strain sensors (Figure 39) at different flow conditions are seen in Figure 72.

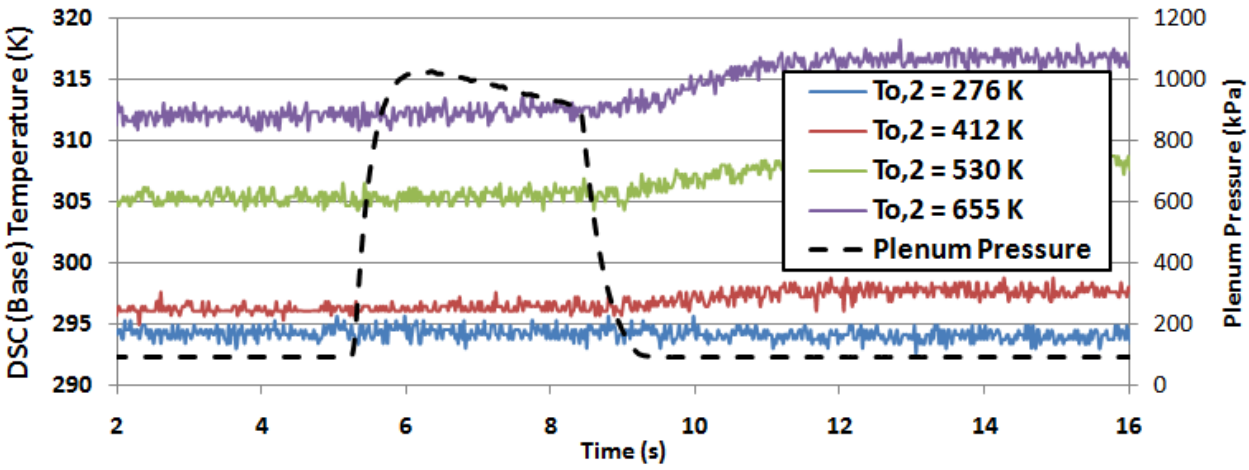

Figure 72: *PT*-2, Build 2 - *DSC* (Base) Temperature

At $T_{0,2} = 655\ K$ (1,180 $°R$), the base temperature is 18 K above the calibration temperature of 294 K (530 $°R$). Since Build 2 does not incorporate the temperature correction calibration, it is susceptible to the thermal stability errors. The DSC-6 has a $\pm$ 0.01 $\%/K$ (0.03 $\%/°R$) null stability rating at full deflection. Though the manufacturer's rating is a theoretical maximum, at $T_{0,2} = 655\ K$ (1,180 $°R$) this correlates to approximately 180% error.

Oil filling proved to damp the gage and reduce signal noise. It may also have reduced heat flux throughout the gage, but thermal stability was not adequate. It can be safely concluded that the design is still dominated by thermal error. In order to regulate the gage temperature, an active cooling system was devised and implemented.

7.2.3. PT-2, Build 4

Build 4 was the first gage to be calibrated for temperature correction and utilize an active water-cooling system. Six coils of copper tubing were wrapped around the base of the housing. Even at a water flow rate of only $1.84\times10^{-6}\ m^3/s$ (1.75 gph), this thermal management system was capable of cooling the entire gage in a matter of seconds. The resulting effect on the shear stress measurements turned out to be very impressive.

Even at the highest temperature flow conditions, the strain sensor region is untouched by thermal fluctuation. Figure 73 illustrates the effect that active cooling had on the base thermocouple as compared to the Build 2 data from Figure 72.

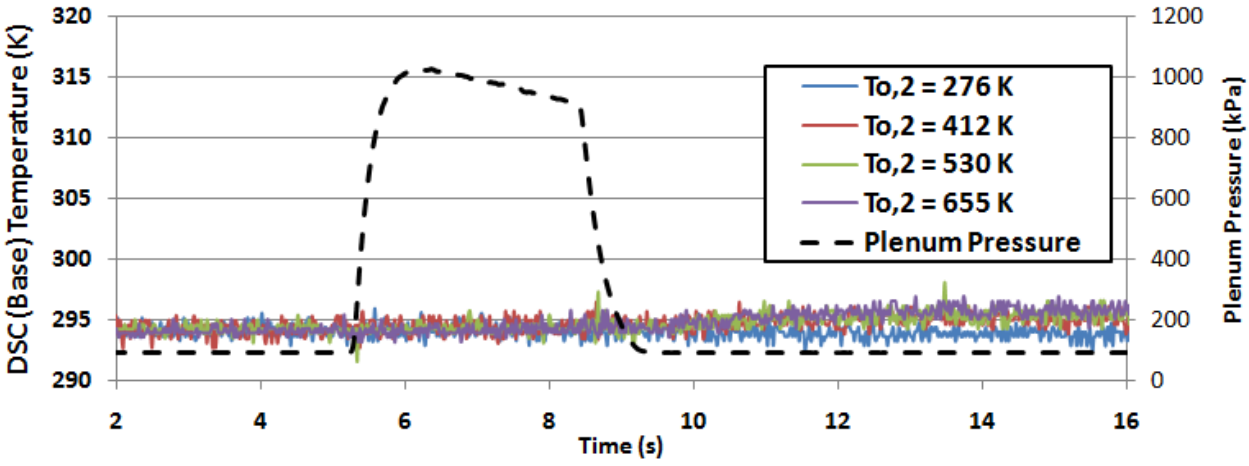

Figure 73: *PT*-2, Build 4 - *DSC* (Base) Temperature

At all flow temperatures, the thermal error in the system was eliminated or greatly reduced. This is evident in the $T_{0,2} = 655\ K$ (1,180 $°R$) test run as seen in Figure 74 where error would be the most prevalent.

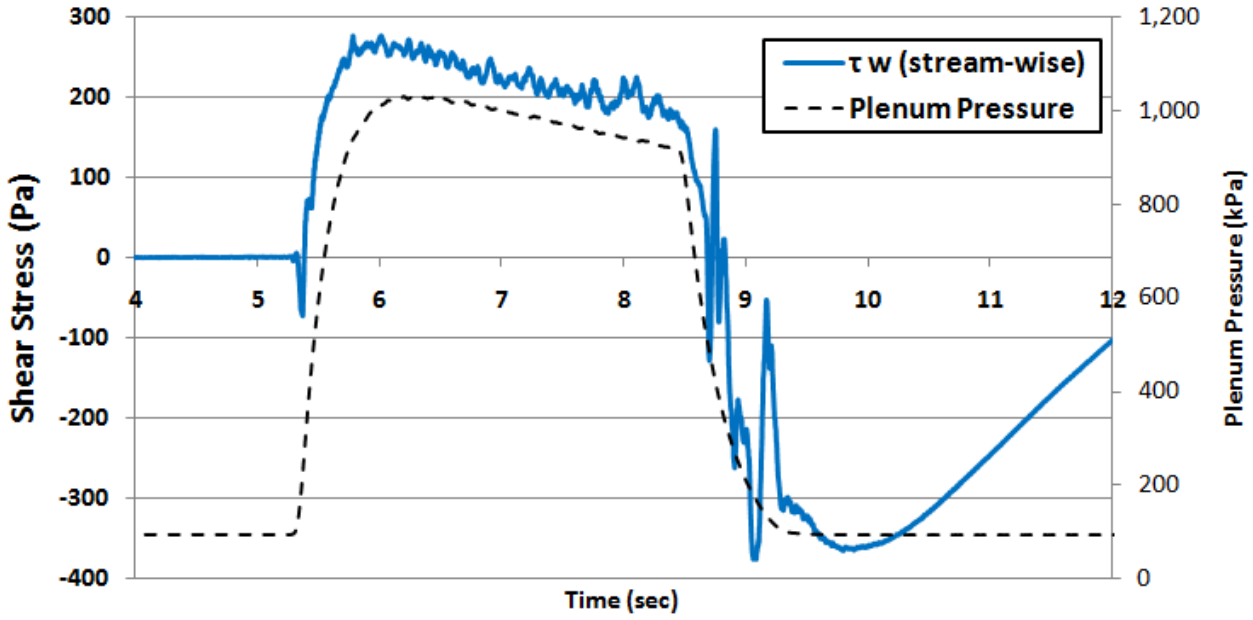

Figure 74: *PT*-2, Build 4 at $T_{0,2} = 655\ K$

Compared to the equivalent Build 2 test run (Figure 70), Figure 74 demonstrates many improvements. The system still shows signs of damping due to the oil filling. The data variance is within a reasonable range of error and can be easily be determined. Lastly, the output signal recovers within a matter of seconds. A summary of the entire *PT*-2, Build 4 test series is shown in Figure 75. The analytical predictions and estimated uncertainty error bands are once again overlaid.

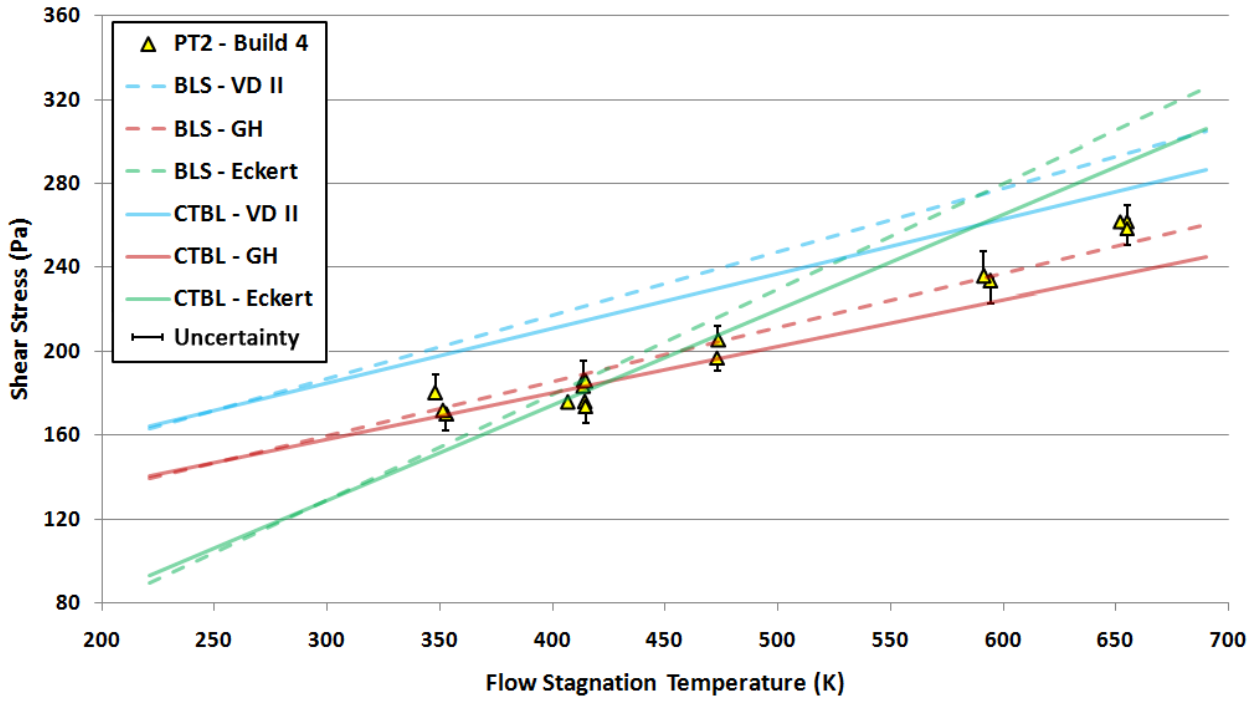

Figure 75: *PT*-2, Build 4 *HST* Test Summary

Build 4 exhibited excellent performance and was the best configuration tested in this research study. The experimental data demonstrated very good concurrence with the predicted values and good repeatability was achieved.

8. Analysis of Errors and Uncertainty

Chapter 8 analyzes the uncertainty for the skin friction gages. It explores three categories of measurement errors: calibration, data acquisition, and data reduction. This approach follows the uncertainty methodology outlined by Figliola and Beasley [75]. The chapter introduces a variety of error sources and presents a summary of uncertainty conclusions.

8.1. Calibration

The calibration of the skin friction gage produced an error source based on angular misalignment. The Deflection Sensor Cartridge unit has two, bi-directional axes offset by 90° with regions of sensitivity associated with each strain gage as shown in Figure 25. The ideal orientation to calibrate the gage is in the direction of one of these axes. In this manner, the aligned strain gage would be subject to the full load of the hanging point mass while the other would remain ideally unaffected by any strain. To quantify error due to angular misalignment, the gage was mounted horizontally and small axial rotations were introduced. It was discovered that for rotations of 5° or less, which was the maximum misalignment expect during calibration and testing, the error was within $\pm$ 0.4%.

Another potential error source during calibration stems from thermal drift. The temperature of the room and DSC unit were monitored during the calibration process. Full calibration cycles were conducted in less than a minute and it was found that the environmental temperatures remained relatively stable. No measurable effects were detected.

The gage was calibrated three to six times in each of the two strain gage axes. Results proved to be highly linear and repeatable. The error in the calibration curves was analyzed as twice the standard deviation of the maximum difference in the output from the same input mass.

For a Gaussian distribution of samples, 95% of the data points fall within $\pm 2\sigma$ of the mean. The highest percent error achieved in this statistical analysis was $\pm$ 0.3%

8.2. Data Acquisition

The errors sources associated with the measurements of the experimental data are referred to as data acquisition errors. The first of these was due to misalignment effects as previously explored in Chapter 3.2.1. Allen [41] relates ratios of geometric parameters and boundary layer thickness to measurement uncertainties. During the wind tunnel verifications, the boundary layer thickness for all flow conditions was found to be $\delta = 4.0\ mm$ (0.157 in). The skin friction gages of this study had a gape size of approximately $G = 0.127\ mm$ (0.005 in), a head diameter of $D = 8.128\ mm$ (0.32 in), and a lip size of $C = 2.54\ mm$ (0.1 in). Both of the gages had a gap ratio G/D of 0.0156, and lip ratio C/D of 0.3125 respectively. According to Allen, when the misalignment was zero, the effect of the gap size became negligible. It was also found that a small lip size in conjunction with a larger gap produced very little error. An estimate error of the gage output due to lip geometry was $\pm$ 1.0%. Each gage was designed with a lip and gap ratio in a range that was relatively insensitive to these misalignment effects.

Non-nulling designs are commonly susceptible to protrusion effect which occurs due to the tilt of the sensing head when the flexure beam deflects. When the head tilts, it inevitably will enter the flow and disrupting the pressure gradient. Allen claimed that protrusion effects became an issue when the head protruded more than 50.8 μm (0.002 in) beyond the surface. Using the relationship found in Section 3.4: *Head Deflection*, the sensing head was estimated to deflect only 3.05 μm (0.00012 in) under the most extreme flow conditions at $AEDC$. Fortunately, due to these very small deflections the effective error was not an issue in this study and the protrusion effect were considered negligible.

The zero drift contribution associated with strain gage unit was also a concern in the uncertainty analysis. The gage output was monitored over a 60 second period, which was several times longer than the duration of a *HST* test run. The voltage change from the balanced zero level was found to be fairly small. The associated error was $\pm$ 0.5% of the expected strain gage signal.

Thermal and vibration effects were the primary sources of error encountered during testing. It is hard to isolate the contributions associated with each source individually, however they can be quantified together. Thermal forms of errors stem from semi-conductor strain gage sensitivity, voltage drift, mismatch of thermal expansion rates, and non-uniform "soak" temperature as previously discussed in Chapter 3.2.2: *Thermal Effects*. Errors associated with vibration levels can be seen during the test cycles in the dynamic response of the system. When the skin friction gages were tested without damping or thermal management systems, they experienced noise levels on the same order of magnitude as that of the deflection being measured. Attempts to average and filter this data produce large levels of uncertainty in the output. This can be seen in the experimental results of the gages *PT*-1 Build 2 and *PT*-2 Build 1, whose output signals were distorted by as much as $\pm$ 80% error. Hence, a great level of error control was needed as was the purpose of certain design features in later iterations of the gage. *PT*-2, Build 4, included a bellows system, oil filling, active-water cooling, and incorporated a temperature compensating calibration that ultimately reduced uncertainties to $\pm$ 4.2%.

8.3. Data Reduction

The final source of error comes from the data reduction process. These errors are associated with the curve fits such as those used in the instrumentation calibrations, Rayleigh-Pitot formula, and Talyor-Maccoll polynomial, etc. Data averaging and truncation will also

affect the overall skin friction measurement of the gage. The calibration curves of the gage proved to be highly linear, and data reduction was performed with an adequate amount of significant digits. The uncertainty due to the data reduction was kept to a minimal and was estimated to be no greater than $\pm$0.5%.

8.4. Summary of Uncertainty Analysis

Determining the errors associated with direct measuring skin friction gages was difficult. Uncertainty values were computed using the root of the sum of the squares method. Refer to Appendix B for the equation sets used in this study.

As the error sources in the skin friction gages were identified, controlled, and minimized throughout the different design iterations, the measurement uncertainties dramatically decreased. Table 5 summarizes the evolution of the wall shear stress uncertainly values for all functioning builds of the *PT*-2 design. Error was reduced from as high as $\pm$ 80% to just under $\pm$ 5.0%.

Table 5: *PT*-2 Shear Stress Uncertainties

	Percent Uncertainty (%)		
T_{heater} (℃)	Build 1	Build 2	Build 4
20	11	8.8	---
100	---	---	**4.7**
200	18	8.3	**4.8**
300	---	---	**3.2**
400	38	12	---
500	---	---	**4.8**
600	80	41	**3.0**

The uncertainty in the measurements due to the calibration and data reduction has been shown to be small (less than $\pm$ 0.5% respectively). The largest source of uncertainty is in the data acquisition as a results of induced thermal and vibration effects, which are believed to be as high as $\pm$ 4.2%. A summary of the uncertainty analysis can be found in Table 6.

Table 6: Measurement Uncertainties in the Virginia Tech Hypersonic Tunnel

Type of Uncertainty		Level of Uncertainty
Calibration		
	Angular Misalignment	$\pm$ 0.4 %
	Curve Linearity	$\pm$ 0.3 %
	Thermal Drift	*Negligible*
Data Acquisition		
	Gap ratio, Lip Ratio	$\pm$ 1.0 %
	Protrusion	*Negligible*
	Zero Drift	$\pm$ 0.5 %
	Vibration /Thermal Effects	$\pm$ 4.2 %
Data Reduction		
	Truncation, curve fits	$\pm$ 0.5 %
Overall Skin Friction Uncertainty		$\pm$ 5.0 %

In the Virginia Tech *HST* wind tunnel, the estimated overall error for the final skin friction gage design, *PT*-2, Build 4, was $\pm$ 5.0 %. These values are superimposed over the stream-wise C_f values summarized in Figure 76 of the conclusion chapter. The errors encountered in flows without thermal and/or vibration effects, such as the *HST* cold flow tests, will be much less.

9. Conclusion and Recommendations

Chapter 9 presents the conclusions and recommendations of this study. The contributions of this study will be summarized. It also discusses how well the goals and objectives of this research were met. Lastly, it provides suggestions and recommendations for future work with direct skin friction gages in high-enthalpy flow.

9.1. Conclusion

The goal to design, build, and analyze a skin friction gage capable of operating in high-enthalpy flow conditions was successful. Two different gage types were constructed and tested in the Virginia Tech Hypersonic tunnel. The gage design incorporated a unique bellows system as a shroud to contain the oil filling and protect the strain gages. Oil filling provided dynamic and thermal damping while eliminating uniform pressure loading. An active water-cooling system provided thermal management to control temperature gradient, while two Wheatstone full-bridge configurations in conjunction with a temperature compensation calibration minimized temperature effects. The design concepts proved to be very sound and give good results in heated, supersonic flow. Through finite element model analyses, the gages are predicted to perform favorably in the Arc-Heated Facilities at Arnold Engineering Development Center for short durations tests. No gage has been constructed or tested at $AEDC$ to date.

The first gage design (PT-1) utilized a two-piece housing to permit soldering of the bellows in order to simplify the assembly process. However, this arrangement proved more problematic than beneficial. The gage was found to be susceptible to preloading due to trapped air bubbles in the oil and component misalignment (PT-1, Build 1). To resolve these problems, any source of error was eliminated by removing the bellows and oil filling (PT-1, Build 2). Still,

the experimental data was not repeatable and show a spread error of up to 80% difference. From this gage, it was concluded that a much more robust design was needed.

The second gage design, PT-2, resolved the preloading errors experienced by PT-1. A one-piece housing reduced the complexity of the gage and number of potential misalignment sources. In addition, high-temperature epoxy was used instead of soldering to set the gage components in a natural steady state where they would be unaffected by any preloading. To isolate error sources, several PT-2 gage iterations were constructed and put through rigorous test matrixes. PT-2, Build 1 was constructed without oil filling or a bellows to see how the new PT-2 features fared under the same test configuration as the earlier PT-1 gage. PT-2, Build 2 was oil filled and equipped with a bellows to identify damping effects. Lastly, the PT-2, Build 4 configuration was identical to Build 2 but with the addition of a thermal management system.

The results from the PT-2 test series were very informative. All prior gage iterations leading up to PT-2, Build 4 laid the fundamental groundwork necessary for its success. The oil filling and bellows provided adequate damping, while the active water-cooling system and temperature correction calibration significantly reduced thermal error. PT-2, Build 4 demonstrated very good concurrences with the predicted values and good repeatability was achieved.

Once the gage functionality was refined and the uncertainty errors were reduced, the skin friction coefficient (C_f) could be accurately determined. This was accomplished by normalizing the measured wall shear stress by the local dynamic pressure. Figure 76 summarizes the stream-wise C_f values in the Virginia Tech HST under various flow conditions.

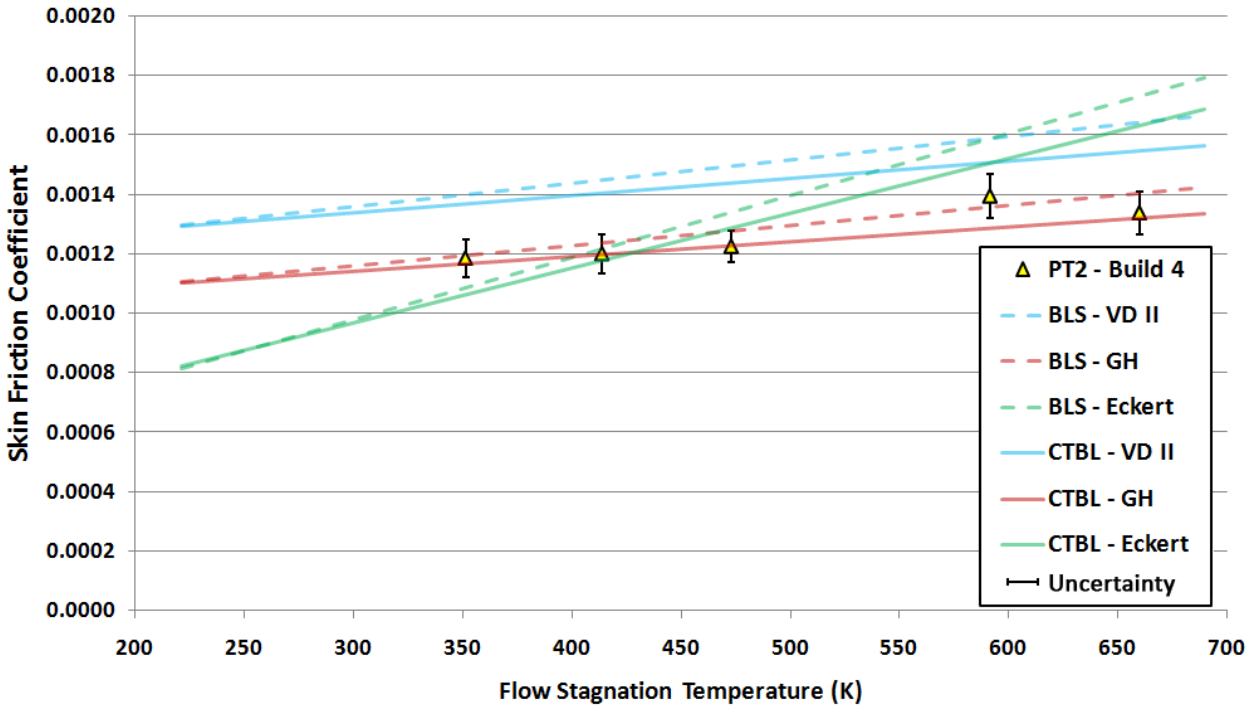

Figure 76: *HST* Skin Friction Measurements

The PT-2, Build 4 gage measured C_f values ranging between 0.00118 and 0.00134 with a $\pm$ 5% uncertainty. These values are well within the predicted C_f range expected in the Virginia Tech HST under such flow conditions. The C_f values closely followed the Gersten-Herwig model and were about 15 – 30% lower than the Van Driest II model. The Eckert trend line was not followed, but the skin friction values fell within a $\pm$30% band.

9.2. Recommendations for Future Work

First and foremost, the implementation of the gage design concept is still not robust enough for routine use. Thus, a detailed design refinement and verification is still required before testing can be conducted at $AEDC$. To help accomplish this, instrumentation design experts at $AEDC$ (or perhaps $NASA$) should be consulted with to acquire expert advice on potential design improvements and better manufacturing processes.

The incorporation of a bellows system proved to be a very successful method of containing the oil filling while preventing oil leakage. However, it required a delicate assembly process and was a source for preloading in the initial gage designs. To enhance robustness, in place of the bellows a narrow, tortuous path, flow channel could be substituted. This strategy is common in steam turbines and is commonly known as a labyrinth seal. The oil filling could be just as effective, may still not leak out, and might remove the need for bellows all together. Careful study of this nascent idea would be needed.

One of the major drawbacks of a High-Enthalpy Ablation Test Unit is the large amounts of electromagnetic interference (EMI) the arc emits. The current gage designs do not account for any EMI sources aside from the low-pass Butterworth filter. This can be controlled by using electrical shielding, cut-off frequency filters, or by containing the gage in a protective platform.

Considering the gages used in this study, effects due to thermal gradient or inertia can be greatly reduced but cannot be completely eliminate. Research using fiber-optic technology might provide a suitable alternative to the cantilever beam arrangement and strain gages. Fiber-optics removes the need for a physical measurement device and could potentially eliminate all thermal and inertial error sources.

Lastly, although the PT-1 and PT-2 designs are considered small in size compared to the average cantilever beam, skin friction gage, they may still be too large for any application at $AEDC$. The test platforms at $AEDC$ have very small cavities in which to house measurement devices. Future gages will need to be reduced in size in order to make them more manageable for such applications. In order to do so, a cut down DSC unit or new flexure will have to be implemented.

References

[1] Sang, A. K., *Study of Rubber Damped Skin Friction Gages for Transonic Flight Testing*, Dissertation in Partial Fulfillment for the Degree of Master of Science in Aerospace Engineering, Virginia Polytechnic and State University, Blacksburg, VA, February, 2001.

[2] *Webster's Dictionary*. Drag. Riverside Publishing Company, 1991.

[3] Houghton, E. L., and P. W. Carpenter, *Aerodynamics for Engineering Students*. Oxford: Butterworth-Heinemann, 2003.

[4] Anderson, John D. Jr., *Introduction to Flight, 3rd Edition*. McGraw-Hill, Inc., New York, 1989, p. 6.

[5] Anderson, John D. Jr., *Fundamentals of Aerodynamics, 2nd Edition.* McGraw-Hill, Inc., New York, 1991., p. 16.

[6] Kuethe, A.M., and Chow, C., *Foundations of Aerodynamics: Bases of Aerodynamic Design Fourth Edition*. John Wiley & Sons, Inc., New York, NY, Chapter 14 & 18, pp. 314-315, 399, 1996.

[7] Schetz, J.A., *Direct Measurements of Skin Friction in Complex Flows*, Applied Mechanical Review, vol. 50, no. 11, Pt. 2, 1997.

[8] MacLean, M., *A Numerical Study of Internal Flow Effects on Skin Friction Gages*. Dissertation in Partial Fulfillment for the Degree of Doctor of Philosophy, Virginia Polytechnic Institute and State University, Blacksburg, VA, April, 2002.

[9] Chadwick, K.M., *An Actively Cooled Floating Element Skin Friction Balance for Direct Measurement in High Enthalpy Supersonic Flows*, Dissertation in Partial Fulfillment for the Degree of Doctor of Philosophy, Virginia Polytechnic Institute and State University, Blacksburg, VA, December, 1992.

[10] DeTurris, D.J., *A Technique for Direct Measurement of Skin Friction in Supersonic Combustion Flow*, Dissertation in Partial Fulfillment for the Degree of Doctor of Philosophy, Virginia Polytechnic Institute and State University, Blacksburg, VA, November, 1992.

[11] Novean, M., *Direct Measurement of Skin Friction in Complex Supersonic Flows*, Dissertation in Partial Fulfillment for the Degree of Doctor of Philosophy, Virginia Polytechnic and State University, Blacksburg, VA, March, 1996.

[12] Remington, A., *A Study of Non-Fluid Damped Skin Friction Measurements for Transonic Flight*, Dissertation in Partial Fulfillment for the Degree of Master of Science in Aerospace Engineering, Virginia Polytechnic and State University, Blacksburg, VA, July, 1999.

[13] Magill, S. A., *Study of a Direct Measuring Skin Friction Gage with Rubber Compounds for Damping*, Dissertation in Partial Fulfillment for the Degree of Master of Science in Aerospace Engineering, Virginia Polytechnic and State University, Blacksburg, VA, July, 1999.

[14] Pulliam, W. J., *Development of Fiber Optic Aerodynamic Sensors for High Reynolds Number Supersonic Flows*, Dissertation in Partial Fulfillment for the Degree of Doctor of Philosophy, Virginia Polytechnic Institute and State University, Blacksburg, VA, November, 2000.

[15] Orr, M. W., *Design, Analysis, and Initial Testing of a Fiber-Optic Shear Gage for 3D, High-Temperature Flows*, Dissertation in Partial Fulfillment for the Degree of Doctor of Philosophy, Virginia Polytechnic Institute and State University, Blacksburg, VA, November, 2004.

[16] Smith, T. B., *Development and Ground Testing of Direct Measuring Skin Friction Gages for High Enthalpy Supersonic Flight Tests*, Dissertation in Partial Fulfillment for the Degree of Doctor of Philosophy, Virginia Polytechnic and State University, Blacksburg, VA, September, 2001.

[17] Rolling, A. J., *Design of Gages for Direct Skin Friction Measurements in Complex Turbulent Flows with Shock Impingement Compensation*, Dissertation in Partial Fulfillment for the Degree of Doctor of Philosophy, Virginia Polytechnic and State University, Blacksburg, VA, July, 2007.

[18] Sang, A. K., Rolling, A. J. and Schetz, J. A., *A Novel Skin Friction Sensor for Hypersonic Flow*, AIAA 2006-3837, 2006.

[19] Schetz, J. A., *Direct Measurement of Skin Friction in Complex Flows (Invited)*, AIAA 2010-0044, 2010.

[20] Smith, R. K., Wagner, D. A., Cunningham, J., *A Survey of Current and Future Plasma Arc-Heated Test Facilities for Aerospace and Commercial Applications*, AIAA 98-0146, 1998.

[21] Smith, D. M., Whittingham, K. B., *Flow Calibration of the AEDC H2 Mach 3.4 Arc-Jet Nozzle*, AIAA 2006-8105, 2006.

[22] Arnold Engineering Development Center. *High-Enthalpy Arc-Heated Facilities at AEDC*. Arnold AFB, TN: Office of Public Affairs, AEDC/DOS, 2000

[23] ANSYS, Inc. *ANSYS*. Computer software. Version 12.

[24] Heiser, W. H., Pratt, D. T., *Hypersonic Airbreathing Propulsion*. American Institute of Aeronautics and Astronautics, Inc., Washington, DC, 1994 p. 487.

[25] Froude, W., *Experiments on the Surface-friction Experienced by a Plane Moving through Water*, 42nd British Association Report, vol. 42, pp. 118-125, 1872.

[26] Winter, K. G., *An Outline of the Techniques Available for the Measurement of Skin Friction in Turbulent Boundary Layers*. Progress in Aerospace Sci., vol. 18, pp.1-57, 1977.

[27] Schetz, J. A., *Overview of Movable Element Skin Friction Gages*. Retrieved February 14, 2001, from the World Wide Web: http://www.aoe.vt.edu/~jschetz/Skin_Friction/Cf_Gage_Table&Refs.pdf

[28] Pulliam, W. J., *Development of Fiber Optic Aerodynamic Sensors for High Reynolds Number Supersonic Flows*, Dissertation in Partial Fulfillment for the Degree of Doctor of Philosophy, Virginia Polytechnic Institute and State University, Blacksburg, VA, November, 2000.

[29] Nitsche, W., Haberland, C. and Thunker, R., "Comparative Investigations of the Friction Drag Measuring Techniques in Experimental Aerodynamics," ICAS 84-2.4.1, 14th ICAS Congress, 1984.

[30] Dhawan, S., *Direct Measurements of Skin Friction*, NACA Report 1121, 1953.

[31] Schetz, J.A., *Boundary Layer Analysis*, Prentice Hall, Englewood Cliffs, NJ, 1993.

[32] Tanner, L.H., Blows, L. G., *A Study of the Motion of Oil Films on Surfaces in Air Flow, with Application to the Measurement of Skin Friction*, Journal of Physics E: Scientific Instruments, Vol. 9, pp. 194-202, Mar. 1976

[33] Kim, K., Settles, G., *Skin Friction Measurements by Laser Interferometry in Swept Shock Wave/Turbulent Boundary-Layer Interactions*, AIAA 88-0497, 26th Aerospace Sciences Meeting, Reno, NV, Jan. 1988

[34] Klein, E., Margozzi, A., *Exploratory Investigation on the Measurement of Skin Friction by Means of Liquid Crystals*, 11th Israel Annual Conf. On Aviation and Astronautics, Tel Aviv, Mar. 1969

[35] Reda, D.C. and Wilder, M.C., *Shear-Sensitive Liquid Crystal Coating Method Applied Through Transparent Test Surfaces,* AIAA Journal, Vol. 39, No. 1, 2001, pp. 195-197

[36] Gaudet, L., Gell, T. G., *Use of Liquid Crystals for Qualitative and Quantitative 2-D Studies of Transition and Skin Friction*, ICIASF '89 – 13th International Congress on Instrumentation in Aerospace Simulation Facilities, vol. 43, pp. 66-81, 1989.

[37] Schetz, J.A., *Skin Friction Measurements in Complex Turbulent Flows using Direct Methods*, pp. 421-430, Engineering Turbulence Modelling and Experiments 6, W. Rodi (Edit.), , Elsevier Ltd., 2005.

[38] Mehregany, M., DeAnna, R., Reshotko, E., *Microelectromechanical Systems for Aerodynamics Applications,* AIAA Paper 96-0421, Jan. 1996

[39] Orr, M. W., *Design, Analysis, and Initial Testing of a Fiber-Optic Shear Gage for 3D, High-Temperature Flows*, Dissertation in Partial Fulfillment for the Degree of Doctor of Philosophy, Virginia Polytechnic Institute and State University, Blacksburg, VA, November, 2004.

[40] Rolling, A. J., Schetz, J. A., *Direct Skin Friction Measurements with Shock-Impingement Compensation in Complex Turbulent Flows*, AIAA 2006-3828, 2006.

[41] Allen, J. M., *Improved Sensing Element for Skin-Friction Balance Measurements*, AIAA J., vol. 18, no. 11, pp.1342-1345, 1980.

[42] Coles, D., *Measurements in the Boundary Layer on a Smooth Flat Plate in Supersonic Flow*, JPL Report 20-70, 1953.

[43] O'Donnell, F.B., *A study of Effect of Floating Element Misalignment on Skin Friction Accuracy*, University of Texas *DRL*-515, 1964.

[44] Brown, K.C. and Joubert, P.N., *Measurement of Skin Friction in Turbulent Boundary Layers with Adverse Pressure Gradients*, J. Fluid Mechanics, vol. 35, pt. 4, pp. 737-757, 1967

[45] Fowke, J.G., *Development of a Skin Friction Balance to Investigate Sources of Error in Direct Skin Friction Measurements*, NASA TM X 61905, N69-40-054, 1969.

[46] Frei, D. and Thomann, H., *Direct measurements of skin friction in a turbulent boundary layer with a strong adverse pressure gradient*, J. Fluid Mech., vol. 101, pp. 79-95, 1980.

[47] O'Donnell, F.B. and Westkaempfer, J.C., *Measurement of Errors Caused by Misalignment of Floating-Element Skin-Friction Balances*, AIAA J., vol. 3, no. 1, pp. 163-165, 1965.

[48] Allen, J. M., *Systematic Study of Error Sources in Supersonic Skin-Friction Balance Measurements*, NASA TN D-8291, 1976.

[49] MacLean, M. and Schetz, J.A., *Numerical Study of Detailed Flow Affecting a Direct Measuring Skin-Friction Gauge*, AIAA J., vol. 41, no. 7, pp. 1271-1281, 2003.

[50] Watson, R.D., Hall, R.M., and Anders, J.B., *Review of skin friction measurements including recent high-Reynolds number results from NASA Langley NTF*, AIAA-2000-2392, 2000.

[51] Online Materials Information Resource. Retrieved March 14, 2009, from the World Wide Web: http://matweb.com

[52] Kistler-Morse. *Displacement Sensor (DS-6) Inspection and Operation Instructions*. Spartanburg, SC, 2005.

[53] Servometer. *Miniature Metal Bellows and Electroforms*. Cedar Grove, NJ, 2008.

[54] Westkaempfer, J.C, *Step-Temperature Effects on Direct Measurements of Drag*, AIAA J., vol. 1, no. 7, pp. 1708-1710, 1963.

[55] Voisinet, R.L.P., *Temperature Step Effects on Direct Measurement of Skin-Friction Drag*, AIAA 78-779, 1978.

[56] MacArthur, R., *Transducer for Direct Measurement of Skin Friction in the Hypersonic Shock Tunnel*, CAL Report 129, 1963

[57] Winter, K. G. and Gaudet, L., *Turbulent Boundary Layer Studies at High Reynolds Numbers at Mach Numbers Between 0.2 and 2.8*, ARC R&M 3712, 1970.

[58] Schetz, J.A. and Nerney, B., *The Turbulent Boundary Layer with Injection and Surface Roughness*, AIAA J., Vol. 15, No. 9, pp. 1288-1294, 1977.

[59] MultiTherm, *Food Grade Mineral Oil MultiTherm PG-1*. Retrieved September 09, 2009, from the World Wide Web: http://www.multitherm.com/multitherm-pg-1.html

[60] The Lee Company, *Lee Plug Inspection and Handling Instructions*. Retrieved June 20, 2009, from the World Wide Web: http://www.theleeco.com/

[61] Department of Aerospace and Ocean Engineering: Hypersonic Wind tunnel. Retrieved July 21, 2009 from the World Wide Web: http://www.aoe.vt.edu/research/facilities/hyperson.php

[62] Russian Academy of Sciences Siberian Fivision Institute of Theoretical and Applied Mechanics. *The Model Aerodynamic Facility (MAF) for Student's Research and Instructions*. Novosibirsk, Russia, 2002.

[63] Omega Engineering, Inc., *Transition Junction Style Probes with High Temperature Molded Construction*. Stamford, CT, 2009

[64] Velmex, Inc. *BiSlide Traverse Assemblies*. Bloomfield, NY, 2001.

[65] Oriental Motor U.S.A. Corp. *Item # PK268-03B, 2-Phase Stepping Motor*. Torrance, CA, 2010.

[66] Velmex, Inc. *Motors and Controls*. Bloomfield, NY, 2010.

[67] Vishay Intertechnology, Inc., Measurement Group. *Instruction Manual Model 2310 Signal Conditioning Amplifier*. Shelton, CT, 1985.

[68] National Instruments, *Full-Featured E Series Multifunction DAQ 12 or 16-Bit , up to 1.25 MS/s, up to 64 Analog Inputs*. Retrieved June 20, 2009 from World Wide Web: http://www.ni.com/pdf/products/us/4daqsc199-201_ETCx2_212-213.pdf

[69] National Instruments. *LabVIEW*. Computer software. Version 2009.

[70] Goyne, C. P., Stalker, R. J., Paull, A., *Skin-friction measurements in high-enthalpy hypersonic boundary layers*, Cambridge University Press, United Kingdom, 2003.

[71] Schlicting, Herrmann and Klaus Gersten, *Boundary-Layer Theory 8th Edition*. Springer, New York 2000, p. 620.

[72] Devenport, W. J., Schetz, J. A. *CTBL*. Computer software. *Java Applets for Engineering Education*. Department of Aerospace and Ocean Engineering, Virginia Tech. Accessed January 27, 2010 from World Wide Web: http://www.engapplets.vt.edu/

[73] Schneider, Paul J. *Conduction Heat Transfer*. Reading, Mass.: Addison-Wesley Pub., 1974.

[74] Epoxy Technology, Inc. *EPO-TEK 353ND Technical Data Sheet*. Billerica, MA, 2009. Retrieved June 20, 2009 from World Wide Web: www.epotek.com/SSCDocs/datasheets/353ND.pdf

[75] Figliola, R.S. and Beasley, D.E., *Theory and Desgin for Mechanical Measurements.* 2nd Edition, John Wiley & Sons, Inc., New York, 1995, pp. 171-210.

[73] Dassault Systèmes SolidWorks Corp. *SolidWorks*. Computer software. Version 2009 SP2.

Appendix A: Drawings

Drawing 1: DSC-6 Unit

NOTE: DIMENSIONS ARE IN INCHES

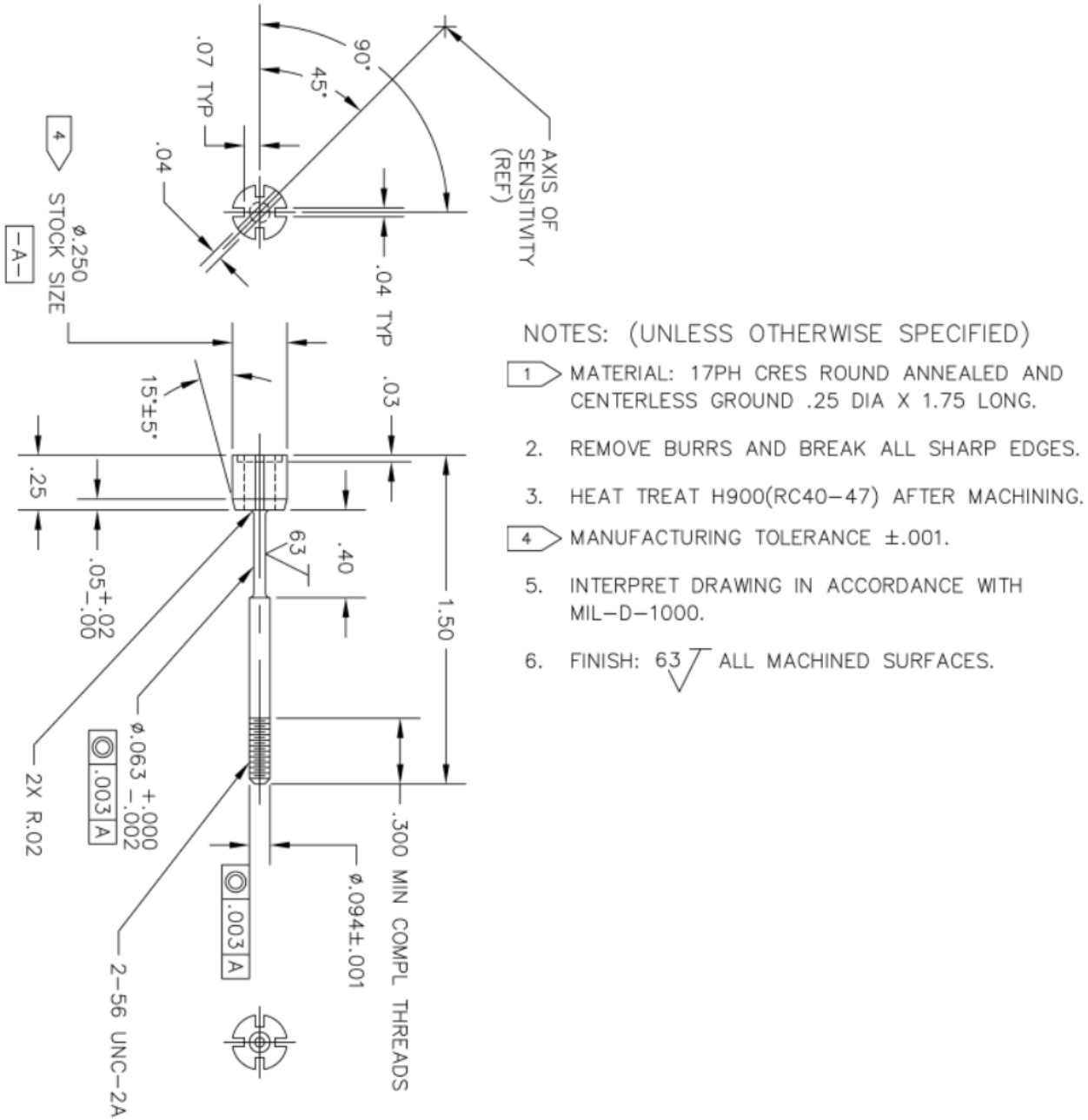

Drawing 2: DSC-6 Unit Assembly

NOTE: DIMENSIONS ARE IN INCHES

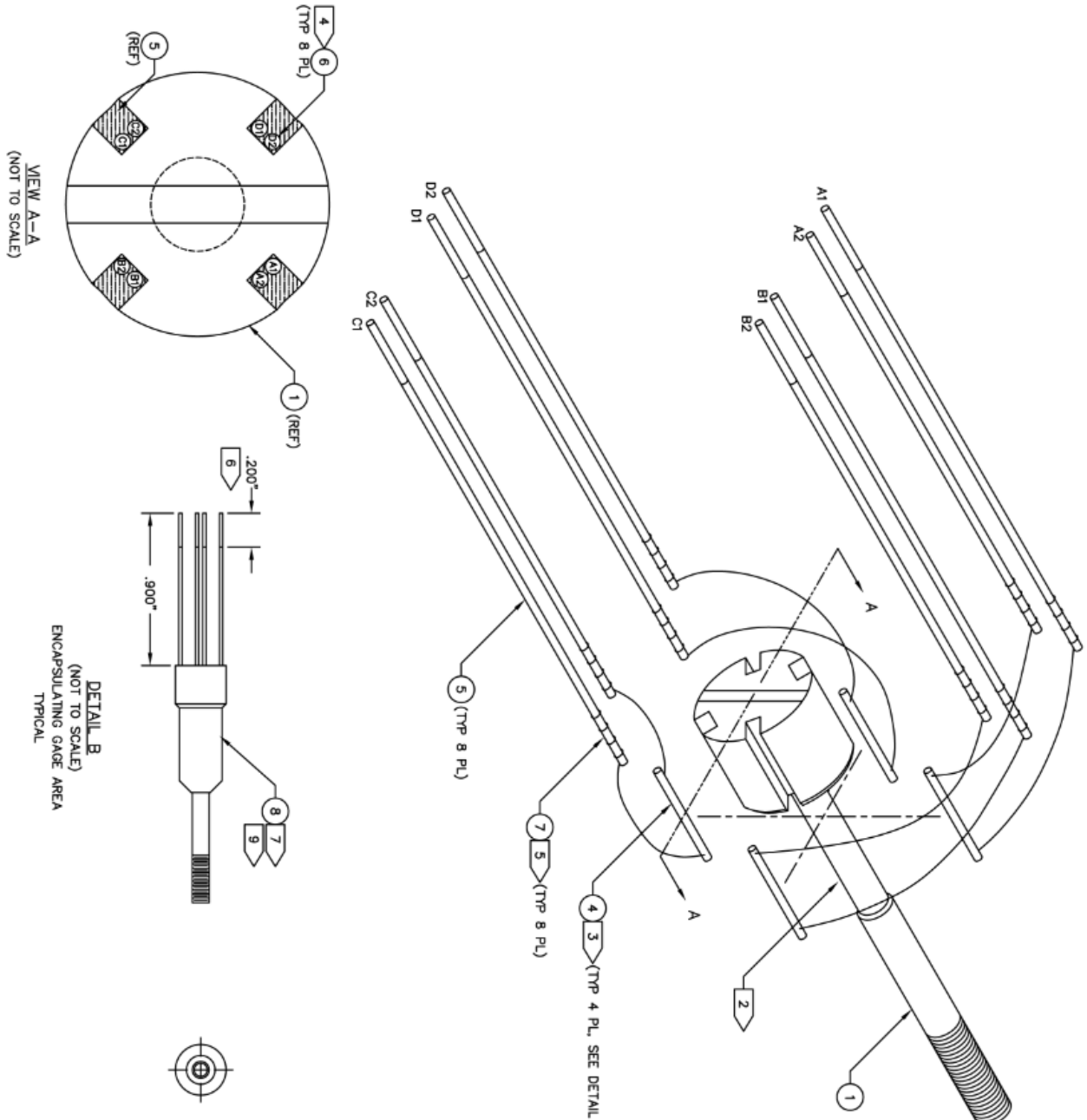

Drawing 3: *PT*-1 Base Housing

NOTE: DIMENSIONS ARE IN INCHES

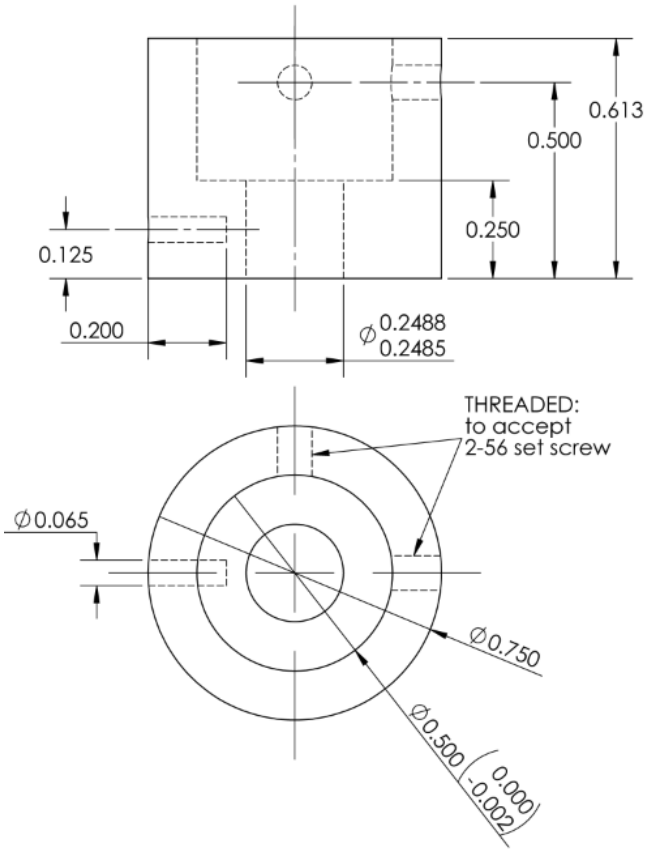

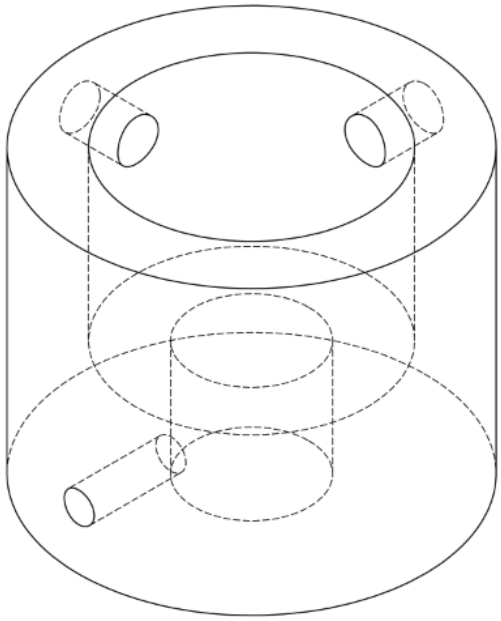

Drawing 4: *PT*-1 Top Housing

NOTE: DIMENSIONS ARE IN INCHES

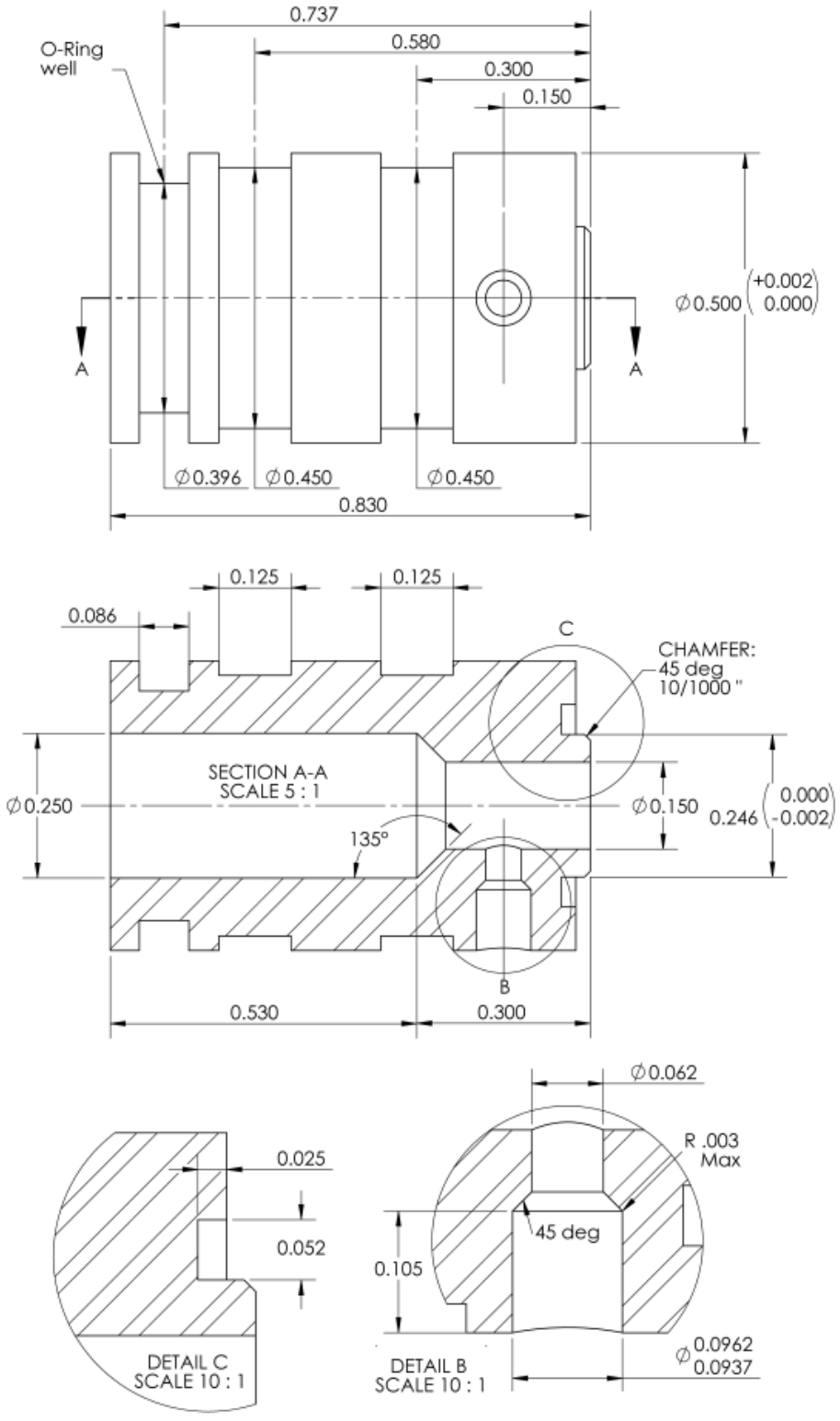

Drawing 5: *PT*-2 Single Piece Housing

NOTE: DIMENSIONS ARE IN INCHES

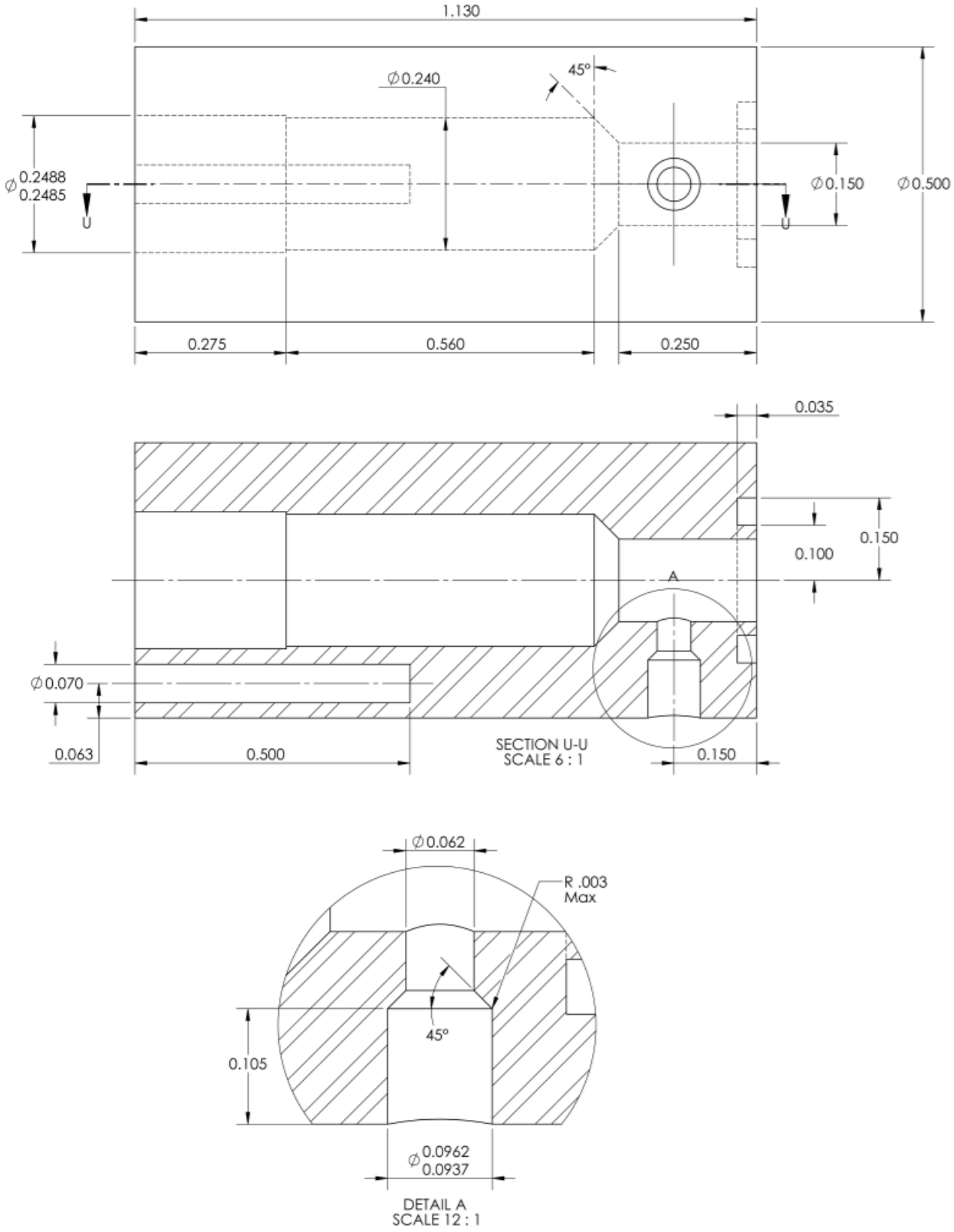

Drawing 6: *PT*-1 and *PT*-2 Head

NOTE: DIMENSIONS ARE IN INCHES

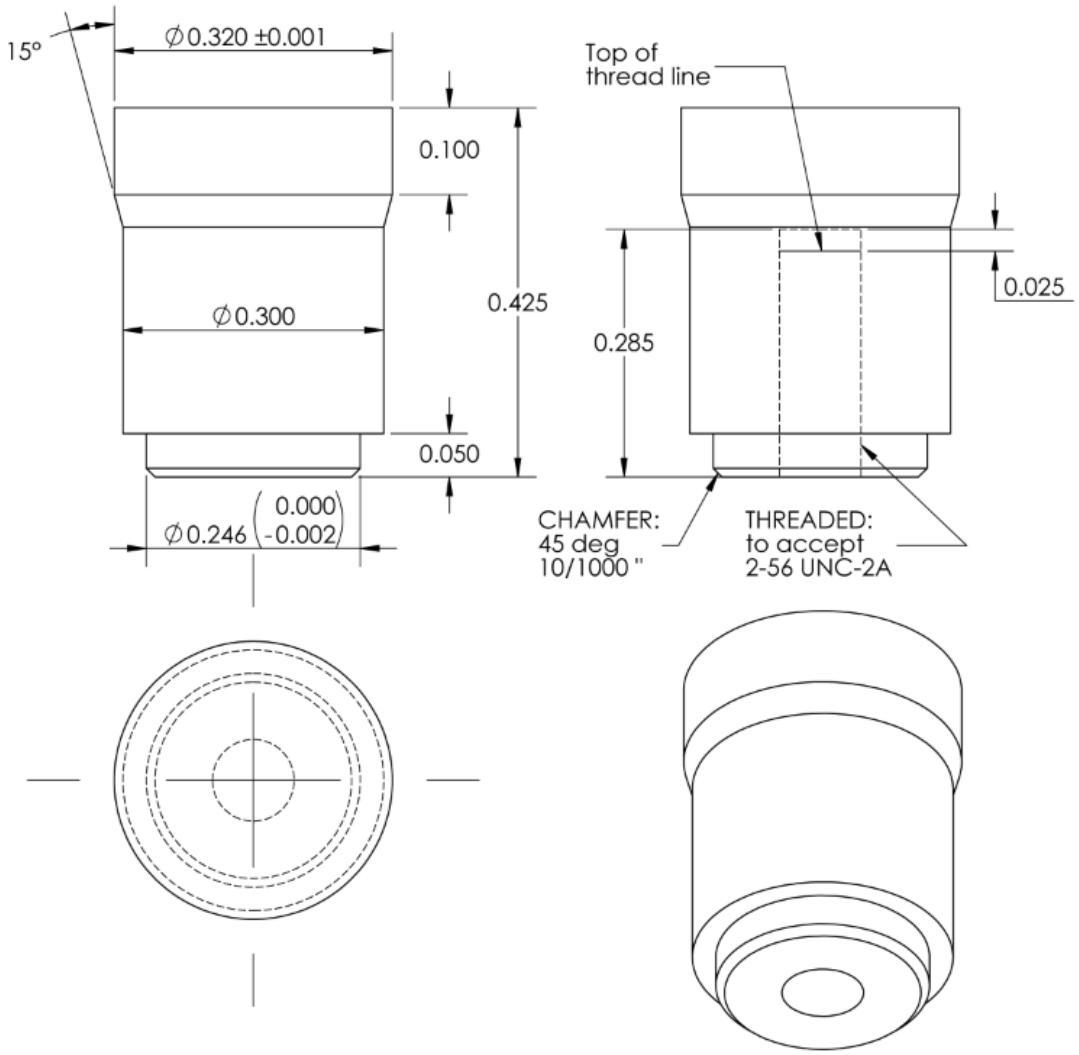

Drawing 7: *PT*-1 and *PT*-2 Collar

NOTE: DIMENSIONS ARE IN INCHES

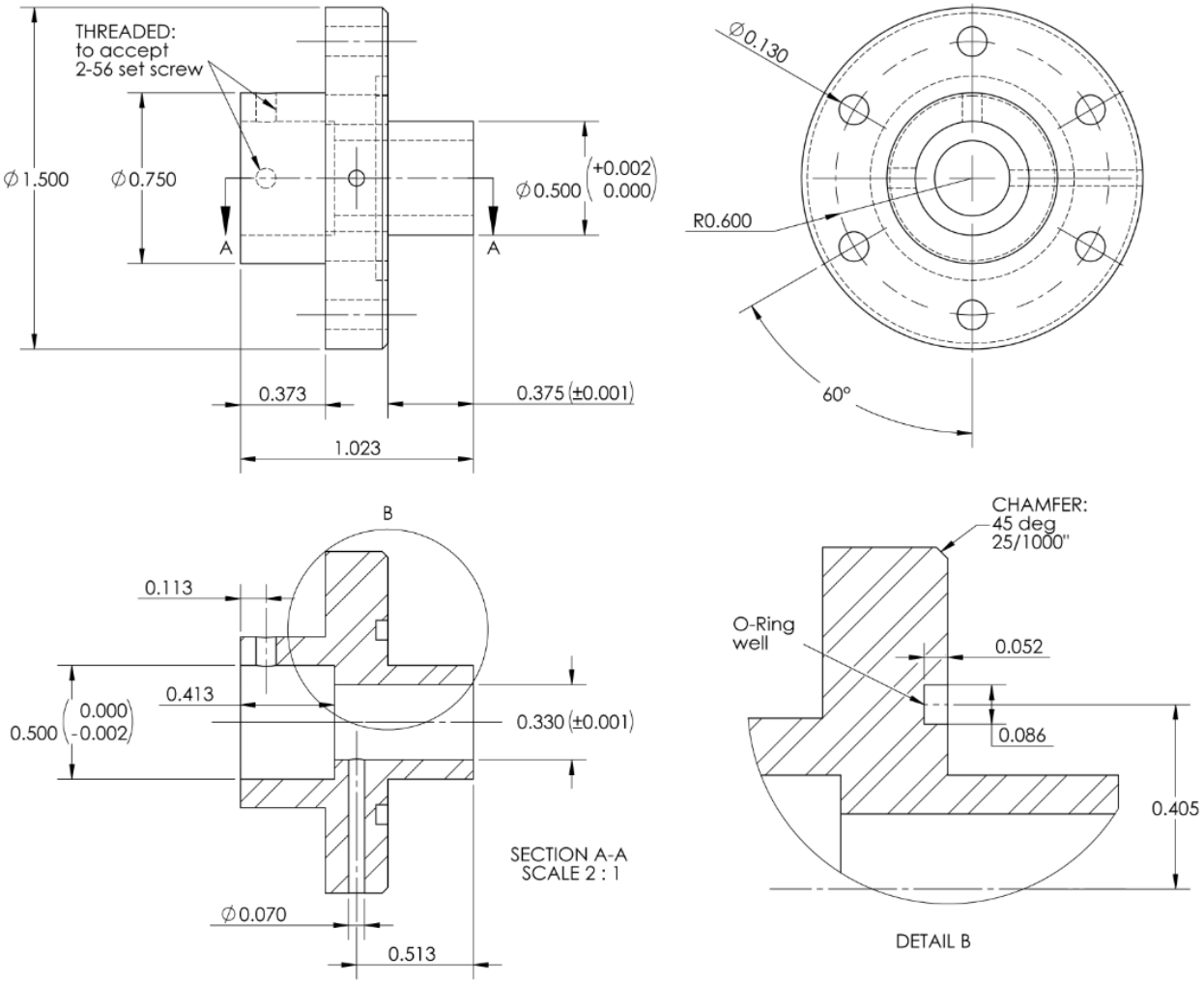

Drawing 8: *PT*-1 and *PT*-2 Flat Plate

NOTE: DIMENSIONS ARE IN INCHES

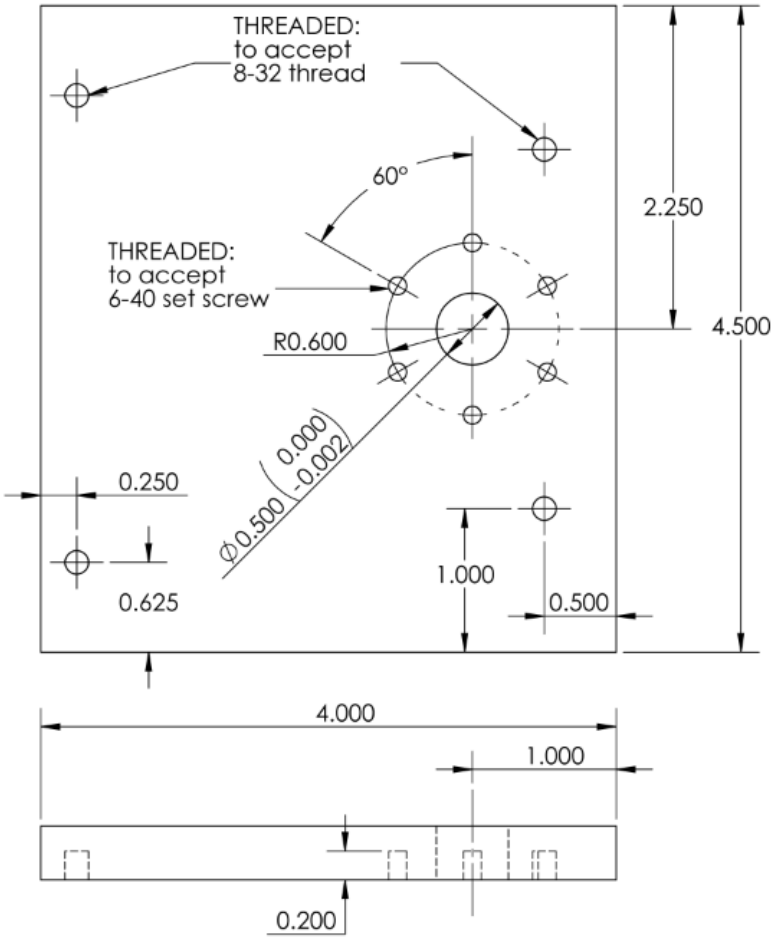

Drawing 9: *PT*-1 Assembly

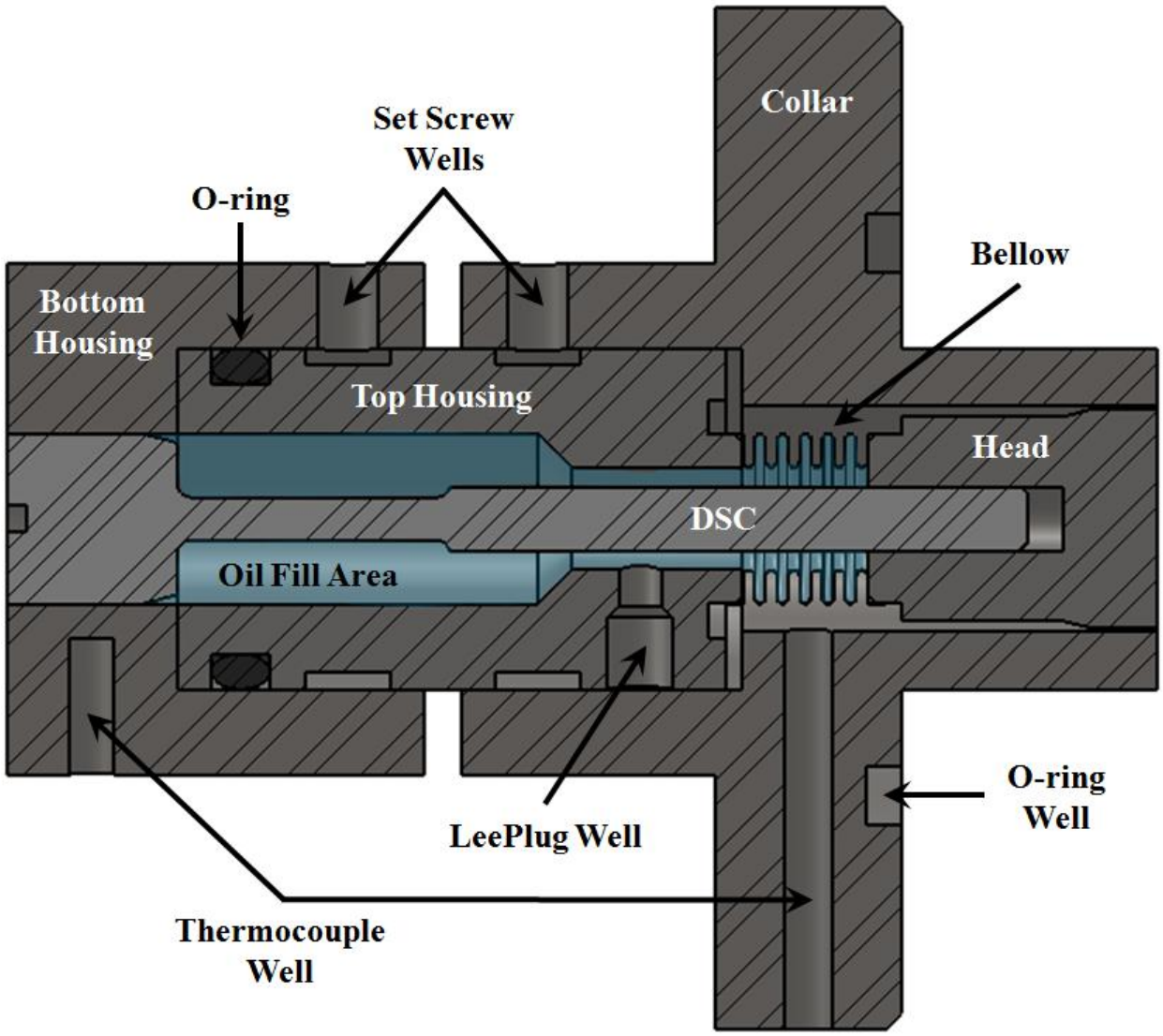

Drawing 10: *PT*-2 Assembly

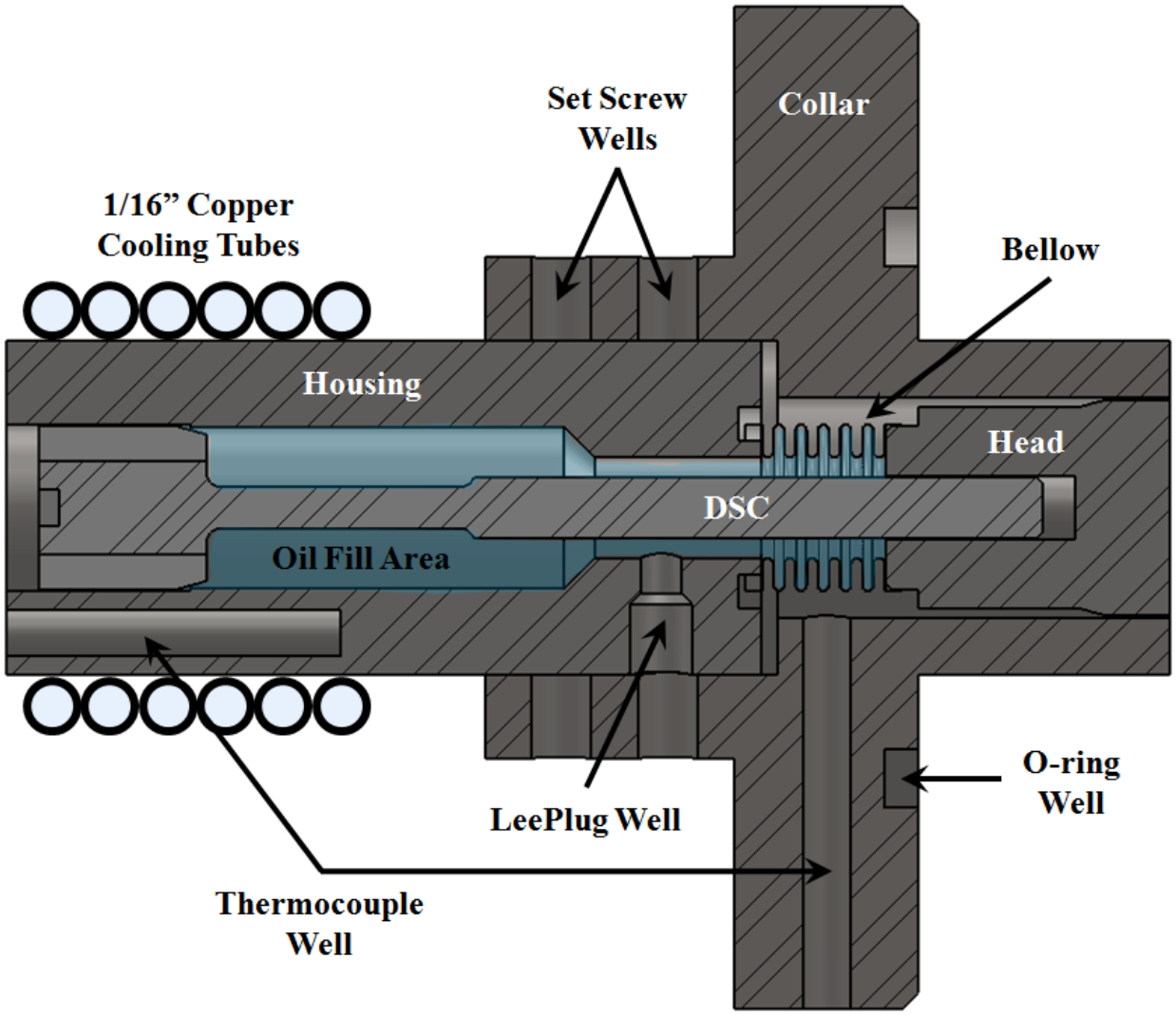

Appendix B: Equation Sets

Theoretical / Experimental Calculations:

$$\tau_w = \frac{m \cdot g}{A_{head}} \cdot \frac{1}{\cos(\theta)} = \frac{(b \cdot T_{DSC} + c) \cdot V}{\cos(\theta)} \quad \textbf{Equation B.1}$$

$$M_e = 0.6926 \cdot \left(\frac{P_{cone}}{P_{pitot}}\right)^{-0.6905} \quad \textbf{Equation B.2}$$

$$T_e = \frac{T_0}{\left(1 + \frac{\gamma - 1}{2} M_e^2\right)} \quad \textbf{Equation B.3}$$

$$U_e = a \cdot M_e = \sqrt{\gamma \cdot R \cdot T_e} \cdot M_e \quad \textbf{Equation B.4}$$

$$\rho_0 = \frac{P_0}{R \cdot T_0} \quad \textbf{Equation B.5}$$

$$\rho_e = \frac{\rho_0}{\left(1 + \frac{\gamma - 1}{2} M_e^2\right)^{\frac{1}{\gamma - 1}}} \quad \textbf{Equation B.6}$$

$$Re_\delta = \frac{\rho_e \cdot U_e \cdot \delta}{\mu} \quad \textbf{Equation B.7}$$

$$C_{f-inc} = 0.0456 \cdot (Re_\delta)^{-1/4} \quad \textbf{Equation B.8}$$

$$C_{f-comp} = \frac{\tau_w}{1/2 \cdot \rho_e \cdot U_e^2} \quad \textbf{Equation B.9}$$

$$h = \frac{\rho_e \cdot U_e \cdot c_p \cdot C_{f-comp}}{2} \quad \textbf{Equation B.10}$$

$$T_{aw} = T_e + r \cdot (T_0 - T_e) \quad \textbf{Equation B.11}$$

$$\dot{q}_w = h \cdot (T_w - T_{aw}) \quad \textbf{Equation B.12}$$

Uncertainty Calculations:

$$\delta(\tau_w) = \sqrt{\left[\frac{\partial \tau_w}{\partial V}\cdot \delta(V)\right]^2 + \left[\frac{\partial \tau_w}{\partial T_{DSC}}\cdot \delta(T_{DSC})\right]^2 + \left[\frac{\partial \tau_w}{\partial \theta}\cdot \delta(\theta)\right]^2 + \left[\frac{\partial \tau_w}{\partial b}\cdot \delta(b)\right]^2 + \left[\frac{\partial \tau_w}{\partial c}\cdot \delta(c)\right]^2}$$ **Equation B.13**

$$\delta(T_e) = \sqrt{\left[\frac{\partial T_e}{\partial T_0}\cdot \delta(T_0)\right]^2 + \left[\frac{\partial T_e}{\partial M_e}\cdot \delta(M_e)\right]^2}$$ **Equation B.14**

$$\delta(U_e) = \sqrt{\left[\frac{\partial U_e}{\partial T_e}\cdot \delta(T_e)\right]^2 + \left[\frac{\partial U_e}{\partial M_e}\cdot \delta(M_e)\right]^2}$$ **Equation B.15**

$$\delta(\rho_0) = \sqrt{\left[\frac{\partial \rho_0}{\partial P_0}\cdot \delta(P_0)\right]^2 + \left[\frac{\partial \rho_0}{\partial T_0}\cdot \delta(T_0)\right]^2}$$ **Equation B.16**

$$\delta(\rho_e) = \sqrt{\left[\frac{\partial T_e}{\partial \rho_0}\cdot \delta(\rho_0)\right]^2 + \left[\frac{\partial T_e}{\partial M_e}\cdot \delta(M_e)\right]^2}$$ **Equation B.17**

$$\delta(C_f) = \sqrt{\left[\frac{\partial C_f}{\partial \tau_w}\cdot \delta(\tau_w)\right]^2 + \left[\frac{\partial C_f}{\partial \rho_e}\cdot \delta(\rho_e)\right]^2 + \left[\frac{\partial C_f}{\partial U_e}\cdot \delta(U_e)\right]^2}$$ **Equation B.18**

$$\delta(h) = \sqrt{\left[\frac{\partial h}{\partial \rho_e}\cdot \delta(\rho_e)\right]^2 + \left[\frac{\partial h}{\partial C_f}\cdot \delta(C_f)\right]^2 + \left[\frac{\partial h}{\partial U_e}\cdot \delta(U_e)\right]^2}$$ **Equation B.19**

$$\delta(T_{aw}) = \sqrt{\left[\frac{\partial T_{aw}}{\partial T_e}\cdot \delta(T_e)\right]^2 + \left[\frac{\partial T_{aw}}{\partial T_0}\cdot \delta(T_0)\right]^2}$$ **Equation B.20**

$$\delta(\dot{q}_w) = \sqrt{\left[\frac{\partial \dot{q}_w}{\partial h}\delta(h)\right]^2 + \left[\frac{\partial \dot{q}_w}{\partial T_w}\delta(T_w)\right]^2 + \left[\frac{\partial \dot{q}_w}{\partial T_{aw}}\delta(T_{aw})\right]^2}$$ **Equation B.21**

Appendix C: Facilities Employed

1. **AOE Shop**
   15A Randolph Hall
   Virginia Tech
   Blacksburg, VA 24061
   Tel: (540) 231-6752
   Contact: James Lambert

2. **Damon Company of Salem, Inc.**
   2117 Salem Ind. Dr.
   Salem, VA 24153
   Tel: (540) 389-8609
   Contact: Oliver White

3. **Venture Measurement**
   Kistler-Morse
   150 Venture Blvd.
   Spartanburg, SC 29306
   Tel: (864) 669-5241
   Contact: James Thornton

4. **PMG LLC/Servometer**
   501 Little Falls Rd.
   Cedar Grove, NJ 07009
   Tel: (973) 785-4630
   Contact: Steven Oliphant

5. **Arnold Engineering**
   Development Center
   1099 Schriever Ave.
   Arnold AFB, TN 37389
   Tel: (931) 454-7627
   Contact: Joseph Sheeley

6. **Luna Innovations**
   3157 State St.
   Blacksburg, VA 24060
   Tel: (540) 552-5128
   Contact: Alex Sang

7. **The Lee Company**
   2 Pettipaug Rd.
   Westbrook, CT 06498
   Tel: (800) 399-6281
   Contact: Peter Costa